

CEBAF UPGRADE BUNCH LENGTH MEASUREMENTS

by

Mahmoud Mohamad Ali Ahmad
B.S. 1999, Tanta University - Egypt
M.S. 2004, Tanta University - Egypt
M.S. 2011, Old Dominion University

A Dissertation Submitted to the Faculty of
Old Dominion University in Partial Fulfillment of the
Requirements for the Degree of

DOCTOR OF PHILOSOPHY

PHYSICS

OLD DOMINION UNIVERSITY

May 2016

Approved by:

Geoffrey Krafft (Director)

Arne Freyberger (Member)

Charles Sukenik (Member)

Gail Dodge (Member)

Helmult Baumgart (Member)

ABSTRACT

CEBAF UPGRADE BUNCH LENGTH MEASUREMENTS

Mahmoud Mohamad Ali Ahmad
Old Dominion University, 2016
Director: Dr. Geoffrey Krafft

Many accelerators use short electron bunches and measuring the bunch length is important for efficient operations. CEBAF needs a suitable bunch length because bunches that are too long will result in beam interruption to the halls due to excessive energy spread and beam loss. In this work, bunch length is measured by invasive and non-invasive techniques at different beam energies. Two new measurement techniques have been commissioned; a harmonic cavity showed good results compared to expectations from simulation, and a real time interferometer is commissioned and first checkouts were performed. Three other techniques were used for measurements and comparison purposes without modifying the old procedures. Two of them can be used when the beam is not compressed longitudinally while the other one, the synchrotron light monitor, can be used with compressed or uncompressed beam.

Copyright, 2016, by Mahmoud Mohamad Ali Ahmad, All Rights Reserved.

Dedicated to my family, my late father, and my late mother.

ACKNOWLEDGMENTS

First and foremost, I would like to thank my thesis advisor Dr. Geoffrey Krafft for giving me the opportunity to work in the accelerator field, teaching me the fundamental basics to understand the field, and supporting me during the research period.

I am very grateful to Dr. Arne Freyberger, the Director of Operations at Jefferson Lab, for providing me the funding for the chamber fabrication, the Real Time Interferometer loan, allowing me sufficient beam time to do the research, and mentoring me. Dr. Freyberger was very patient during my research, led me to understand programming, and helped me to build my scientific skills through discussions and guidance.

I would like to offer my thanks to Dr. Charles Sukenik, Dr. Gail Dodge, and Dr. Helmut Baumgart for their acceptance of the proposal, guiding me by discussion during the annual reviews, and their review of the final thesis.

I would especially like to thank Dr. Matthew Poelker for giving me the opportunity to work with him and the injector group. I am indebted to Dr. Michael Tiefenback for his long discussions, guidance, and explanations in beam physics. I would like to thank Joe Gubeli for his chamber design, Steve Benson for teaching me the SRW code, Fay Hanon for providing me the simulation data, Alicia Hofler for providing me the expected bunch length in the 1D line, and CEBAF operators who helped me during the experiments. Also I would like to express my thanks to CASA members, especially Michael Spata for showing me how to perform the zero-phasing technique, Todd Satogata for discussion about kinematic compression, and Yves Roblin for helping me to understand Elegant simulations.

I would like to offer my thanks to my colleagues Maha Omar, Diego Franco, and my ODU professors for helping me throughout my first year in the graduate school. Also, I would like to express my thanks to the Muslim community for their support especially Hisham Sayed, Ahmed Al Sum, Ahmed Elmekawy, and Dr. Abdelmagged Elmustafa for his discussions and guidance about life issues and research obstacles.

Finally, I express special debt of gratitude to my wife Haidi Elmekawy for her patience and support through out my studying in USA. I thank my son Ali and my daughter Judi for their joy and amusement during the previous years. I am grateful to my brother Sherif and my sister Hager for their support and chatting which makes me feel that I am still with them.

TABLE OF CONTENTS

	Page
LIST OF TABLES	viii
LIST OF FIGURES	ix
Chapter	
1. CEBAF OVERVIEW	1
1.1 INTRODUCTION	1
1.2 BEAM LINE DESCRIPTION	1
2. LITERATURE REVIEW OF BUNCH LENGTH MEASUREMENTS	8
2.1 INTRODUCTION	8
2.2 BUNCH LENGTH MEASUREMENTS REVIEW	8
3. THEORETICAL BACKGROUND	16
3.1 CHARGED PARTICLE IN A MAGNETIC FIELD	16
3.2 TRANSFER MATRICES	16
3.3 BETA FUNCTION AND BEAM ENVELOPE	19
3.4 PHASE SPACE	20
3.5 BUNCH COMPRESSION	21
3.6 SYNCHROTRON RADIATION	26
3.7 COHERENT RADIATION AND FORM FACTOR	28
3.8 FORM FACTOR FOR DIFFERENT DISTRIBUTIONS	30
4. FAR-INFRARED MEASUREMENTS	33
4.1 MIRRORS	33
4.2 WINDOWS	33
4.3 DETECTORS	35
4.4 CONCLUSION	37
5. BUNCH LENGTH MEASUREMENT TECHNIQUES	38
5.1 DESTRUCTIVE TECHNIQUES	38
5.2 NON-DESTRUCTIVE TECHNIQUES	40
6. CEBAF BUNCH LENGTH MEASUREMENTS	44
6.1 BUNCH LENGTH IN THE INJECTOR	44
6.2 BUNCH LENGTH IN THE 4D LINE	63
6.3 BUNCH LENGTH IN THE INJECTOR CHICANE	66
6.4 SYNCHROTRON LIGHT MONITOR	78

7. SUMMARY AND CONCLUSION	88
APPENDICES	
A. SIGNAL PROCESSING	97
A.1 WIENER-KHINCHIN THEOREM	97
A.2 CONVOLUTION THEOREM	98
B. BEAM DYNAMICS	99
B.1 TILTED ELLIPSE	99
B.2 M_{56} FOR KINEMATIC COMPRESSION	101
C. COMPUTER CODES USED	103
C.1 MATLAB CODE	103
C.2 ELEGANT	105
C.3 ELEGANT: INJ.ELE	114
 VITA	 116

LIST OF TABLES

Table	Page
1 Bunch length results for different currents using the chopper slit technique	51
2 Bunch length results for different currents using the Brock cavity in the 1D line . .	54
3 Bunch length results for Brock cavity at A2 and slit scan technique using the 249.5 MHz laser	56
4 Bunch length results for Brock cavity at A2 and slit scan technique using the 499 MHz laser	56
5 Back-phasing results	64
6 Estimated power for different beam current	67
7 Edge radiation parameters	68
8 Estimated power for the detector's channels at 50 μA	77
9 Bunch length results	86
10 Bunch length results (<i>rms</i> value) summary at all locations	90

LIST OF FIGURES

Figure	Page
1 12 GeV CEBAF schematic overview.	2
2 Spreader at the end of South Linac.	3
3 Recombiner at the beginning of South Linac.	4
4 499 MHz separation for three beams [1].	5
5 749.5 MHz separation with all the buckets are filled [1].	6
6 749.5 MHz separation with some empty buckets [1].	6
7 Particle trajectories for different particles [31]. (a) is for a single particle trajectory while (b) is for 18 different trajectories.	20
8 Bunch compression using kinematic compression at 130 keV for different chirp . . .	23
9 Bunch compression through a magnetic chicane	24
10 Phase space before and after compression	25
11 Power spectrum for 123 MeV electron beam at 300 μ A with 499 MHz repetition rate and Gaussian bunches with <i>rms</i> length σ	27
12 A diagram to calculate the electric field of a bunch	29
13 Transmission curve for different materials	34
14 Schematic diagram for pyrodetector and its equivalent electrical circuit where V_{in} is applied voltage, R_D is the detector resistance, C_D is the detector capacitance, R_L is the load resistance, C_L is the load capacitance, and V_{out} is the output voltage.	36
15 Transverse deflecting cavity.	39
16 Streak camera.	40
17 Michelson interferometer	41
18 Wall current monitor	43
19 Equivalent circuit for wall current monitor	43
20 Gain switch representation	45

21	SHG representation	45
22	Definition of time structure [32]. a) Microbunch with time duration τ_μ . b) Microbunches separated by a multiple of the RF period. T_μ is either 3 or 6 times 666.8 psec, the fundamental accelerating period.	46
23	Current for different beam modes. The series of spikes represents the micropulsed current, not to scale	47
24	chopping chamber	48
25	Schematic diagram for injector line from the gun to the 1D line.	49
26	The beam current transmitted through the chopper-slit as a function of the laser phase is shown for six different beam currents. These measurements were made using the A-laser with a 499 MHz repetition rate.	50
27	Brock cavity	52
28	Brock cavity in 1D line	53
29	Oscilloscope signal from camera and epics	53
30	Measured voltage before and after using transfer function correction for the Brock cavity at the 1D line.	55
31	Measured voltage for A-laser and B-laser for Brock cavity at the A2 location.	57
32	Slit scan for A-laser and B-laser.	58
33	Simulated and measured electron bunch length as a function of bunch charge at 249.5 MHz for chopper-slit technique and Brock cavity technique. The uncertainty on the chopper-slit technique data is at most 0.4 ps while on the Brock technique data is at most 0.1 ps and therefore is not visible on the plot.	60
34	Simulated and measured electron bunch length as a function of bunch charge at 499 MHz for chopper-slit technique and Brock cavity technique. The uncertainty on the chopper-slit technique data is at most 0.3 ps while on the Brock technique data is at most 0.1 ps and therefore is not visible on the plot.	61
35	Brock cavity as phase detector	62
36	Voltmeter output as a function of phase	62
37	Schematic drawing for 4D line	63
38	Back-phasing results	65

39	Schematic diagram for the SR coming from the injector chicane fourth dipole. The solid blue lines represents the ends of the dipole. The mirror is 455.5 mm from the center of the arc from where SR hits the mirror.	66
40	Estimated power spectrum for different beam current	67
41	Radiation intensity for different frequencies around the mirror location. The color key on the right of the figure represents the intensity where the dark red is the minimum value and equals 3.1×10^5 photons/mm ² . The dark blue represents the maximum intensity and equals 8.99×10^7 photons/mm ²	69
42	Old and new beam line	69
43	Chamber assemblies	70
44	Optical line	71
45	Radiabeam Real Time Interferometer	72
46	Camera is installed to check the light coming from the optical port	74
47	Camera output when SL mirror is inserted and retracted	74
48	Oscilloscope traces at different currents	76
49	Oscilloscope traces at different chopping frequencies	76
50	Detector installed in a new position	77
51	Synchrotron light monitor	79
52	The spot length on SLM changes as the NL gang phase changes.	83
53	Changing the gradient by ± 1 MV to calculate the dispersion.	83
54	Hyperbola fitting for Arc1 - head to tail calculation (tune mode).	84
55	Hyperbola fitting for Arc1 - <i>rms</i> calculation (tune mode).	84
56	Hyperbola fitting for Arc2 - head to tail calculation (tune mode).	85
57	Hyperbola fitting for Arc2 - <i>rms</i> calculation (tune mode).	85
58	Hyperbola fitting for Arc1 - <i>rms</i> calculation (CW mode).	87
59	Hyperbola fitting for Arc2 - <i>rms</i> calculation (CW mode).	87
60	Phase space	100

CHAPTER 1

CEBAF OVERVIEW

1.1 INTRODUCTION

The Continuous Electron Beam Accelerator Facility (CEBAF) at Jefferson Lab in Newport News, Virginia, is designed to provide high energy electron beams for nuclear physics research. It accelerates an electron beam to 12 GeV after 5.5 circulation passes. CEBAF consists of two linacs, recirculating arcs, and four experimental halls. The facility has a circumference of 1.4 km and it is about 8 m under ground. The dimensions of the accelerator tunnel are about 3 m high by 4 m wide. The first electron beam was delivered to users in Hall C with beam energy equal to 4 GeV and beam current equal to 200 μA in 1995. Two years later, beam was delivered into Hall A and Hall B. By 1998, the three halls were operated simultaneously. In 2000, the SRF gradient and cryogenic systems were sufficient to support energy of 6 GeV. Six GeV operation was terminated in 2012 for an upgrade to 12 GeV. Commissioning of 12 GeV CEBAF started at the end of 2013 and should be completed by 2017.

1.2 BEAM LINE DESCRIPTION

The Jefferson Lab 12 GeV beam line is shown in Fig. 1. The beam is created in the injector by using up to four lasers. The lasers are operating at either the third or sixth subharmonic of the 1497 MHz RF operating frequency in order to create interleaved beams with different currents. Each such beam is delivered to a different hall. The laser beams fall on a GaAs photocathode which is held at 130 kV where the electrons are liberated. The electron beam is transported through the injector section of CEBAF, which includes the following RF structures: a prebuncher, a buncher, a capture section, a 1/4 cryomodule, which consists of two Superconducting RF (SRF) accelerating cavities, and two full cryomodules. After the 1/4 cryomodule the beam energy is 6.3 MeV. The beam achieves full injection energy of 123 MeV after acceleration by the cryomodules before the injector chicane. Each full cryomodule consists of eight 1497 MHz SRF cavities. Each five cell SRF cavity is 50 cm long in C20 and C50 cryo-modules; new C100 cryo-modules have 7-cell cavities and each cavity is 70 cm

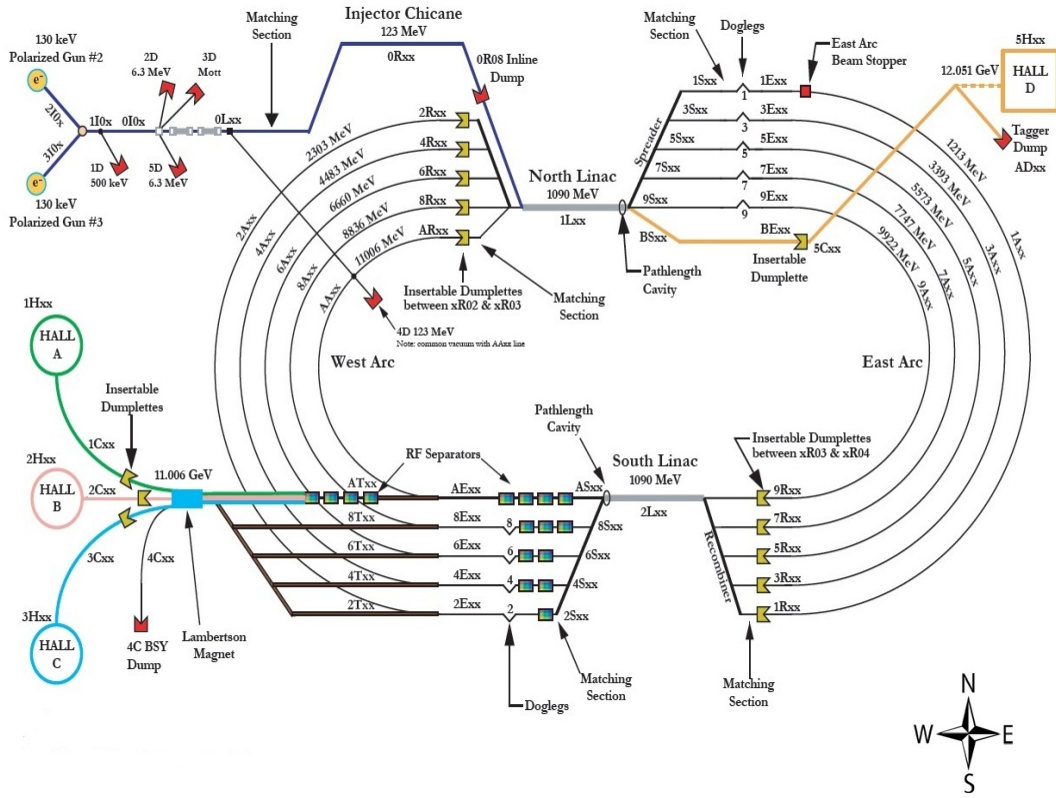


FIG. 1: 12 GeV CEBAF schematic overview.

long. The cryomodules are filled with liquid helium and operate at 2.07 K. After the injector chicane the beam is injected into the North linac.

The North linac is 250 meters long and consists of 25 accelerating cryomodules. Between the cryomodules an alternating gradient magnetic lattice is used to ensure that the beam is focused with the design parameters. In traversing the linac, the beam energy is increased by 1090 MeV after which it meets the spreader. In the spreader, the different beam energies are separated vertically by using dipole magnets. The lowest energy is directed towards the highest elevated arc (Arc 1) and the highest energy is directed towards the lowest elevated arc (Arc 9). The beam is bent through 180° as it propagates through the East arcs (Arc1, Arc3, Arc5, Arc7, and Arc9). At the end of the arcs, the beam will go through a recombiner which is mirror symmetric with respect to the spreader. In the recombiner, the separated



FIG. 2: Spreader at the end of South Linac.

beams are reformed into one beam as they go into the South linac. By design each arc is different in path length by an integer number of RF wavelengths to maintain synchronism across different beam passes and within one pass all the electrons travel the same path length regardless of their energy, which means the arcs are isochronous. The ARC focusing lattice is designed to be achromatic, meaning that the position and angle of beam transport are independent of the energy.

The South linac is approximately equal to the North linac in acceleration capacity and the beam energy is increased by another 1090 MeV. At the end of the South linac, the beam traverses the West spreader which acts similarly to the East spreader. As the beam leaves the spreader, it can be extracted into one of the three experimental halls or it can go to the West arcs (Arc2, Arc4, Arc6, Arc8, and ArcA) and be bent by 180° before it goes through the West recombiner. After the West recombiner, the beam will meet the North linac again, so each complete revolution will increase the beam energy by 2180 MeV. In each of Arcs1-9 path length adjustment is accomplished using doglegs to ensure successive passes are synchronized. Doglegs are three magnet chicane systems and are used to match the arrival time of the following passes to the crest of RF wave. The locations of the doglegs are at the beginning of each arc (five at the beginning of each East arc and four at the beginning of each West arc, except the highest energy arc). The doglegs can change the path length up to 2 cm but in the 12 GeV era, the path length can be changed only by 1 cm corresponding



FIG. 3: Recombiner at the beginning of South Linac.

to 18^0 of 1497 MHz for the first four doglegs limited by the power supplies. The path length change is less than 1 cm for the remaining doglegs.

If the beam is extracted to one of the halls before five beam passes, it must go through the energized extraction system which consists of a 499 MHz RF separator cavity and two septum magnets. As any beams leave the West spreader, they will meet the RF separators where the desired extracted beam will be deflected to the left and any recirculating beam will be deflected to the right. Then the beams will pass through the first septum magnet which has a magnetic field on the left and zero magnetic field on the right of the septum. Any non-extracted beams will continue recirculating while the extracted beam encounters a second septum magnet and is directed into the beam switch-yard recombining section.

This type of extraction to Halls A, B, or C beam can be done from the first to the fourth pass. The separator phase is set in such a way as to give different kicks to the beam. For instance, if beam A is extracted, the cavity will give a kick for beam A to the left while B and C beams are kicked to the right to continue recirculating as shown in Fig. 4. The extraction of the beams can happen simultaneously at the end of the fifth pass using a 749.5 MHz RF separator (4 cavities). Since the 749.5 MHz is one half the fundamental frequency (1497 MHz), when the separators are set properly and the bunches will receive alternating right and left kicks as shown in Fig. 5. The beam pattern can be represented as $A_R B_L C_R A_L B_R C_L$ where the suffix R and L represents the right or left kick. Half of the bunches

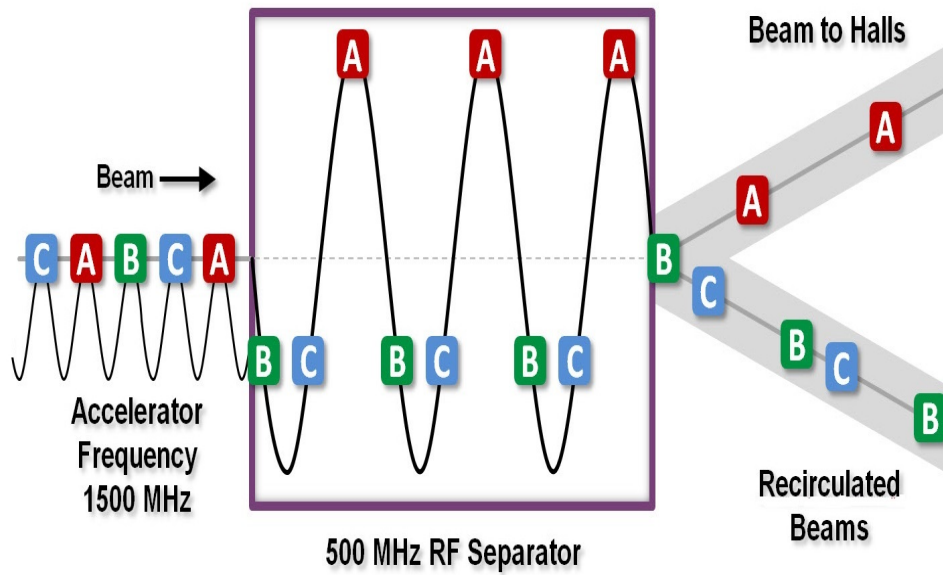


FIG. 4: 499 MHz separation for three beams [1].

($A_L B_L C_L$) will go to the 499 MHz separator and continue to go to one of the three halls while the second half ($A_L B_L C_L$) will go to Hall D. If the injector produces three 249.5 MHz bunches ($A_L B_L C_L$) and a fourth 249.5 MHz bunch (A_R or B_R or C_R), then all the four halls will receive beam simultaneously. In such cases, the 749.5 separator will work as shown in Fig. 6, where the empty bucket represents no beam.

The Hall D beam continues recirculating while Hall A beam, Hall B beam, and Hall C beam meet the AT_{xx} RF separator. The final RF separators are turned on and phased so that the Hall A beam is kicked up, Hall B beam is passed on zero crossing while Hall C beam is kicked down. After the RF separators, the three beams meet the Lambertson magnet which kicks Hall A beam to the right by entering the upper aperture, Hall B beam is undeflected and enters the middle aperture, while Hall C beam is deflected to the left by entering the lower aperture. Only Hall D can receive six pass beam by directing the beam towards the BS_{xx} line and the beam is extracted by using septum magnets.

The bunch length measurement is important for CEBAF operation because a bunch that is too long will increase the beam energy spread. The increase of the energy spread will interrupt beam operations due to beam loss or failure to satisfy user requirements. The bunch length is determined using different techniques at different locations with different beam currents. The techniques are either an invasive or non invasive.

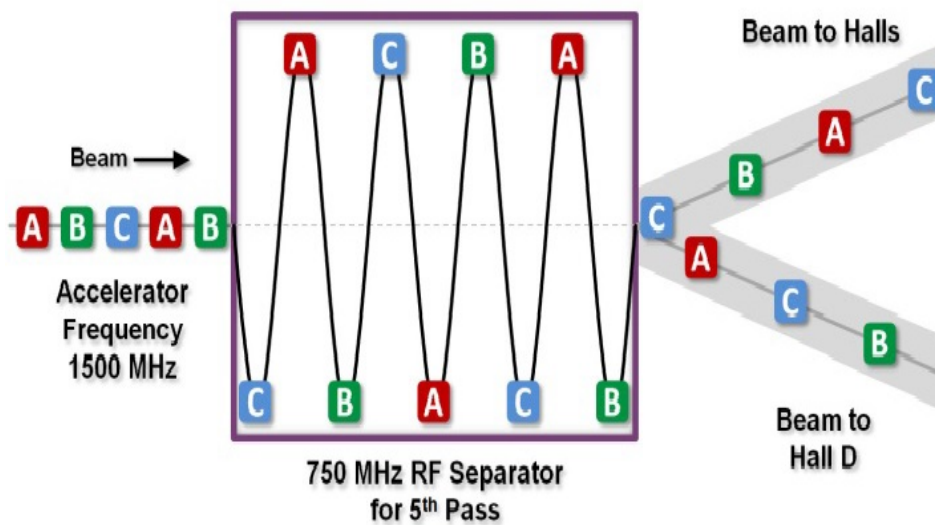


FIG. 5: 749.5 MHz separation with all the buckets are filled [1].

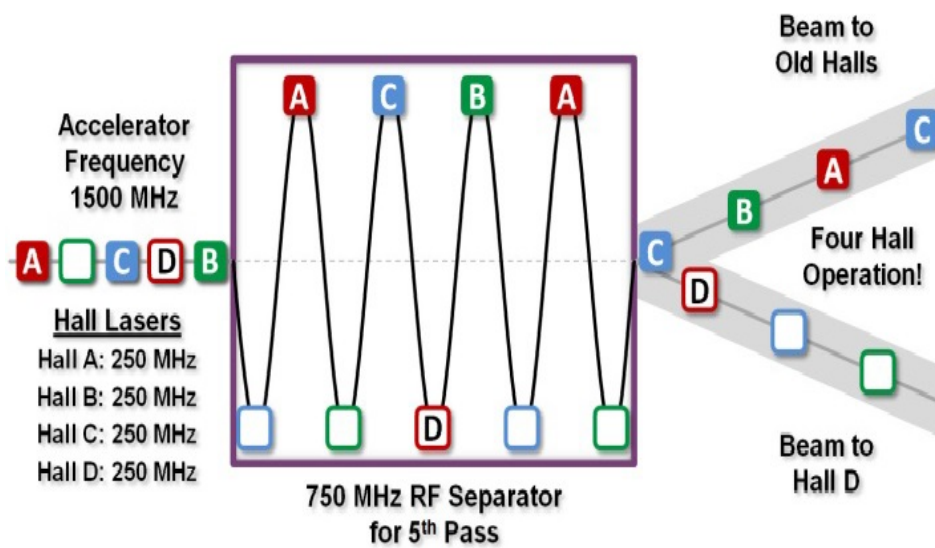


FIG. 6: 749.5 MHz separation with some empty buckets [1].

The next chapter is a literature review on bunch length measurements that have been completed during the previous two decades. Starting from the first observation of coherent synchrotron radiation, the latest results showing what has been accomplished in the techniques to determine the length of short bunches are given.

Chapter three introduces the theoretical background for the accelerator field including relevant equations of motion, transfer matrices, the beta function, bunch compression, synchrotron radiation, and the derivation of the form factor for different distributions. Chapter four gives a quick view about the far-infrared components that are used in the real time interferometer experiment and chapter five summarizes some of the bunch length measurement techniques showing the advantages and disadvantages of each technique.

Finally chapter six shows the bunch length measurements that have been done in CEBAF and the results. In the injector line, an invasive measurement was made using the slit-scan method and a new non-invasive method, using a Brock cavity, was completed. The two techniques are compared to ASTRA simulations. Back-phasing measurement was completed in the 4D line before the injector chicane while an investigation of the new non invasive technique, using real time interferometer, was done at the end of the injector chicane after the bunch was fully compressed. An invasive technique, using synchrotron light monitor (SLM), was used in ARC1 and ARC2. The SLM result is compared to the results of back-phasing.

CHAPTER 2

LITERATURE REVIEW OF BUNCH LENGTH MEASUREMENTS

2.1 INTRODUCTION

In this chapter, some of the bunch length measurements that are done by other scientists are documented. The review starts with the first observation of coherent synchrotron radiation (CSR), the verification of the current squared dependence of CSR experimentally, and the effect of shielding on CSR. The other parts of the review encompass frequency domain techniques, the transverse cavity technique, the energy-modulation technique, and laser based techniques. This section is ordered historically for each technique. The purpose of the review is to give a quick survey of what has been accomplished in bunch length measurement and to show that as the bunch become shorter and shorter, the measurements become more challenging.

2.2 BUNCH LENGTH MEASUREMENTS REVIEW

In 1989 Nakazato, et al., [2] first observed coherent synchrotron radiation (CSR) experimentally from short electron bunches at 180 MeV in the Tohoku 300 MeV linac. The radiation was observed when the electrons passed a bending magnetic field of strength 0.247 T.

Measurements by Blum, et al., [3] showed that the intensity of the far infrared radiation from a short bunch passing through a vertical 0.44 T magnetic field is proportional to the square of the number of electrons in the bunch. As they increased the current, the results deviated from the strict scaling behavior due to the changes in the bunch length.

Kato, et al., [4] verified the suppression of CSR by conducting boundaries, a result expected theoretically since CSR was first discussed [5]. They used a 50 MeV beam and a bending magnet with field strength of 68.6 mT. The CSR passed through finite parallel aluminum shields with thickness 1 mm, the distance between the shields could be varied from 81 mm to 14 mm, and a polarizing interferometer was used to measure the synchrotron

radiation. The suppressed CSR intensity can be explained by the results of Nodvick and Saxon [5], and the total incoherent synchrotron radiation does not change due to the conducting boundaries.

At Brookhaven National Lab, the effect of CSR shielding was studied in a 40 cm long dipole magnet with a bending angle of 20° by Yakimenko, et al., [6]. Two vertically spaced aluminum sheets were used and the gap between the plates was varied from 0 to 14 mm. The two sheets were 70 cm long to cover the edge field region of the dipole. The beam energy spectrum was measured using a beam profile monitor as a function of the gap between the shielding plates. The results showed that at 1 mm separation, the energy loss and the energy spread induced by the CSR was suppressed.

Shibata, et al., [7] measured coherent transition radiation (CTR) in Osaka University. They passed a 28 MeV electron beam through an aluminum foil of thickness 15 mm. The TR was reflected by a plane mirror to another collecting mirror with an acceptance angle of 60 mrad and the radiation was detected by a liquid-He-cooled Si bolometer. The results showed that the observed radiation was coherent and the angular distribution of CTR for different wavelengths (λ) is nearly symmetric with respect to the beam axis and emitted in a cone, consistent with expectations.

In 1995 Wang, et al., [8] used a GaAs Schottky whisker diode at the end of the CEBAF injector to detect CSR. The beam energy was 45 MeV with bunch train of 100 μ s duration and the bunches were separated by 2 ns. The results showed that the CSR power increased as the bunch length became shorter. The spectrum coming from the shorter bunch length covered the spectrum coming from the longer bunch length because the CSR power for the short bunch is greater than the CSR power of the longer bunches. Also, the square law current dependence was verified. The detector had a good sensitivity for bunch lengths between 0.1 and 0.5 ps but its deficiency was that it could not measure the longitudinal profile directly, so it had to be calibrated by another sensitive device.

A bunch length experiment was conducted at the TESLA Test Facility (TTF) by Leissner, et al., [9]. They used a Martin-Pupplett interferometer to determine the auto-correlation of CTR produced by a thin metal film. Two pyrodetectors were used to measure at sub-millimeter wavelengths. The sum of the two detector signals gave the total radiation power entering the interferometer. The *rms* bunch length was 2 ps with analysis error of 20% to 30%. As above, they found that the total signal detected by the pyrodetectors increased as the bunch length became shorter.

Geitz, et al., [10] used a Josephson junction to determine the longitudinal charge distribution. The junction was made from $\text{YBa}_2\text{Cu}_3\text{O}_{7-x}$ and it was exposed to transition radiation in the millimeter and sub-millimeter range. The current-voltage curve had a current step δI at a certain voltage and this step was proportional to the power of the incident radiation. By applying a Hilbert transformation to the current-voltage relation, the form factor (defined in Section 3.7) of the bunch was determined.

Castellano, et al., [11] measured coherent diffraction radiation (CDR) at the TESLA test facility at DESY using a Martin-Puplett interferometer. They used a variable width slit with two halves. When the two halves were closed together transition radiation is emitted. The slit was opened, allowing the beam to pass through the slit, and diffraction radiation was generated. The experiment allowed CDR to be compared to CTR under the same beam conditions. The normalized CDR spectra was plotted for different slit widths. The shape of the coherent spectra shows that the low frequency response was suppressed and the intensity was independent of the slit width. At higher frequencies the slit width had an effect on the radiation. The results were compared to a theoretical calculations and there was good agreement except for wider slit widths of 8 mm and 10 mm. The DR experiments showed the dependence of the radiation intensity on the electron beam position with respect to the slit center.

Perez, et al., [12] measured the bunch length and beam size at the ANKA storage ring. The bunch length had been measured by using a bunch spectrum obtained with an annular electrode and a spectrum analyzer up to 8 GHz. They did the bunch length measurements as a function of energy and current. They found that above 1 GeV the bunch length was in good agreement with the theoretical predictions implying that the beam is longitudinally stable. However at less than 1 GeV the bunch length was oscillating between 10 and 18 mm; the beam was longitudinally unstable. Simultaneously beam size measurements were performed using two monitors. One was located in a dispersive section while the other was in a non-dispersive section. Transverse size measurements from the non-dispersive region were not oscillating. On the other hand, measurements from the dispersive region could not be analyzed because the bunch was oscillating, indicating the beam energy oscillated.

Yamamoto, et al., [13] measured the bunch length using an avalanche photo-diode at the AURORA ring. The fundamental frequency was 190.86 MHz and the measured spectrum had higher harmonics up to the sixth harmonic with decreasing amplitude as the order increases. Results showed that the bunch length determined by a photo diode were in fair agreement compared to those which were determined from a streak camera measurement

and by theoretical calculations.

Evtushenko, et al., [14] measured the bunch length at the Jefferson Lab FEL using a modified Martin-Puplett interferometer and a Fourier transform infrared (FTIR) interferometer. The modified Martin-Puplett interferometer was used to measure coherent transition radiation (CTR) while FTIR was used to measure CSR. The interferometers were installed in the accelerator vault right next to the beam line. The FTIR received CSR coming from the last dipole of the magnetic compressor. The difference between the two interferometers is that the path length in the FTIR is changed by using a mirror moving at constant velocity during the scan. The bunch length measurements were done as a function of average beam current and showed that the bunch length did not change as the current changed. Results of the two measurements agreed within 15%. Also results showed that the bunch length at the wiggler depended strongly on the bunch charge. The CSR spectra showed a local minima due to the water vapor absorption and to overcome this data corruption, future measurements will utilize an interferometer working in vacuum.

Kondo, et al., [15] used non-destructive bunch length monitors to measure bunch lengths from 10 ps to 30 fs during the commissioning of SACLA in Japan. The monitors were placed at the three bunch compressors. The CSR is focused onto a pyro-detector with frequency range from 0.1 to 30 THz. The radiation intensity as a function of the beam charge was measured and it was proportional to the square of the beam charge. The bunch length was varied by changing the RF phase of an s-band bunching cavity and a correlation between the bunch length and CSR intensity was determined. The correlation showed that the CSR intensity is linearly proportional to the RF phase. The sensitivity of the non-destructive monitor to bunch length was determined to be 5%.

Wesch, et al., [16] measured CTR with the aid of a spectrometer consisting of five consecutive reflection gratings to measure the bunch length in two ranges. The first range is from 5 μm to 44 μm and the second is from 45 μm to 430 μm . The first grating disperses wavelengths less than 44 μm to a detector array while wavelengths greater than 45 μm are reflected to a second grating. Each remaining grating disperses a certain range of wavelengths and reflects the remaining wavelengths to the next grating. A circular arc consisting of 30 pyro-detectors is used to record the diffracted radiation for each grating. Different bunch lengths and bunch structures were created and measured to prove the performance of the spectrometer. A transverse deflecting microwave structure (TDS) was used to cross calibrate the longitudinal profile of the electron bunches. Three bunch shapes were used during the commissioning and results showed that a very good agreement for the form factor which is

calculated by the two methods.

Thangaraj, et al., [17] used a real time interferometer (RTI) to measure the bunch length in the A_0 photo injector at Fermilab. The bunch length was varied between 240 μm and 450 μm (FWHM), measured with the RTI, and compared to a streak camera and a Martin-Pupplet interferometer (MPI). Results showed that the auto-correlation measured from the RTI and MPI are in good agreement but at lower frequencies (0.1 THz to 0.3 THz) are in conflict due to problematic differences in the size of the detectors which cause diffraction effects leading to a different low frequency response. The RTI measurement was compared to the streak camera measurements and they are in good agreement for bunch lengths less than 300 μm . At longer bunch lengths, the agreement is not good due to the poor frequency response of the pyro-detector in the RTI.

Nozowa, et al., [18] used a Michelson interferometer to determine the bunch length by measuring the auto-correlation of CTR. The CTR is measured by using two detectors, a mercury cadmium telluride (MCT) photo conductive detector and a liquid helium cooled silicon bolometer, with different spectral ranges. The total measurement range is from 3 to 50 THz. The sensitivity of the bolometer is from 3 to 15 THz while the MCT sensitivity is from 11 to 50 THz. The bolometer is used for bunch lengths longer than 20 fs while MCT is used for bunch lengths shorter than 20 fs. A sensitivity model and a filtered model are used to analyze the data. The sensitivity model estimated the bunch length to be 8.9 fs while the filtered model estimated it to be 14 fs. The sensitivity model explained the experimental interferogram better than the filtered model because the filtered model did not include the frequency dependence of the detection system. The interferogram measured with the bolometer gave a bunch length of 26 fs, the difference between the results from the two detectors is explained by the limited sensitivity of the bolometer at high frequency.

Carlsten, et al., [19] used a transverse deflecting cavity to measure the bunch length at Los Alamos National Laboratory. The charges were compressed from 10-15 ps to less than 1 ps (FWHM) using a magnetic chicane at 8 MeV. The bunch length at low charges (0.1 nC) was measured by the fast deflector cavity while at higher charges (1.1 nC), the bunch length was inferred from the induced beam energy spread at the spectrometer.

Akre, et al., [20] measured the bunch length using a transverse RF deflecting cavity. The RF cavity was operated near the zero-phase at 2856 MHz to sweep the transverse beam perpendicular to the direction of propagation. The amplitude and phase of the cavity were varied. The cavity was calibrated by observing the beam position (Y) on a downstream BPM as the RF phase was changed. When the beam size was minimum, the corresponding RF

voltage indicated how much crabbing was applied to eliminate the wake field in the bunch. The bunch length was measured as a function of the beam line compressor voltage and bunch length with smaller error bars were found around the minimum because the beam is more Gaussian.

Sakaue, et al., [21] developed an RF deflector system for measuring the longitudinal profile of an electron bunch from an RF photo-cathode gun. They built a rectangular shaped s-band standing wave RF cavity that can sweep the bunch with a transverse magnetic field. The deflector cavity is designed with two cells and has a resonant RF frequency of 2856 MHz. They found that the temporal resolution (*rms*) is 147.6 fs during operation with an RF input power of 740 kW. An electron energy of 4.82 MeV, a drift length of 0.72 m, and initial beam size of 313 μm were present during the measurement. The temporal profiles at RF phases of 20° and 40° showed a good agreement between experimental results and GPT simulation calculations. Also, they studied the effect of space charge on the temporal profile at 1070 pC and 240 pC bunch charge. The temporal profile at 1070 pC seemed to take a top-hat like form and the 240 pC temporal profile had a Gaussian distribution. They found the space charge changed the temporal profile drastically from Gaussian to a top-hat as the bunch charge increased.

Fitch, et al., [22] performed an experiment at Fermilab to measure the bunch length using an electro-optic crystal. A short pulse laser was used as a probe for the field induced in a LiTaO_3 crystal by the beam. The LiTaO_3 crystal was mounted in vacuum to avoid the perturbation of electric field due to conduction, the probe laser passes through the crystal, and the polarization change was detected by two photodiodes. The bunch profile was measured by varying of the delay between the probe laser and the bunch.

Yan, et al., [23] measured the longitudinal profile using an ultrafast electro-optic sensor. Results showed that the electric field profile at the entrance of an undulator had a large positive peak which was the direct field of the bunch and another smaller signal which came from the wake field. The electron bunch profile was changed by the prebuncher and the shortest bunch was 1.7 ± 0.2 ps (FWHM).

Berden, et al., [24] used an electro-optic detector (EOD) and a transverse deflecting structure (TDS) to measure the longitudinal profile at the soft X-ray free electron laser at Hamburg (FLASH). The TDS method was used to investigate the faithfulness of the (EO) method. Results showed that the TDS signal consisted of narrow peak and a shoulder with *rms* width less than 30 fs, while the EO signal had only a peak with *rms* width equal to 60 fs and a higher intensity in the tail of the bunch due to the wake-field. The wake-field did not

appear in the TDS signal because the TDS streaked the bunch charge and TDS is insensitive to electromagnetic fields (wake-field). By changing the bunches to wide bunches, TDS and EO measurements had a very good agreement and the simulated EO measurements agreed with the measured EO data except for the tail because of the wake-field.

Wang, et al., [25] used the RF zero-phasing technique to measure the bunch length at Jefferson Lab. The head and tail of a bunch at zero phase in an accelerating cavity will receive different amount of energy. When it traverses a dipole, the dispersion after a dipole magnet is used to detect the energy chirp as a spot size increase. The agreement between the measured and simulated results was excellent and the CSR power increased as the bunch length became shorter. According to the authors opinion, this measurement was the first accurate measurement for bunch length less than 100 fs.

A bunch length monitor that is based on coherent Smith-Purcell radiation was constructed by Ayzatsky, et al. [26]. The monitor consists of a copper diffracting grating with a period of 8 mm and a calibrated detector. Results showed that the radiation power depends on the distance between the beam axis and the highest point on the grating surface. The bunch length of the beam at the grating was determined by using simulations and found to be 2.5 mm. Also, the observed coherent radiation came from the grating, but also from a discontinuity of the beam pipe.

Korbly, et al., [27] used Smith-Purcell radiation (SPR) to do bunch length measurements. The grating was made of oxygen-free high thermal conductivity copper. Two types of grating are used with periods of 10 mm and 6 mm. The over all length of both of them is 10 cm with a 10^0 blaze angle. The grating is set at 0.75 mm away from the beam centroid and the grating height can be controlled by using two stepper motors. The SPR is sent through a controlled copper mirror before it hit a Si-bolometer. The results showed that the dependence of the radiation on current and beam height is in good agreement with the theoretical calculations and the bunch length is found to be 1 ± 0.2 ps for long bunches. For short bunches, the bunch length is found to be 600 ± 200 fs.

Lumpkin [28] provided a review of RF deflector cavity and streak camera measurements of bunch length. He showed some examples of time domain measurements and compared the results of Carlston, et al., [19] and Takahashi, et al. [29]. His conclusion was that the time domain diagnostics could play a critical role in the development of microbunched beams in the future.

Geitz summarized some bunch length measurements in [30]. He classified the measurements into two categories, the first category is the time domain measurements such as streak

camera and RF kicker cavity. The second category is the frequency domain such as fourier transform spectroscopy and hilbert transform spectroscopy. Geitz concluded that the frequency domain measurements are good for short bunches but take more time for data acquisition. On the other hand, they may be non-invasive to the beam being measured.

CHAPTER 3

THEORETICAL BACKGROUND

3.1 CHARGED PARTICLE IN A MAGNETIC FIELD

In order to describe the motion of a particle in a magnetic field, a coordinate system (x, y, s) is introduced where the normal horizontal and vertical axes are x and y respectively while s is along the beam direction. Assume a reference particle moves parallel to the s direction $v = (0, 0, v_s)$ and the magnetic field has transverse components $B = (B_x, B_y, 0)$. When the particle moves through the magnetic field, there will be an acceleration due to the Lorentz force

$$F = e(E + v \times B). \quad (1)$$

Equating the acceleration in the circular motion to the Lorentz force due to a magnetic field and assuming that the particle moves in the horizontal plane,

$$-ev_s B_y = \frac{-mv_s^2}{\rho} \quad (2)$$

$$\frac{1}{\rho(x, y, s)} = \frac{eB_y(x, y, s)}{mv_s} = \frac{e}{p} B_y(x, y, s), \quad (3)$$

where m is the particle mass and ρ is the radius of curvature of the trajectory. For a relativistic particle, the relativistic mass γm should be used where $\gamma = 1/\sqrt{1 - \beta^2}$. The product of the field and the bend radius ($B\rho = p/e$), depends only on the particle relativistic momentum and charge. It does not depend (directly) on the relativistic energy or particle type.

3.2 TRANSFER MATRICES

The transverse equations of motion for ring accelerators [31] which only bends in the horizontal plane must be generalized for CEBAF, where there are a vertical deflections. Including both the horizontal and vertical bending, the equations of motion are given by

$$\begin{aligned} x''(s) + \left(\frac{1}{R_x^2(s)} + k(s) \right) x(s) &= \frac{1}{R_x(s)} \frac{\Delta p}{p} \\ y''(s) + \left(\frac{1}{R_y^2(s)} - k(s) \right) y(s) &= \frac{1}{R_y(s)} \frac{\Delta p}{p}, \end{aligned} \quad (4)$$

where x and y are the transverse coordinates, s is the longitudinal coordinate, R is the radius of curvature, $k = B'/B\rho$ is the quadrupole focussing strength, and $\Delta p/p$ is the relative momentum error. Transverse matrix models for beam dynamics are made by assuming that the fields are constant along the beam axis and the fields begin and end suddenly at the beginning and ending of the magnets. The sign of the quadrupole strength k follows the normal convention that when k is greater than zero the quadrupole is focusing in the horizontal plane and it is defocusing in the vertical plane.

Start with the case when the particle goes through a focusing quadrupole. In this case there is no bending to the beam and $1/R = 0$. Using Eq. (4) and consistent with the previous assumptions (working in the x coordinates and similarly for the y coordinates), then

$$x''(s) + kx(s) = 0. \quad (5)$$

When k is greater than zero, Eq. (5) will have a solution given by

$$\begin{aligned} x(s) &= A \cos(\sqrt{k}s) + B \sin(\sqrt{k}s) \\ x'(s) &= -\sqrt{k}A \sin(\sqrt{k}s) + \sqrt{k}B \cos(\sqrt{k}s). \end{aligned} \quad (6)$$

Using the boundary condition which state that when $s = 0$, $x(s) = x_0$ and $x'(s) = x'_0$ then Eq. (6) gives

$$\begin{aligned} x(s) &= x_0 \cos(\sqrt{k}s) + \frac{x'_0}{\sqrt{k}} \sin(\sqrt{k}s) \\ x'(s) &= -x_0 \sqrt{k} \sin(\sqrt{k}s) + x'_0 \cos(\sqrt{k}s). \end{aligned} \quad (7)$$

Using $\phi = (\sqrt{k}s)$ and writting these equations as a transfer matrix yields

$$\begin{bmatrix} x(s) \\ x'(s) \end{bmatrix} = \begin{bmatrix} \cos(\phi) & \frac{1}{\sqrt{k}} \sin(\phi) \\ -\sqrt{k} \sin(\phi) & \cos(\phi) \end{bmatrix} \begin{bmatrix} x_0 \\ x'_0 \end{bmatrix}. \quad (8)$$

For the y -direction Eq. (4) will have a solution given by

$$\begin{aligned} y(s) &= A \cosh(\sqrt{k}s) + B \sinh(\sqrt{k}s) \\ y'(s) &= \sqrt{k}A \sinh(\sqrt{k}s) + \sqrt{k}B \cosh(\sqrt{k}s). \end{aligned} \quad (9)$$

Using the same boundary conditions with the same techniques and defining $\phi = (\sqrt{k}s)$, the transfer matrix for the defocusing quadrupole is

$$\begin{bmatrix} y(s) \\ y'(s) \end{bmatrix} = \begin{bmatrix} \cosh(\phi) & \frac{1}{\sqrt{k}} \sinh(\phi) \\ \sqrt{k} \sinh(\phi) & \cosh(\phi) \end{bmatrix} \begin{bmatrix} y_0 \\ y'_0 \end{bmatrix}. \quad (10)$$

From the above discussion, the transfer matrix for a quadrupole focusing in the horizontal and defocusing in the vertical plane is given by

$$\begin{bmatrix} x(s) \\ x'(s) \\ y(s) \\ y'(s) \end{bmatrix} = \begin{bmatrix} \cos(\phi) & \frac{1}{\sqrt{k}} \sin(\phi) & 0 & 0 \\ -\sqrt{k} \sin(\phi) & \cos(\phi) & 0 & 0 \\ 0 & 0 & \cosh(\phi) & \frac{1}{\sqrt{k}} \sinh(\phi) \\ 0 & 0 & \sqrt{k} \sinh(\phi) & \cosh(\phi) \end{bmatrix} \begin{bmatrix} x_0 \\ x'_0 \\ y_0 \\ y'_0 \end{bmatrix}. \quad (11)$$

When $k < 0$, the diagonal blocks should be swapped and $|k|$ used in place of k .

When k equals zero, Eq. (5) will have a solution given by

$$\begin{aligned} x(s) &= x_0 + sx'_0 \\ x'(s) &= x'_0, \end{aligned} \quad (12)$$

and the transfer matrix for a drift is

$$\begin{bmatrix} x(s) \\ x'(s) \end{bmatrix} = \begin{bmatrix} 1 & s \\ 0 & 1 \end{bmatrix} \begin{bmatrix} x_0 \\ x'_0 \end{bmatrix}. \quad (13)$$

Next, it is possible to obtain the transfer matrix for a dipole magnet. Since the dipole has no focusing effect ($k = 0$) and all the particles have minimum momentum deviation ($\Delta p/p = 0$), then Eq. (4) will be

$$x''(s) + \frac{1}{R_x^2} x(s) = 0. \quad (14)$$

Similarly to the previous procedure, the solution of Eq. (14) is

$$\begin{aligned} x(s) &= x_0 \cos\left(\frac{s}{R_x}\right) + x'_0 R_x \sin\left(\frac{s}{R_x}\right) \\ x'(s) &= -\frac{x_0}{R_x} \sin\left(\frac{s}{R_x}\right) + x'_0 \cos\left(\frac{s}{R_x}\right). \end{aligned} \quad (15)$$

Since the dipole magnet bends only in one direction and assuming this direction is the horizontal direction then the vertical direction can be considered as a drift. Denoting the total bending angle by $\theta = s/R_x$, the transfer matrix is

$$\begin{bmatrix} x(s) \\ x'(s) \\ y(s) \\ y'(s) \end{bmatrix} = \begin{bmatrix} \cos(\theta) & R_x \sin(\theta) & 0 & 0 \\ -\frac{1}{R_x} \sin(\theta) & \cos(\theta) & 0 & 0 \\ 0 & 0 & 1 & s \\ 0 & 0 & 0 & 1 \end{bmatrix} \begin{bmatrix} x_0 \\ x'_0 \\ y_0 \\ y'_0 \end{bmatrix}. \quad (16)$$

This matrix applies to a sector magnet where there is no edge focusing.

The bending magnet field begins and ends sharply along the particle trajectory in a rectangular dipole. The previous matrix needs to be corrected and edge focusing needs to be considered. The edge focusing matrix for a rectangular dipole magnet in the deflecting plane is given by [32]

$$M_{edge} = \begin{bmatrix} 1 & 0 \\ \tan(\psi)/R_x & 1 \end{bmatrix}, \quad (17)$$

where ψ is the entrance or exit angle and equals $(\theta/2)$. The edge focusing matrix for a rectangular dipole magnet in the nondeflecting plane is given by [32]

$$M_{edge} = \begin{bmatrix} 1 & 0 \\ -\tan(\psi)/R_x & 1 \end{bmatrix}, \quad (18)$$

The complete matrix is obtained by multiplying the edge focusing for the entrance and the exit by the transfer matrix of the dipole. The complete matrix for the rectangular dipole with edge focusing for $\theta \ll 1$ is given by

$$\begin{bmatrix} x(s) \\ x'(s) \\ y(s) \\ y'(s) \end{bmatrix} = \begin{bmatrix} 1 & R_x\theta & 0 & 0 \\ 0 & 1 & 0 & 0 \\ 0 & 0 & \cos(\theta) & R_x \sin(\theta) \\ 0 & 0 & -\sin(\theta)/R_x & \cos(\theta) \end{bmatrix} \begin{bmatrix} x_0 \\ x'_0 \\ y_0 \\ y'_0 \end{bmatrix}. \quad (19)$$

3.3 BETA FUNCTION AND BEAM ENVELOPE

When $\Delta p/p = 0$ in Eq. (4), Hill's equation is obtained

$$x''(s) + k(s)x(s) = 0. \quad (20)$$

The solutions for this equation are given by

$$x(s) = \sqrt{\epsilon\beta(s)} \cos[\psi(s) + \phi], \quad (21)$$

where ϵ , ϕ are integration constants and $\beta(s)$ is the beta function which depends on the beam focusing and changes as the position changes. To define the beam envelope equation, Eq. (21) can be written for particle i with arbitrary phase ϕ_i as

$$x_i(s) = \sqrt{\epsilon\beta(s)} \cos[\psi(s) + \phi_i], \quad (22)$$

Each particle will have its own phase and position. Since there are many particles, they define a beam area (ellipse) in phase space. The beam area consists of a combination of all

individual trajectories of the particles. The maximum transverse position for the ellipse is the beam envelope and equals $\sqrt{\epsilon\beta}$ where ϵ is the beam emittance, defined as the area of ellipse divided by π . Since $|\cos[\psi(s) + \phi_i]| \leq 1$ in Eq. (21) then all particles are contained in

$$-\sqrt{\epsilon\beta(s)} \leq x_i \leq \sqrt{\epsilon\beta(s)}. \quad (23)$$

The particles will have a transverse motion around the orbit in a range managed by the beam envelope as shown in Fig. 7.

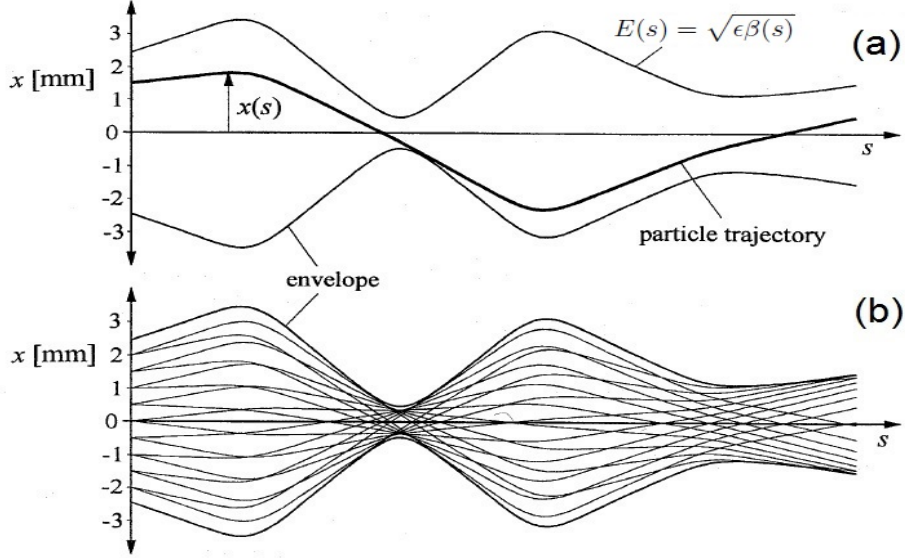


FIG. 7: Particle trajectories for different particles [31]. (a) is for a single particle trajectory while (b) is for 18 different trajectories.

3.4 PHASE SPACE

By differentiating Eq. (21), we obtain

$$x'(s) = \frac{-\sqrt{\epsilon}}{\sqrt{\beta(s)}} \left(\alpha(s) \cos[\psi(s) + \phi] + \sin[\psi(s) + \phi] \right), \quad (24)$$

where $\alpha(s) = -\beta'(s)/2$ and $\phi'(s) = 1/\beta(s)$. To find the equation for the phase space ellipse, the orbit expressions which depend on ψ must be eliminated. From Eq. (21)

$$\cos[\psi(s) + \phi] = \frac{x}{\sqrt{\epsilon}\sqrt{\beta(s)}}, \quad (25)$$

and from Eq. (24)

$$\sin[\psi(s) + \phi] = \frac{\sqrt{\beta(s)}x'}{\sqrt{\epsilon}} + \frac{\alpha(s)x}{\sqrt{\epsilon}\sqrt{\beta(s)}}. \quad (26)$$

Using $\cos^2(\delta) + \sin^2(\delta) = 1$, then

$$\frac{x^2}{\beta(s)} + \left(\frac{\alpha(s)x}{\sqrt{\beta(s)}} + \sqrt{\beta(s)}x' \right)^2 = \epsilon, \quad (27)$$

$$\frac{x^2}{\beta(s)} + \frac{\alpha^2(s)}{\beta(s)}x^2 + \beta(s)x'^2 + 2\alpha(s)xx' = \epsilon, \quad (28)$$

$$\gamma(s)x^2 + 2\alpha(s)xx' + \beta(s)x'^2 = \epsilon, \quad (29)$$

where

$$\gamma(s) = \frac{1 + \alpha^2(s)}{\beta(s)}. \quad (30)$$

Eq. (29) is the phase space ellipse equation and ϵ is the beam emittance. According to Liouville's theorem, as the particles travel along the orbit, the shape and tilt of the ellipse change with $\alpha(s)$ and $\beta(s)$, but the area remains constant. This means that by knowing the area of the ellipse at the beginning of the beam line, we can determine the size of the beam at any place along the orbit without calculating the trajectory for each individual particle if the beta function is known there.

3.5 BUNCH COMPRESSION

There are two methods to achieve bunch compression, the first method is kinematic compression and the second method is magnetic compression. Kinematic compression is only effective for non-relativistic particles while magnetic compression is effective for relativistic particles. Kinematic compression requires a velocity modulation to the bunch. An RF cavity is used to introduce a velocity difference between the particles; the largest velocity change is achieved by setting the bunch at zero crossing in an accelerating RF wave. At zero crossing, the tail particles will receive added energy while the head particles will receive an energy decrease. After traversing a drift, the bunch length is decreased; the bunch is compressed. The M_{56} is the transfer matrix element that gives how much change in longitudinal offset happens to an off-momentum particle ($\Delta z = M_{56}\delta$), where $\delta = \Delta p/p$ is the relative momentum deviation of the particle. The M_{56} for a path of length L is equal to L/γ^2 . For mathematical derivation see APPENDIX B.

3.5.1 KINEMATIC COMPRESSION

Since the drift matrix, beam size matrix, and $(\beta_L, \alpha_L, \gamma_L)$ transforms exactly the same way as the transverse parameters [33], then the longitudinal drift matrix¹ is given by

$$\begin{bmatrix} z \\ \delta \end{bmatrix}_2 = \begin{bmatrix} M_{55} & M_{56} \\ M_{65} & M_{66} \end{bmatrix} \begin{bmatrix} z \\ \delta \end{bmatrix}_1 = \begin{bmatrix} 1 & L/\gamma^2 \\ 0 & 1 \end{bmatrix} \begin{bmatrix} z \\ \delta \end{bmatrix}_1, \quad (31)$$

where L is the drift length and the subscript (1) indicates the beginning location while (2) indicates the end location. The beam size matrix is given by

$$\Sigma_L = \begin{bmatrix} \langle z^2 \rangle & \langle z\delta \rangle \\ \langle z\delta \rangle & \langle \delta^2 \rangle \end{bmatrix} = \begin{bmatrix} \sigma_z^2 & \sigma_{z\delta}^2 \\ \sigma_{z\delta}^2 & \sigma_\delta^2 \end{bmatrix} = \epsilon_L \begin{bmatrix} \beta_L & -\alpha_L \\ -\alpha_L & \gamma_L \end{bmatrix}, \quad (32)$$

where σ_z is the longitudinal *rms* beam size, σ_δ is the *rms* momentum spread, $\sigma_{z\delta}$ is the *rms* chirp correlation, and $(\beta_L, \alpha_L, \gamma_L)$ are the longitudinal Twiss parameters². The chirp correlation can be changed by changing the RF voltage or phase. The longitudinal Twiss parameters at the end location are given by

$$\begin{bmatrix} \beta_L \\ \alpha_L \\ \gamma_L \end{bmatrix}_2 = \begin{bmatrix} M_{55}^2 & -2M_{55}M_{56} & M_{56}^2 \\ -M_{55}M_{65} & M_{55}M_{66} + M_{56}M_{65} & -M_{56}M_{66} \\ M_{65}^2 & -2M_{65}M_{66} & M_{66}^2 \end{bmatrix} \begin{bmatrix} \beta_L \\ \alpha_L \\ \gamma_L \end{bmatrix}_1. \quad (33)$$

Using the corresponding values for M_{55} and M_{56} from the drift matrix.

$$(\beta_L)_2 = (\beta_L)_1 - \frac{2L}{\gamma^2}(\alpha_L)_1 + \frac{L^2}{\gamma^4}(\gamma_L)_1, \quad (34)$$

and since $\sigma_z^2 = \epsilon_L \beta_L$ and $\sigma_\delta^2 = \epsilon_L \gamma_L$

$$(\sigma_z^2)_2 = (\sigma_z^2)_1 + \frac{2L}{\gamma^2}(\sigma_{z\delta}^2)_1 + \frac{L^2}{\gamma^4}(\sigma_\delta^2)_1, \quad (35)$$

$$(\sigma_z)_2 = \sqrt{\langle z^2 \rangle} = \sqrt{\langle z^2 \rangle_1 + \frac{2L}{\gamma^2} \langle z\delta \rangle_1 + \frac{L^2}{\gamma^4} \langle \delta^2 \rangle_1}. \quad (36)$$

Eq. (36) gives the value of the bunch length after moving through a drift of length L and the calculations using this equation at different correlation values $\sigma_{z\delta}$ are shown in Fig. 8. The kinematic compression will compress the bunch to the smallest value and the shortest distance when the chirp is maximum. As the chirp decreases the bunch compression decreases and the distance becomes longer to achieve the compression. When γ goes to infinity, Eq. (36)

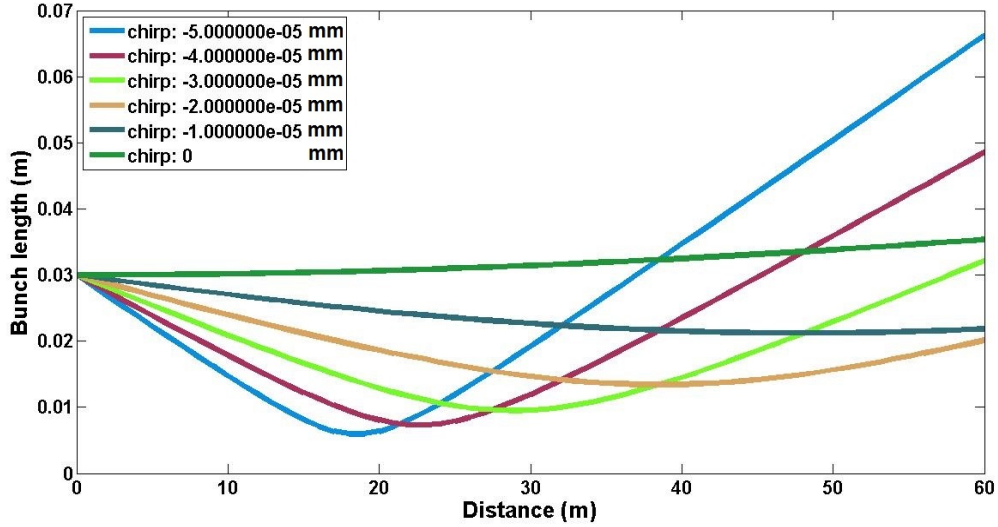


FIG. 8: Bunch compression using kinematic compression at 130 keV for different chirp

states that the bunch will not compress because the particles are relativistic, and magnetic compression is needed to compress the particles.

3.5.2 MAGNETIC COMPRESSION

Magnetic compression is done by introducing a bunch chirp correlation at the entrance of a magnetic chicane followed by propagation through a chicane with $M_{56} \neq 0$. As in the kinematic compression, the bunch chirp correlation is done by setting the bunch off-crest of an RF wave, so the tail will receive a higher amount of energy than the head. The tail moves a shorter path through the magnetic chicane while the head will move a longer path due to the effect of the slightly different magnetic rigidity of the particles. At the end of the chicane, the tail is closer to the head and the bunch is compressed as shown in Fig. 9.

To know how much the bunch is compressed, a magnification factor should be calculated. The general equation for longitudinal phase space is given by³

$$\gamma(\Delta z)^2 + 2\alpha(\Delta z)(\Delta E) + \beta(\Delta E)^2 = \epsilon, \quad (37)$$

where Δz is the longitudinal offset and ΔE is the energy offset. By compression, we desire to decrease the Δz extent of the ellipse describing the particles. The transformation array

¹Derivation is provided by Todd Satogata

²Not to be confused with $\beta = v/c$ and γ the relativistic factors

³Derivation is done with the help of Geoffrey Krafft

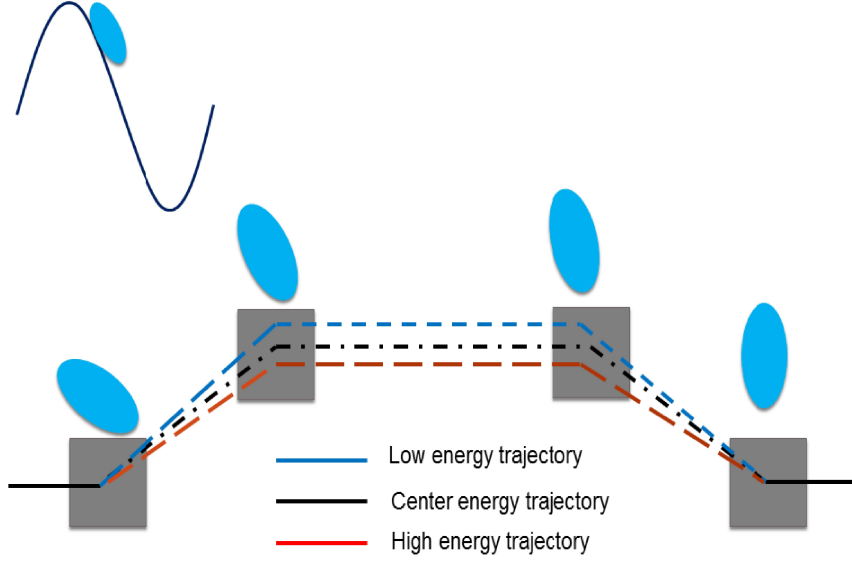


FIG. 9: Bunch compression through a magnetic chicane

is given by Eq. (33) and the ellipse Twiss parameters after transformation will be

$$(\beta_L)_2 = M_{55}^2(\beta_L)_1 - 2M_{55}M_{56}(\alpha_L)_1 + M_{56}^2(\gamma_L)_1, \quad (38)$$

$$(\alpha_L)_2 = -M_{55}M_{65}(\beta_L)_1 + (M_{55}M_{66} + M_{56}M_{65})(\alpha_L)_1 - M_{56}M_{66}(\gamma_L)_1, \quad (39)$$

$$(\gamma_L)_2 = M_{65}^2(\beta_L)_1 - 2M_{65}M_{66}(\alpha_L)_1 + M_{66}^2(\gamma_L)_1, \quad (40)$$

Assume that the longitudinal phase space distribution is a horizontal upright ellipse before compression with Δz_0 and ΔE_0 as the initial values for the bunch length and energy respectively. After the compression it will be Δz_{opt} and ΔE_{opt} as shown in Fig. 10. Let m be the magnification factor, so the bunch length will be compressed by a factor $1/m$.

After the chirp by the RF cavity, the horizontal upright ellipse will transform into a tilted ellipse and the transformation equation is given by

$$\begin{bmatrix} \Delta z_1 \\ \Delta E_1 \end{bmatrix} = \begin{bmatrix} 1 & 0 \\ -s & 1 \end{bmatrix} \begin{bmatrix} \Delta z_0 \\ \Delta E_0 \end{bmatrix}, \quad (41)$$

where $s = 2\pi V \sin \phi / \lambda$, V is the cavity offset voltage, λ is the RF wavelength, and ϕ is the offset phase from the crest in radians. Using the same technique as discussed before in Eq. (38), Eq. (39), and Eq. (40) and noticing that $\alpha_0 = 0$ when the ellipse is horizontal upright, then the new Twiss parameters are

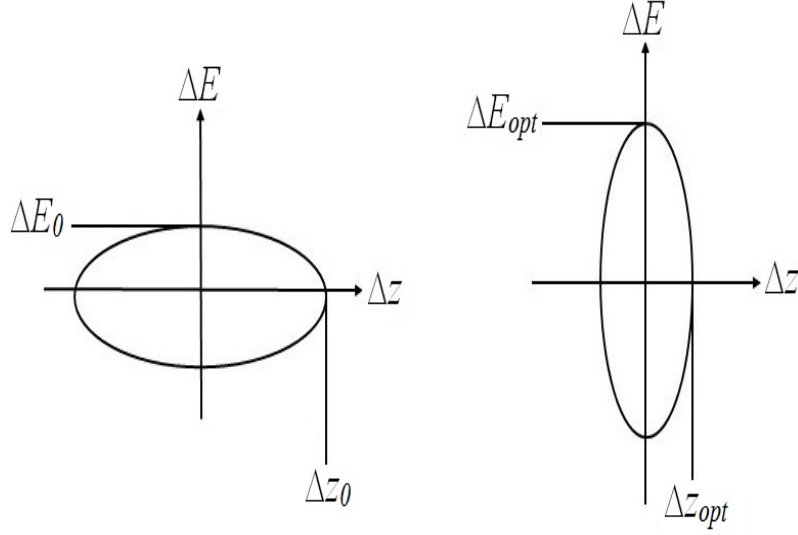


FIG. 10: Phase space before and after compression

$$\beta_1 = \beta_0, \quad (42)$$

$$\alpha_1 = s\beta_0, \quad (43)$$

$$\gamma_1 = \gamma_0 + s^2\beta_0. \quad (44)$$

The amplification factor m is defined as the old horizontal distance divided by the new horizontal distance, so $m = \sqrt{\gamma_1\epsilon/\gamma_0\epsilon}$.

Since $\epsilon = \Delta_{z0}\Delta_{E0}$, $\Delta_{z0} = \sqrt{\beta_0\epsilon}$, and $\Delta_{E0} = \sqrt{\gamma_0\epsilon}$, then

$$\beta_0 = \frac{\Delta_{z0}}{\Delta_{E0}}, \quad (45)$$

$$\gamma_0 = \frac{\Delta_{E0}}{\Delta_{z0}}. \quad (46)$$

Square m and substitute the previous values of γ_1 , γ_0 , and β_0 to obtain

$$m^2 = 1 + s^2\frac{\beta_0}{\gamma_0} = 1 + s^2\frac{\Delta_{z0}^2}{\Delta_{E0}^2}. \quad (47)$$

The linear transfer matrix for the chicane is given by

$$\begin{bmatrix} \Delta z_2 \\ \Delta E_2 \end{bmatrix} = \begin{bmatrix} 1 & \frac{M_{56}}{E_{inj}} \\ 0 & 1 \end{bmatrix} \begin{bmatrix} \Delta z_1 \\ \Delta E_1 \end{bmatrix}, \quad (48)$$

where E_{inj} is the energy at which the compression is done. Again using the same procedure, the final Twiss parameters will be

$$\beta_2 = K^2\gamma_1 - 2K\alpha_1 + \beta_1, \quad (49)$$

$$\alpha_2 = -K\gamma_1 + \alpha_1, \quad (50)$$

$$\gamma_2 = \gamma_1, \quad (51)$$

where $K = M_{56}/E_{inj}$. Since the ellipse transforms into a vertical upright ellipse, so $\alpha_2 = 0$ is required. From Eq. (50) the maximum compression condition becomes

$$K = \frac{\alpha_1}{\gamma_1} = \frac{s\beta_0}{\gamma_0(1 + \frac{s^2\Delta_{z0}^2}{\Delta_{E0}^2})}, \quad (52)$$

$$M_{56} = \frac{E_{inj}s\Delta_{z0}^2}{\Delta_{E0}^2(1 + \frac{s^2\Delta_{z0}^2}{\Delta_{E0}^2})}. \quad (53)$$

From Eq. (47) $m^2 - 1 = s^2\Delta_{z0}^2/\Delta_{E0}^2$ and finally

$$M_{56} = \frac{E_{inj}}{s} \frac{m^2 - 1}{m^2}. \quad (54)$$

So by knowing M_{56} , s , and E_{inj} , the amplification factor can be calculated and the bunch length after compression is known.

3.6 SYNCHROTRON RADIATION

When relativistic particles move around a ring, they emit radiation called Synchrotron Radiation (SR). The first visible SR was observed by Floyd Herber in 1947 at the 70 MeV Synchrotron which was built at General Electric's Schenectady facility. SR has important technical and economic implications on circular electron accelerators because the amount of SR increases rapidly as the particle energy increases. To maintain the electron energy, more power needs to be supplied. To reduce the synchrotron radiation in circular electron accelerators, they need to be built with large circumferences to reduce the power lost by radiation. The SR spectrum has a wide range of frequencies starting from far-infrared up to hard X-rays. Bending magnets and insertion devices are the two main types of SR sources.

3.6.1 BENDING MAGNET

As the relativistic particles go through a bending magnet on a circular path, SR is emitted tangentially from any point on the curved path. The total energy per unit angular frequency emitted by a single electron in one revolution on a circular orbit is given by [34]

$$\frac{dE}{d\omega} = \frac{9\sqrt{3}}{8\pi\omega_c} \frac{e^2\gamma^4}{3\rho\epsilon_0} y \int_y^\infty K_{5/3}(x) dx, \quad (55)$$

where e is the electronic charge, γ is the relativistic factor, ρ is the bending radius, ϵ_0 is the free space permittivity, $K_{5/3}$ is the modified Bessel function, and $y = \omega/\omega_c$, where $\omega_c = 3\gamma^3 c/2\rho$ is the critical angular frequency. The power spectrum is calculated for different bunch lengths (σ) for an electron beam traversing a dipole with bending radius equal to 3.125 m as shown in Fig. 11. When Eq. (55) is integrated over the whole range of ω , the total energy is given by

$$E = \frac{e^2\gamma^4}{3\rho\epsilon_0}. \quad (56)$$

The SR has properties such as a wide spectral range and high collimation with a vertical opening angle of order $1/\gamma$. The radiation is polarized in the orbital plane, and polarized elliptically above and below the orbital plane.

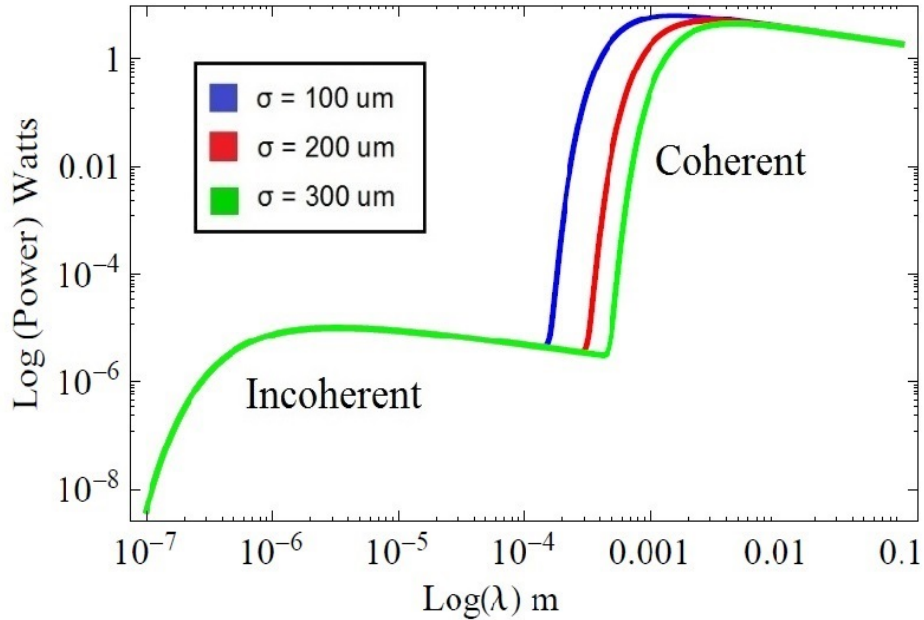


FIG. 11: Power spectrum for 123 MeV electron beam at 300 μA with 499 MHz repetition rate and Gaussian bunches with *rms* length σ .

3.6.2 INSERTION DEVICES

Insertion devices (w wigglers and undulators) are periodic short bending magnets possessing an alternating magnetic field direction installed in straight sections of a storage ring or a linac. As the relativistic particles enter the insertion device, the particles perform a sinusoidal transverse oscillation. During the sinusoidal motion, the particles emit SR with a higher photon flux than in a bending magnet. Each magnetic pole produces a fan in the forward direction and the total flux is equal to the number of poles multiplied by the flux emitted from one magnetic pole. Wigglers and undulators are almost the same except that undulators weakly deflect the particles with an angle less than $1/\gamma$. The maximum trajectory angle is given by [31]

$$\theta_\omega = \frac{K}{\gamma}, \quad (57)$$

where γ is the relativistic factor and $K = 0.9337 \times B(T) \times \lambda_\mu$ where B is the magnetic field in Tesla and λ_μ is the undulator period length in cm. Undulators have $K \leq 1$ and $K > 1$ for wigglers. Due to constructive interference from the emission along an undulator, it produces narrow band SR.

3.7 COHERENT RADIATION AND FORM FACTOR

In calculating the total radiation intensity from a charged particle beam at a certain location, the individual intensity radiated from each particle should be added. The emitted spectrum can be classified into coherent and incoherent regions. The incoherent radiation happens when the bunch length is greater than the wavelength of the radiation while the coherent radiation happens when the bunch length is shorter than the wavelength of the radiation as shown in Fig. 11.

To calculate the coherent and incoherent contribution to the synchrotron radiation, assume that the electric field produced by an electron at position $r = 0$ at wavelength λ is $E(\lambda)$ as shown in Fig. 12 and the intensity is proportional to the square of the electric field [3]

$$I(\lambda) \sim |E(\lambda)|^2. \quad (58)$$

Let the distance between the reference electron and the detector be R and consider the j^{th} electron at position r_j relative to the reference electron. The electric field component from the j^{th} electron is

$$E_j(\lambda) = E(\lambda) \exp\left(\frac{2\pi i n_j \cdot r_j}{\lambda}\right), \quad (59)$$

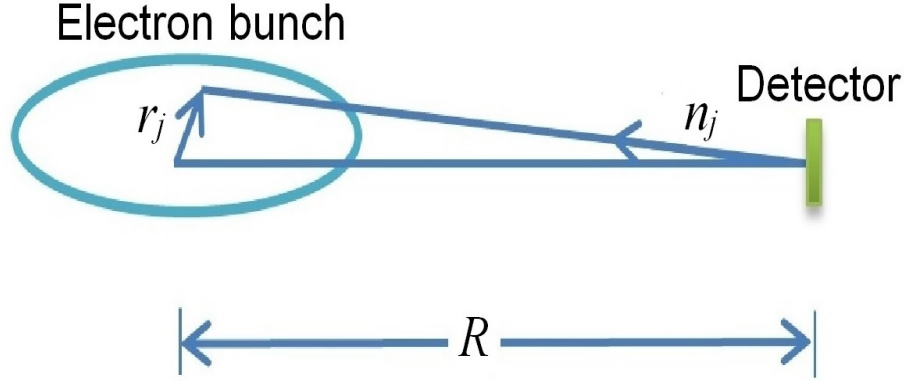


FIG. 12: A diagram to calculate the electric field of a bunch

where n_j is a unit vector directed from the detector to the electron and the total electric field from N electrons is given by

$$E_{total}^2 = |E(\lambda)|^2 \left| \sum_{j=1}^N \exp\left(\frac{2\pi i n_j \cdot r_j}{\lambda}\right) \right|^2. \quad (60)$$

Using Eq. (58), the total intensity from N electrons is given by

$$I_{total} = I(\lambda) \left| \sum_{j=1}^N \exp\left(\frac{2\pi i n_j \cdot r_j}{\lambda}\right) \right|^2, \quad (61)$$

and since $|a|^2 = a\bar{a}$, then

$$I_{total} = I(\lambda) \left[\sum_{j=1}^N \exp\left(\frac{2\pi i n_j \cdot r_j}{\lambda}\right) \sum_{k=1}^N \exp\left(\frac{-2\pi i n_k \cdot r_k}{\lambda}\right) \right]. \quad (62)$$

Because there are N terms for $j = k$ and $N^2 - N$ terms for $j \neq k$

$$I_{total} = I(\lambda) \left[N + \sum_{j=1}^N \sum_{\substack{k=1 \\ j \neq k}}^N \exp\left(\frac{2\pi i [n_j \cdot r_j - n_k \cdot r_k]}{\lambda}\right) \right]. \quad (63)$$

Assume the number of electrons between r and $r + \delta r$ is $NS(r)$, where $S(r)$ is the normalized number density of electrons in the bunch, i.e. $\int S(r) dr = 1$. Since the distribution is

symmetric about $r = 0$, i.e. $S(r) = S(-r)$, the summation of Eq. (63) can be replaced by an integral as follows

$$I_{total} = I(\lambda) \left[N + N(N-1) \int \int \exp\left(\frac{2\pi in \cdot [r - r']}{\lambda}\right) S(r)S(r') dr dr' \right], \quad (64)$$

$$I_{total} = I(\lambda) \left[N + N(N-1) \int \exp\left(\frac{2\pi in \cdot r}{\lambda}\right) S(r) dr \int \exp\left(\frac{-2\pi in \cdot r'}{\lambda}\right) S(r') dr' \right], \quad (65)$$

and using $a\bar{a} = |a|^2$, then

$$I_{total} = I(\lambda) \left[N + N(N-1) \left| \int \exp\left(\frac{2\pi in \cdot r}{\lambda}\right) S(r) dr \right|^2 \right], \quad (66)$$

$$I_{total} = I(\lambda) \left[N + N(N-1) f(\lambda) \right] \quad (67)$$

$$I_{total} = I_{inc}(\lambda) \left[1 + (N-1) f(\lambda) \right],$$

where $I_{inc} = NI(\lambda)$ is the incoherent Synchrotron radiation and $f(\lambda)$ is the form factor

$$f(\lambda) = \left| \int \exp\left(\frac{2\pi in \cdot r}{\lambda}\right) S(r) dr \right|^2. \quad (68)$$

In the far field, the form factor becomes

$$f(\lambda) = \left| \int \exp\left(\frac{2\pi iz}{\lambda}\right) S(z) dz \right|^2, \quad (69)$$

where z is the direction of propagation.

When the bunch length is smaller than the wavelength of the radiation, the form factor becomes one and $I_{total} = N^2 I(\lambda)$, which means that the particles radiate in-phase and the radiation is coherent. When the bunch length is greater than the wavelength of radiation the form factor becomes zero and $I_{total} = NI(\lambda)$. In this case the particles radiate at all phases and the radiation is incoherent. Notice that the coherent radiation intensity increases by a factor N compared to the incoherent intensity.

3.8 FORM FACTOR FOR DIFFERENT DISTRIBUTIONS

3.8.1 KLIMONTVICH DISTRIBUTION

The Klimontovich distribution is defined as

$$S(z) = \frac{1}{N} \sum_{j=1}^N \delta(z - z_j). \quad (70)$$

Substituting in Eq. (69) yields

$$f(\lambda) = \left| \int_{-\infty}^{\infty} \exp\left(\frac{2\pi iz}{\lambda}\right) \frac{1}{N} \sum_{j=1}^N \delta(z - z_j) dz \right|^2, \quad (71)$$

$$f(\lambda) = \left| \frac{1}{N} \sum_{j=1}^N \int_{-\infty}^{\infty} \exp\left(\frac{2\pi iz}{\lambda}\right) \delta(z - z_j) dz \right|^2, \quad (72)$$

$$f(\lambda) = \left| \frac{1}{N} \sum_{j=1}^N \exp\left(\frac{2\pi iz_j}{\lambda}\right) \right|^2, \quad (73)$$

$$f(\lambda) = \frac{1}{N^2} \left| \sum_{j=1}^N \exp\left(\frac{2\pi iz_j}{\lambda}\right) \sum_{k=1}^N \exp\left(\frac{2\pi iz_k}{\lambda}\right) \right|^2, \quad (74)$$

reproducing the result in Eq. (60). This formula is suitable for computing form factors from computer simulations of the longitudinal distribution.

3.8.2 GAUSSIAN DISTRIBUTION

The Gaussian distribution is defined as

$$S(z) = \frac{1}{\sqrt{2\pi\sigma^2}} \exp\left(\frac{-z^2}{2\sigma^2}\right). \quad (75)$$

Substituting in Eq. (69)

$$f(\lambda) = \left| \frac{1}{\sqrt{2\pi\sigma^2}} \int_{-\infty}^{\infty} \exp\left(\frac{2\pi iz}{\lambda}\right) \exp\left(\frac{-z^2}{2\sigma^2}\right) dz \right|^2, \quad (76)$$

$$f(\lambda) = \left| \frac{1}{\sqrt{2\pi\sigma^2}} \int_{-\infty}^{\infty} \exp\left(\frac{-1}{2\sigma^2} \left(z^2 - \frac{4\pi i\sigma^2 z}{\lambda}\right)\right) dz \right|^2. \quad (77)$$

By completing the square

$$f(\lambda) = \left| \frac{1}{\sqrt{2\pi\sigma^2}} \int_{-\infty}^{\infty} \exp\left(\frac{-1}{2\sigma^2} \left[\left(z - \frac{2\pi i\sigma^2}{\lambda}\right)^2 + \frac{4\pi^2\sigma^4}{\lambda^2}\right]\right) dz \right|^2, \quad (78)$$

$$f(\lambda) = \left| \frac{\exp\left(\frac{-2\pi^2\sigma^2}{\lambda^2}\right)}{\sqrt{2\pi\sigma^2}} \int_{-\infty}^{\infty} \exp\left(\frac{-1}{2\sigma^2} \left[z - \frac{-2\pi i\sigma^2}{\lambda}\right]^2\right) dz \right|^2. \quad (79)$$

Let $z - 2\pi i\sigma^2/\lambda = U \Rightarrow dz = dU$

$$f(\lambda) = \left| \frac{\exp\left(\frac{-2\pi^2\sigma^2}{\lambda^2}\right)}{\sqrt{2\pi\sigma^2}} \int_{-\infty}^{\infty} \exp\left(\frac{-U^2}{2\sigma^2}\right) dU \right|^2. \quad (80)$$

$$\text{Let } U^2/2\sigma^2 = X^2 \quad \Rightarrow \quad dU = \sqrt{2}\sigma dX$$

$$f(\lambda) = \left| \frac{\exp\left(\frac{-2\pi^2\sigma^2}{\lambda^2}\right)}{\sqrt{2\pi\sigma^2}} \int_{-\infty}^{\infty} \sqrt{2}\sigma \exp(-X^2) dX \right|^2, \quad (81)$$

$$f(\lambda) = \left| \exp\left(\frac{-2\pi^2\sigma^2}{\lambda^2}\right) \right|^2 = \exp\left(\frac{-4\pi^2\sigma^2}{\lambda^2}\right). \quad (82)$$

3.8.3 RECTANGULAR DISTRIBUTION

The rectangular distribution is defined as

$$S(z) = \begin{cases} \frac{1}{2l} & |z| < l \\ 0 & \text{otherwise} \end{cases}, \quad (83)$$

substituting in Eq. (69)

$$f(\lambda) = \left| \frac{1}{2l} \int_{-l}^l \exp\left(\frac{2\pi iz}{\lambda}\right) dz \right|^2, \quad (84)$$

$$f(\lambda) = \left| \frac{\lambda}{2\pi l} \left(\frac{\exp\left(\frac{i2\pi l}{\lambda}\right) - \exp\left(\frac{-i2\pi l}{\lambda}\right)}{2i} \right) \right|^2, \quad (85)$$

$$f(\lambda) = \left| \frac{\lambda}{2\pi l} \sin\left(\frac{2\pi l}{\lambda}\right) \right|^2. \quad (86)$$

CHAPTER 4

FAR-INFRARED MEASUREMENTS

The RTI experiment depends on the CSR coming from the fourth dipole at the end of the injector chicane and the radiation is in the far-infrared. In order to complete the experiment, many components such as mirrors, filters, windows, and a detector are chosen to work in far-infrared. The next sections will give a brief summary about these components [35] [36].

4.1 MIRRORS

The normal method to produce far-infrared mirrors is by using vacuum deposition of a low resistivity metal on glass. The reflectivity of metals is given by

$$R = 100 - 3.65\sqrt{\frac{\rho}{\lambda}}, \quad (87)$$

where R is the percentage reflectivity, ρ is the resistivity in $\mu\Omega\text{cm}$, and λ is the wavelength in μm . This means that the reflectivity increases as $\sqrt{\rho/\lambda}$ becomes small.

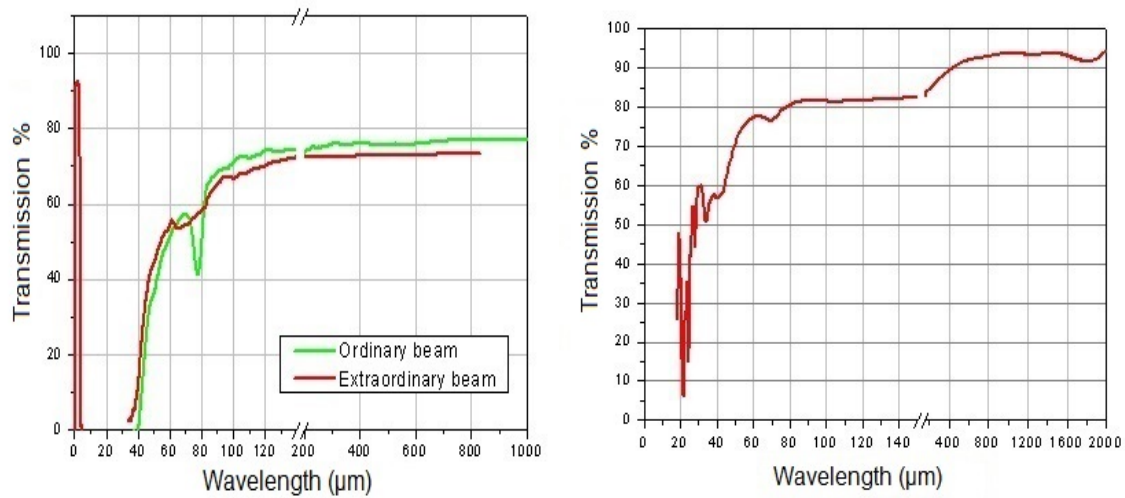
Copper, aluminum, silver, and gold are metals which have very low resistivity. Silver has the highest percentage reflectivity but it tarnishes quickly, while gold has a high reflectivity below $30 \mu\text{m}$ and it can be used for laser mirrors. The resistivity of gold at room temperature is $2.271 \times 10^{-2} \mu\Omega\text{m}$ and the wave length of interest is $100 \mu\text{m}$ for obtaining coherent synchrotron radiation, so the reflectivity of a mirror is about 99.45. Gold coated mirrors are very good to use in the infrared and we chose to use gold coated mirrors in the real time interferometer (RTI) experiment. For long wavelengths, cheap metals with high resistivity can be used because the mirror quality is not critical in this region.

4.2 WINDOWS

The vacuum chamber for the CEBAF accelerator needs a window to allow the radiation to pass through it to the measuring device. The ideal properties of a window are that it should be strong, cheap, and stable for a wide range of temperatures; it should possess high transmission and a low reflection loss. There are many types of windows such as alkali halides, KRS-5, Irtran materials, and silicon; a brief discussion about the most interesting materials follows.

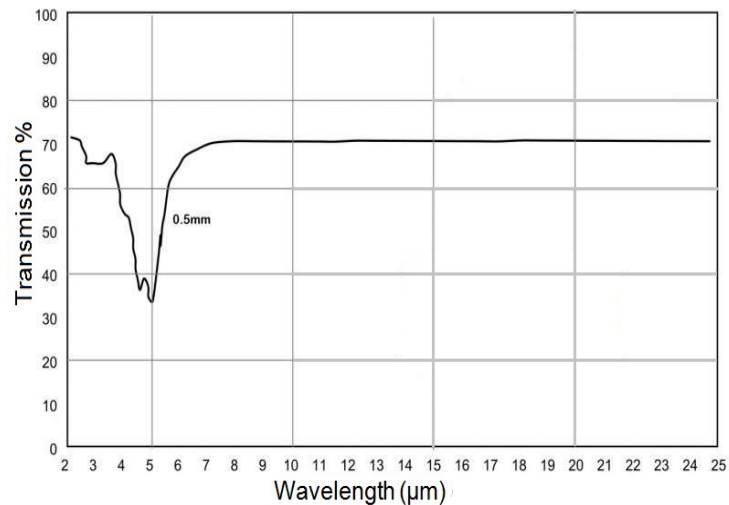
4.2.1 CRYSTALLINE QUARTZ

The refractive index of the crystalline quartz is 2.1 and it has a large thermal expansion coefficient. If it is polished flat, it will give successive maxima and minima in its transmission. It can be used for thin windows down to $45 \mu\text{m}$ and can be used as a filter between 4 and $40 \mu\text{m}$. Crystal quartz is chosen for use in the RTI experiment.



(a) Crystal quartz

(b) TPX



(c) Diamond

FIG. 13: Transmission curve for different materials

4.2.2 TPX

TPX is a hard material and has a resistance to heat deformation. It has a reflective index of 1.43 in the visible and far-infrared. Its transmission is excellent above 200 μm and less than 200 μm it decreases until 50 μm and where it reaches about 65% transmission.

4.2.3 DIAMOND TYPE II

Diamond type II is expensive and has a high refractive index. It is transparent from UV to far infrared and its transmission is about 70%. It is transparent even at high temperatures and has extreme thermal conductivity, hardness, and chemical resistance. Its transmission decreases between 2.5 μm and 6.5 μm , comfortably below THz wavelengths.

4.3 DETECTORS

Far-infrared detectors can be divided into two categories: thermal detectors and photo-conductive detectors. Thermal detectors are based on the absorption of the radiation which heats the detector material. The physical properties of the material will change and the change is measured. Thermal detectors are relatively slow in response because heating is involved. Photo-conductive detectors depend on electron distribution changes upon illumination. When the radiation is incident on the detector, the conductivity changes. Photo-conductive detectors are relatively fast in their response.

The choice of far-infrared detectors depends on several factors:

- 1- The wavelength range at which it responds.
- 2- The voltage responsivity (R_v)

$$R_v = \frac{dV}{dP}, \quad (88)$$

where dV is the output voltage from the detector and dP is the incident power.

- 3- The response time of the detector (τ).
- 4- The minimum detectable power (P_N) or noise equivalent power (n.e.p)

$$P_N = \frac{V_N}{R_v}, \quad (89)$$

where V_N is the root mean square voltage produced by the detector as a result of all noise sources.

- 5- The detectivity (D)

$$D = \frac{1}{P_N}. \quad (90)$$

4.3.1 PYRO-DETECTOR

Pyro-electricity is the ability of a material to generate voltage when it is heated or cooled. A pyro-detector is made when a pyro-electric material is connected with an electrode on each side as shown in Fig. 14. When infra-red radiation falls on the material, heat will be generated and a signal is produced. The signal is amplified and recorded to get a reading proportional to the infra-red radiation intensity.

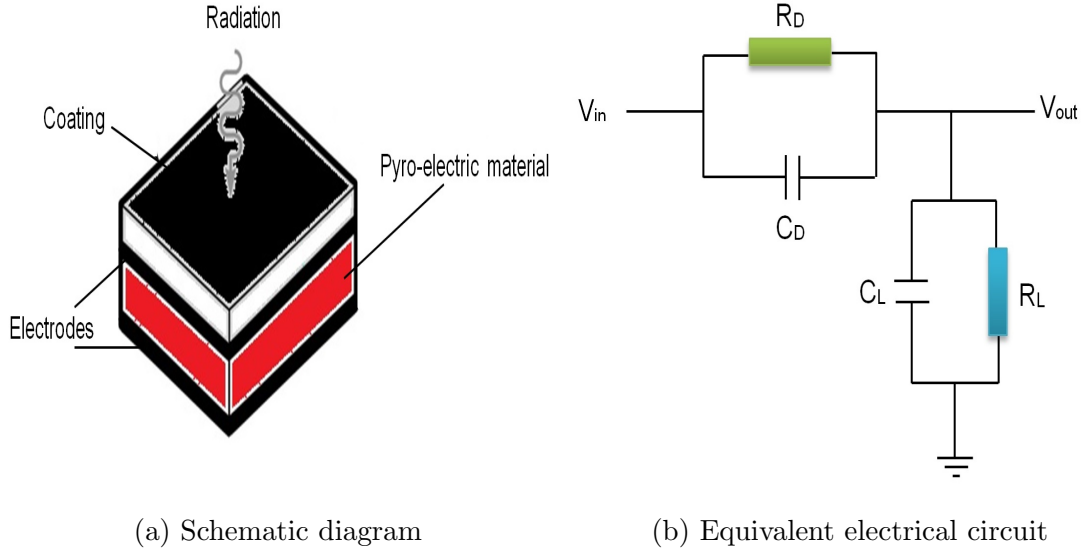


FIG. 14: Schematic diagram for pyrodetector and its equivalent electrical circuit where V_{in} is applied voltage, R_D is the detector resistance, C_D is the detector capacitance, R_L is the load resistance, C_L is the load capacitance, and V_{out} is the output voltage.

The pyro-detector is an AC device because it detects a temperature change, so a chopper should be used with the detector. The detector has a time constant given by

$$\tau_D = \frac{C_P}{C_G}, \quad (91)$$

where C_P is the heat capacity of the pyro material and C_G is the heat conductivity of the material connecting the pyro material and the heat sink. The responsivity of the detector is at a maximum if the chopper frequency is less than the detector time constant (τ_D) and the electrical time constant (τ_E). There are three noise sources associated with the detector: the temperature fluctuation in the detector (V_T), the Johnson noise from the detector's resistance (V_J), and the amplifier noise (V_A). If $V_A^2 \ll V_T^2 + V_J^2$, the signal to noise ratio is constant for

frequencies higher than the frequencies corresponding to the reciprocal of the thermal and electrical time constant. Pyro-detectors are cheap, small, sensitive, have a broad spectral response, and a fast response time, but they have a slightly lower detectivity compared to other detectors. Also their microphonic response requires attention.

4.4 CONCLUSION

In this chapter a brief summary for the best coated mirrors, window materials, and detectors is made to give background about infrared components used in our experiment. In conclusion, it is better to use the crystal quartz than TPX or diamond as a material for the window because it is cheap and does not crack under vacuum. The best mirrors to be used are the gold coated mirrors due to their high reflectivity and they do not tarnish. Also, the pyro-detector is better than the other thermal detectors because it depends on the thermal effect of the radiation regardless of the wave length and does not need to be cooled.

CHAPTER 5

BUNCH LENGTH MEASUREMENT TECHNIQUES

Bunch length measurement is important for determining that the longitudinal dimension of the beam bunches is within the accelerator acceptance. Short bunches lead to robust beam transport which helps in performing the nuclear physics program. There are many techniques used for determining the bunch length. These techniques can be classified into destructive techniques such as a transverse deflecting cavity and the zero phasing technique, or non-destructive techniques such as streak cameras, Synchrotron Light Monitors (SLMs), electro-optical sampling techniques, frequency domain techniques (interferometers and spectrometers), and wall current monitors.

5.1 DESTRUCTIVE TECHNIQUES

5.1.1 TRANSVERSE DEFLECTING CAVITIES

Assuming that an electron bunch with bunch length (σ_z) enters a transverse deflecting RF cavity and the bunch is close to the zero crossing, the amplitude of the deflecting voltage varies across the beam bunch. The voltage effectively maps the longitudinal profile into a transverse angular distribution (vertical beam size) at a distance downstream from the deflecting cavity. The measured beam size on the transverse diagnostic is given by [20]

$$\sigma_y^2 = \beta_s \epsilon_0 + \sigma_z^2 \beta_{cav} \beta_s K^2 (\sin \psi)^2 (\cos \phi)^2, \quad (92)$$

where σ_y is the measured beam size on the screen, β_s is the beta function at the screen position, ϵ_0 is the normalized vertical emittance, $(\beta_s \epsilon_0)$ is the initial vertical beam size, σ_z is the longitudinal bunch length, β_{cav} is the beta function at the deflecting cavity position, ψ is the betatron phase advance, ϕ is the cavity phase, and $K = 2\pi eV/\lambda E$ where e is the electronic charge, V is the deflecting voltage, E is the beam energy, and λ is the RF wavelength. The bunch length is determined from fitting the quadratic relation between the RF deflecting voltage and the square of the measured transverse beam size.

The advantages of this technique are that it is fast, accurate, and if a large deflecting voltage at short RF wavelengths is available, the cavity will give a strong deflection that provides a high resolution. The disadvantage of this technique is that it is destructive.

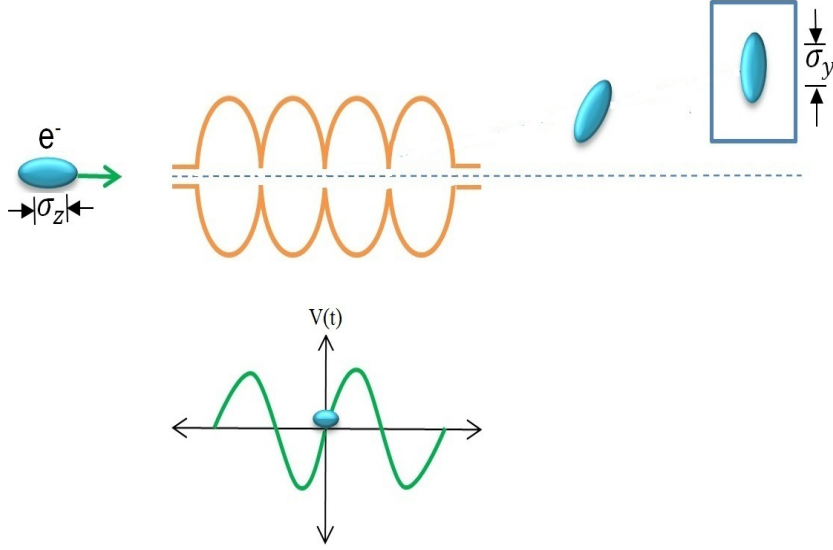


FIG. 15: Transverse deflecting cavity.

5.1.2 SYNCHROTRON LIGHT MONITOR

In this technique, bunch length can be determined by using incoherent synchrotron radiation with the aid of an RF cavity and a profile monitor. This technique must be performed in a high dispersion region using radiation emitted from a bending magnet. The beam size at a horizontally dispersed location is $\sigma_x = \sqrt{\epsilon_x \beta_x + (\eta dP/P)^2}$ where $(\epsilon_x \beta_x)$ is the horizontal beam size, η is the dispersion, and dP/P is the momentum spread. For bunches synchronized with RF and by changing the relative RF phase with respect to the beam bunch, the momentum spread will increase as a function of RF phase change ($\Delta\phi$) and the bunch length (σ_z). Plotting the beam size as a function of RF phase change and doing a parabolic fit, the bunch length can be determined using $\sigma_z = \sqrt{A/|ak|}$ where A is the parabolic fit coefficient, k is the RF wave number, and a is the calibration slope which is given by $-eV_0\eta \sin(\phi)/E_0$, where e is the electronic charge, V_0 is the peak accelerating voltage, η is the dispersion, ϕ is the RF phase, and E_0 is the nominal energy after the linac section. The mathematical background is described in Ref. [37]

The advantage of this technique is that it is fast, inexpensive, and easy to implement while the disadvantage is that it is destructive. The accuracy of the measurement depends

on the dispersion and the monitor resolution which depends on the optical setup and the digital camera.

5.2 NON-DESTRUCTIVE TECHNIQUES

5.2.1 STREAK CAMERA

Streak cameras convert the temporal profile of the bunch into a spatial profile by using the radiation which comes from the electron beam (diffraction radiation, transition radiation, synchrotron radiation, etc.). The emitted light passes through a slit followed by a photocathode where the light is converted into electrons proportional to the light intensity. The electrons pass through an accelerating mesh to increase their kinetic energy, and then they go into a sweeping circuit. The sweeping circuit consists of positive and negative electrodes.

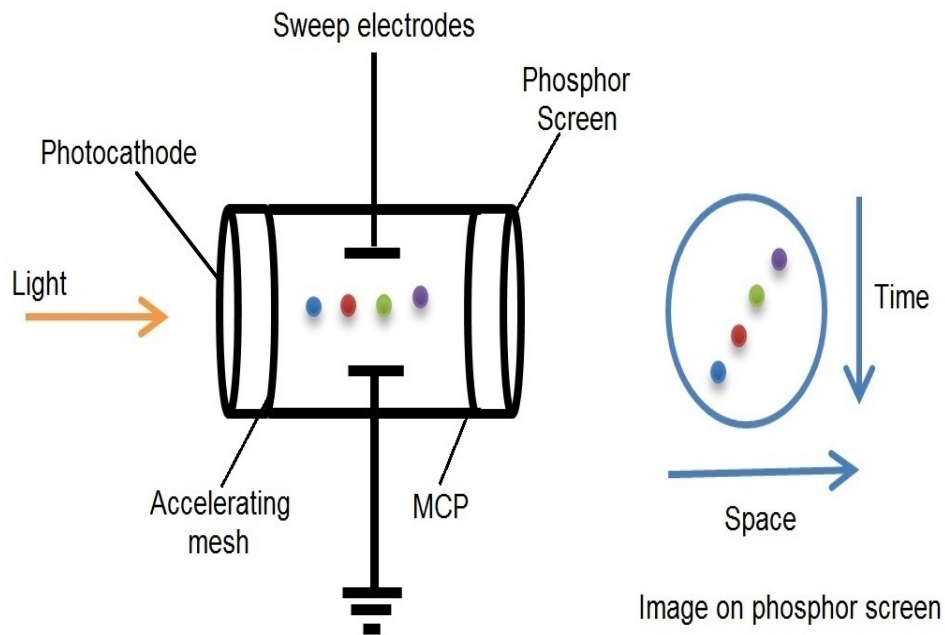


FIG. 16: Streak camera

Electrons arriving at different times are deflected by different angles before they go through a micro-channel plate (MCP). The number of electrons is amplified as they pass through the MCP and then hit a phosphor screen. The brightness of the phosphor image is proportional to the incident light intensity and the images appear on the screen from top to bottom where the electrons entering first go to the top as shown in Fig. 16. The vertical axis represents time and the horizontal axis acts as space (horizontal distance) for the incident

light. The incident light intensity can be determined from the phosphor image while the arrival time and position can be determined from the location of the phosphor image.

The advantage of streak camera is that it can be used for a wide range of radiation frequencies from near infrared to X-rays while its disadvantage is that it can not resolve less than 200 fs due to the limitations in the sweeping electric field.

5.2.2 INTERFEROMETERS

This technique depends on frequency analysis of the radiation coming from the beam. The radiation path is split into two paths and each path will have successive reflections. The radiation in the two paths recombines to form an interference pattern which is detected by a detector. Golay cells or pyro-electric detectors have been used. The resulting interference pattern can be converted from frequency domain into the time domain by using Fourier transformation and the bunch length can be determined. There are many types of interferometers. A common type is the Michelson interferometer as shown in Fig. 17. The advantage of this method is that it is more inexpensive than other techniques but its disadvantage is the missing phase information, which complicates interpreting results.

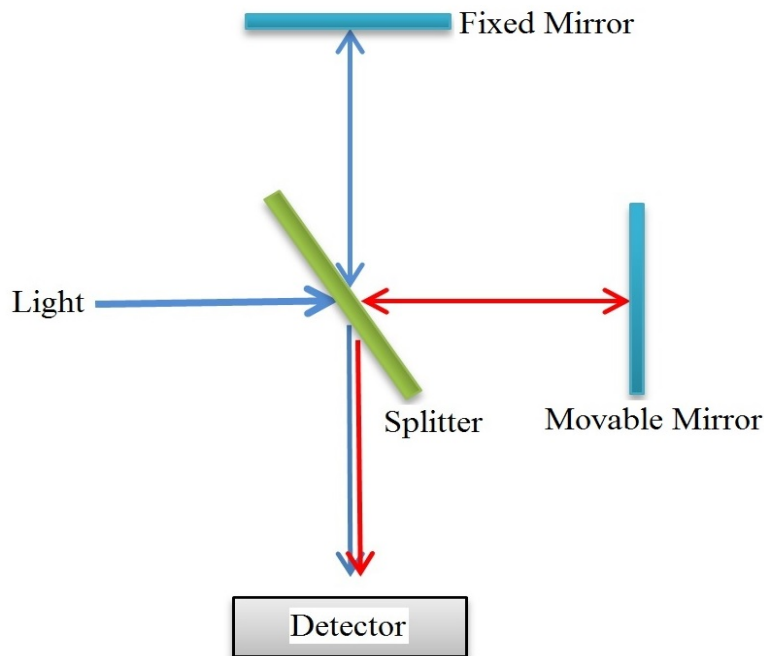


FIG. 17: Michelson interferometer

5.2.3 WALL CURRENT MONITORS

Accelerated electrons in a conducting tube will produce an image charge on the inner tube wall which produces a current equal and opposite to the beam current. If the wall current passes across a resistor (R), the resulting voltage pulse can be measured via an oscilloscope. To measure the beam current, the beam pipe is cut and a resistive ceramic gap is used as shown in Fig. 18. The ceramic gap is used to interrupt beam pipe conduction and usually Ferrite cores are used to allow the current to pass through the resistance instead of passing in other conducting parts. The measurement is valid only if the following relation is fulfilled [38]

$$\sigma_t \gg \frac{r}{\gamma\sqrt{2}}, \quad (93)$$

where σ_t is the *rms* bunch length, r is the tube radius, and γ is the relativistic Lorentz factor. When the particles are relativistic, the electric field will compress by a factor $1/\gamma$ within a small angle in the transverse direction. When Eq. (93) is satisfied, the electric field duration on the gap is less than the bunch length which is ideal for the measurements. The monitor will measure the bunch length instead of the $1/\gamma$ width of the electric field distribution.

The ceramic gap acts as a capacitor (C_{gap}) and it shorts the circuit at frequencies above F_{hf} . The low frequency cut off of the circuit (F_{lf}) and high frequency cut off (F_{hf}) are given by

$$F_{hf} = \frac{1}{2\pi RC_{gap}}, \quad (94)$$

$$F_{lf} = \frac{R}{2\pi L}. \quad (95)$$

The wall current monitor is usually used to determine the bunch length for proton accelerators and it is rarely used in the determination of electron bunch length because the electron bunch length is usually much too small. Wall current monitors are usually limited in bandwidth to around several GHz.

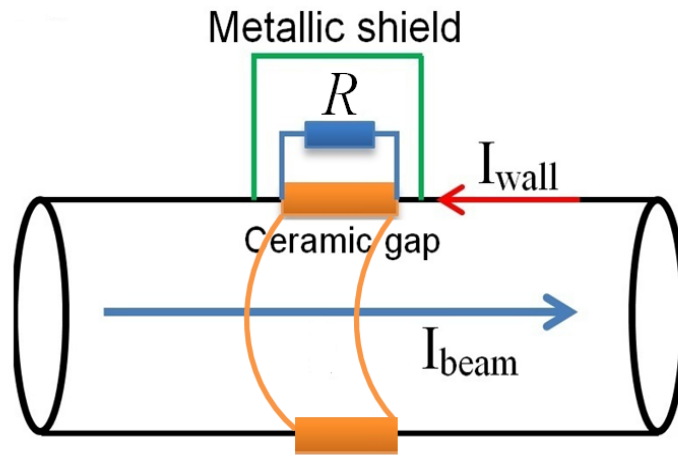


FIG. 18: Wall current monitor

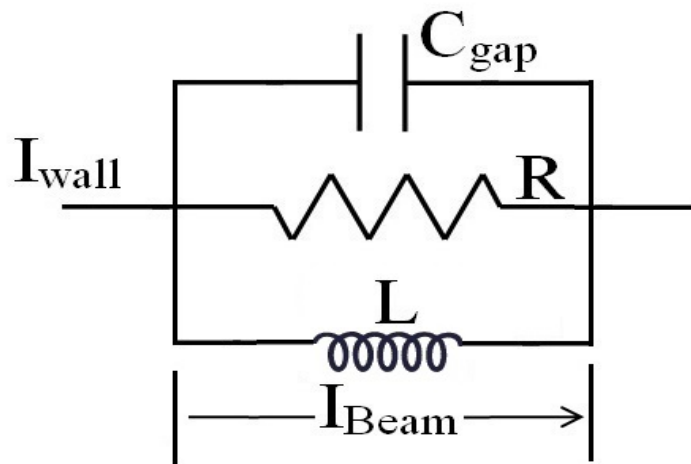


FIG. 19: Equivalent circuit for wall current monitor

CHAPTER 6

CEBAF BUNCH LENGTH MEASUREMENTS

6.1 BUNCH LENGTH IN THE INJECTOR

6.1.1 INJECTOR OVERVIEW

The CEBAF accelerator uses up to four lasers striking a photo cathode to form its beam. The laser pulses are produced at a sub-harmonic of the fundamental accelerator operating frequency of 1497 MHz, usually the third or sixth sub-harmonic. The laser system consists of an inexpensive seed laser (1560 nm), an ErYb doped fiber amplifier, and a Periodically Poled Lithium Niobate (PPLN) frequency doubler. A DC current and RF sine wave are used to bias the seed laser as in Fig. 20. The DC and RF should be balanced in order to minimize extraneous laser light incident on the photo cathode. For example if the DC bias is too high, laser light will be continuously emitted at low level and if the RF is high, this will produce an after pulse. If both of them are low, the seed will not produce the desired amplitude. The seed laser produces about 1 mW average power at 499 MHz. The fiber amplifier amplifies the 1 mW to 5 Watts, then the amplified light is taken into a Second Harmonic Generator (SHG) see Fig. 21.

In the SHG, the light is collimated by lens (L1) before it goes to the half wave plate (W1). The half wave plate will change the linear polarization to circular polarization to match the polarization axis of the PPLN crystal. The PPLN crystal must be aligned properly and be at the correct temperature to match the phase of the laser. Some of the 1560 nm light will be converted to 780 nm light. The two wave lengths are collimated through lens (L3) before they hit a dichroic mirror (M3) which is coated to pass the 1560 nm and reflect the 780 nm. The 780 nm is reflected by mirror (M4) through a laser table before it hits the photo cathode to produce the electron beam [39].

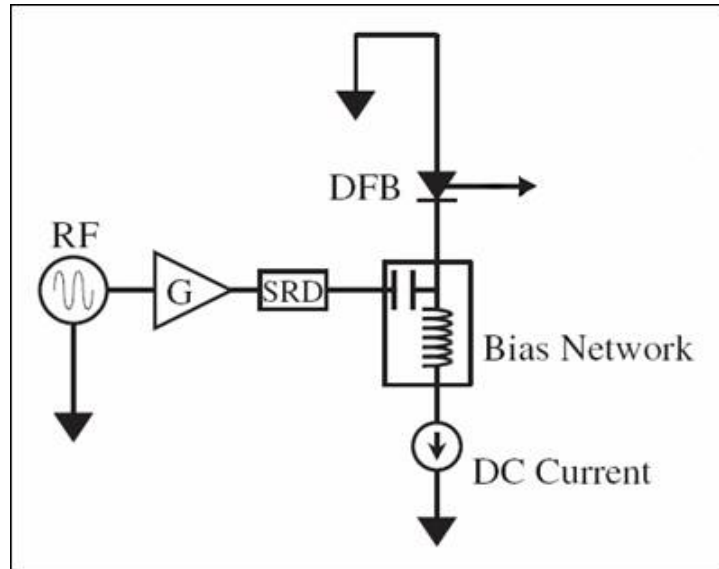


FIG. 20: Gain switch representation

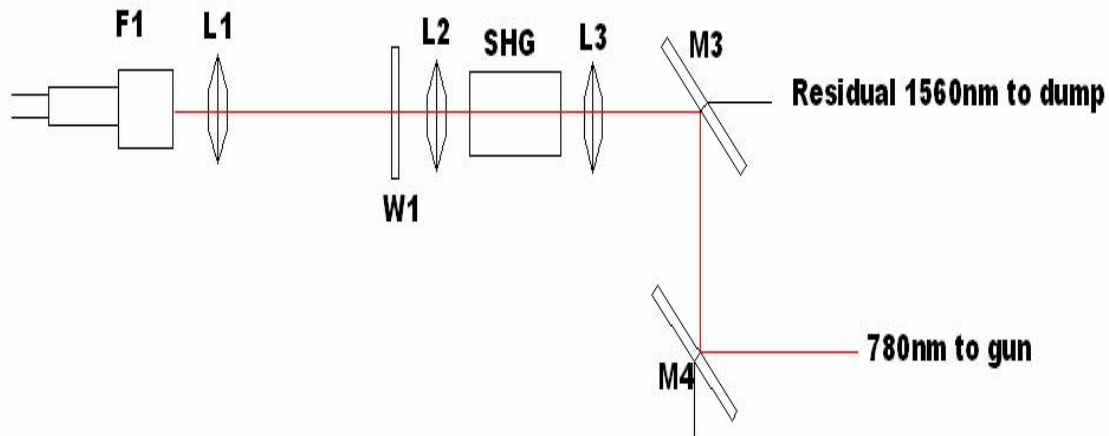


FIG. 21: SHG representation

The photo cathode is prepared for photo emission in a preparation chamber. The preparation chamber maintains four Gallium arsenide (GaAs) photo cathodes that can be used at any time in case the cathode in use needs to be replaced. It takes about 12 hours to do a cathode replacement. Nitrogen trifluoride (NF_3) and cesium (Cs) are used to activate the photo cathode by lowering the work function of the material. After activation, the photo cathode is placed in the center of a high voltage chamber.

A voltage of -130 kV is applied to the cathode to extract the electrons liberated when the laser light impinges on the cathode. The laser pulse structure has three modes: viewer-safe mode, tune mode, and CW mode. Any mode has a macropulse consisting of a series of microbunches generated by the laser. The beam bunch length is defined by $\tau_\mu v_b$ where τ_μ is shown in Fig. 22 and v_b is the beam velocity. In general, the beams delivered to the different halls have different microbunches with different bunch lengths. Each microbunch is separated from the next microbunch by an integral number of the fundamental RF period as shown in Fig. 22. The macropulse length in viewer mode is 10 μs at 60 Hz repetition rate. This beam mode is used whenever viewers are in the accelerator beam path. Tune mode beam has a macropulse length of 250 μs , again at 60 Hz, and is used to thread beam through the accelerator. It has the advantage of being measured by the Beam Position Monitors (BPM). Tune mode beam does not have enough power to damage equipment or drill a hole in the beam line vacuum chambers. The CW mode beam is on continuously and is used for physics data production as shown in Fig. 23.

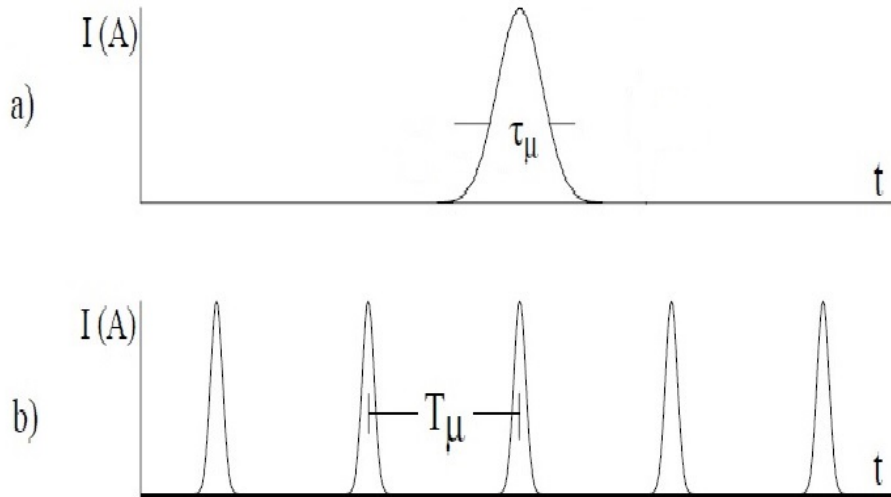


FIG. 22: Definition of time structure [32]. a) Microbunch with time duration τ_μ . b) Microbunches separated by a multiple of the RF period. T_μ is either 3 or 6 times 666.8 psec, the fundamental accelerating period.

After the electron beam leaves the gun, it goes through beam magnetic elements (correctors, solenoids and viewers) until it reach the first Wien filter. The vertical Wien filter is used to rotate the spin of the electrons vertically by $+\pi/2$ with respect to the beam path. After the beam passes the Wein filter, it will traverse two spin flipper solenoids. The solenoids can rotate the spin polarization transversely to the left or to the right while keeping the beam

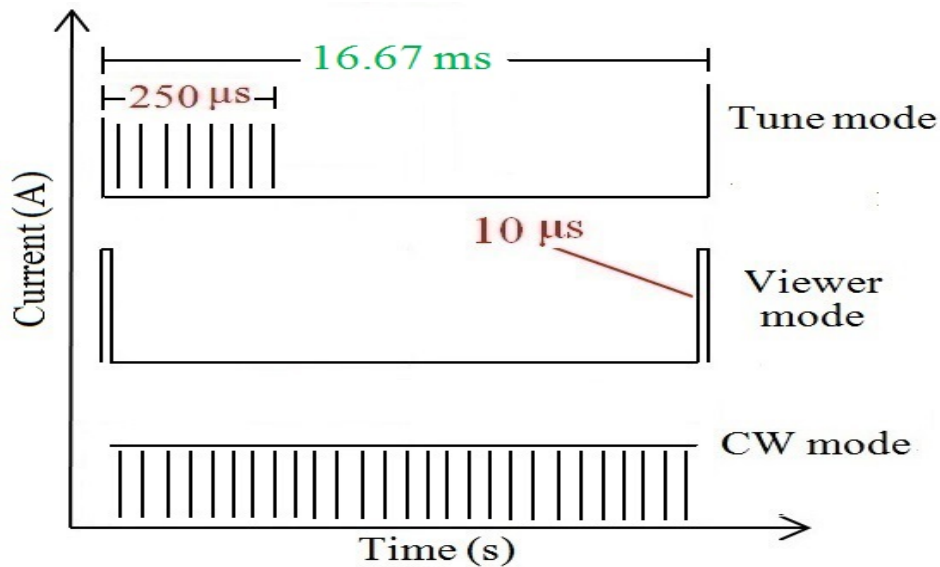


FIG. 23: Current for different beam modes. The series of spikes represents the micropulsed current, not to scale

envelope and beam focusing constant (the solenoids orient the spin into the vertical plane with the spin vector perpendicular to the beam direction). After spin orientation, the beam traverses the prebuncher which is a cavity with a longitudinal electric field that is used to compress the beam longitudinally. After the prebuncher, the beam goes through a horizontal Wien magnet which deflects the spin to an angle with respect to the horizontal plane. Two apertures A1 and A2 are placed before and after the horizontal Wien filter. They are used to control the emittance of the beam by trimming the transverse beam halo. Downstream of A2, the beam meets the chopper system.

The chopper system consists of two square box cavities (chopper 1 and chopper 2) with two solenoids and a chopping chamber between them. The two cavities are operated in two degenerate orthogonal modes TM_{120} and TM_{210} with circular polarization. When the two modes are excited in quadrature phase and equal amplitude, the first cavity deflects the incoming beam radially outward and sweeps the beam into a circle at the chopping chamber. The first solenoid focuses the beam parallel to the beam line. After passing the chopping chamber, the second solenoid deflects the beam to the center of the second cavity (chopper 2). The kicks from the two choppers must cancel in order to make the over all deflection from the chopping system zero. In normal operation of CEBAF, the chopping chamber is used to define the beam intensity for each hall. The chamber consists of the master slit (held at 10 o'clock), central plug (held at 2 o'clock), and Hall A, B, C slit apertures (held at 8,

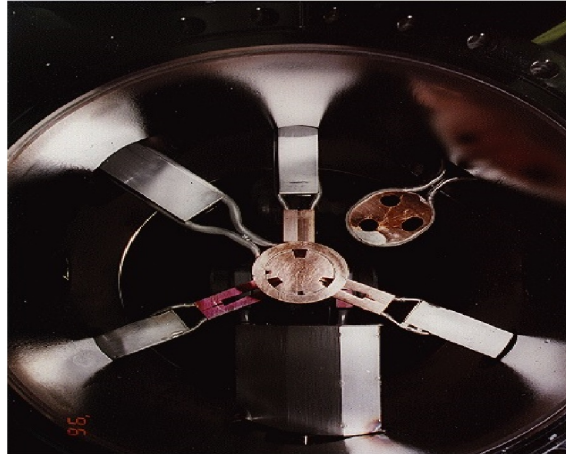


FIG. 24: chopping chamber

12 and 4 o'clock respectively) as shown in Fig. 24. The Master slit has a small aperture in the center of the disk used for beam centering measurements. Each chopping aperture (A, B, and C) defines a phase acceptance of 60° at 1497 MHz and can be fully inserted, fully retracted, or partially inserted. A slit and C slit have smaller apertures which are used for bunch length testing. The beam does not pass through them during normal operation. The central plug is inserted when the chopper RF is turned off.

After the chopping system, the electron beam goes through the buncher. The buncher is a cavity which operates in a TM_{010} mode at 1497 MHz and is used to compress the electron beam bunch, via kinematic compression (see Section 3.7) before it passes through the capture section. The capture section increases the beam energy from 130 keV to 500 keV. Then the beam enters the 1/4 cryomodule which consists of 2 five-cell superconducting cavities. After the 1/4 cryomodule, the beam energy becomes 6.2 MeV. The beam goes through different beam optics until it meets the 0L03 and 0L04 cryomodules which increase the beam energy to 123 MeV. Finally, the beam bunch is compressed through the injector chicane, via magnetic compression (see Section 3.7), before it is injected into the north linac.

6.1.2 CHOPPER SLIT TECHNIQUE

The slit-chopper scan is an invasive technique which is used to measure the bunch length of the beam at the chopper as shown in Fig. 25. The measurements are done by setting the prebuncher gradient to zero. The Hall A laser configuration is utilized and the current adjusted by changing the attenuator. The Hall B slit, Hall C slit, and master slit apertures are closed during the measurements. A 130 keV electron beam is sent to the chopping chamber and passes through a notch (narrow slit) in the Hall A slit which is 18 ± 1 ps wide. By changing the laser phase in one degree steps (1.8 ps), the bunch charge transmitted through the notch is measured as a function of phase with a Faraday cup.

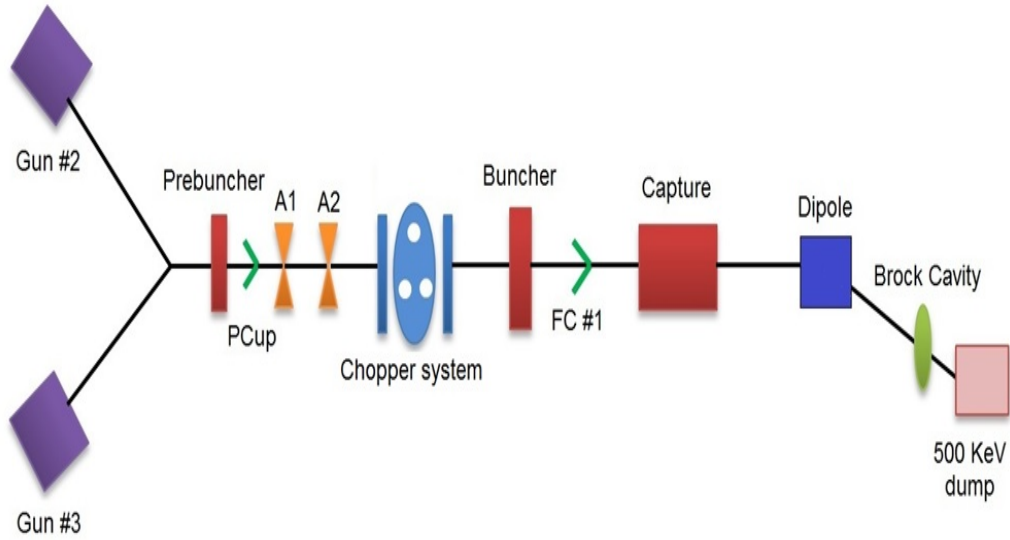


FIG. 25: Schematic diagram for injector line from the gun to the 1D line

The previous steps are done with different attenuator settings to change the laser power which changes the total charge in the beam bunch. The results show that the bunch length increases as the charge increases and the bunch length distribution becomes non-Gaussian as shown in Fig. 26, due to space charge effects which become significant for large bunch charge. The actual bunch length reported is calculated by deconvolving the notch size from the raw data. This is done by using the following equation

$$\sigma_{corrected}^2 = \sigma_{meas.}^2 - (\text{notch size})^2, \quad (96)$$

where $\sigma_{corrected}^2$ is the FWHM for the actual bunch length and $\sigma_{meas.}^2$ is the FWHM for the measured bunch length.

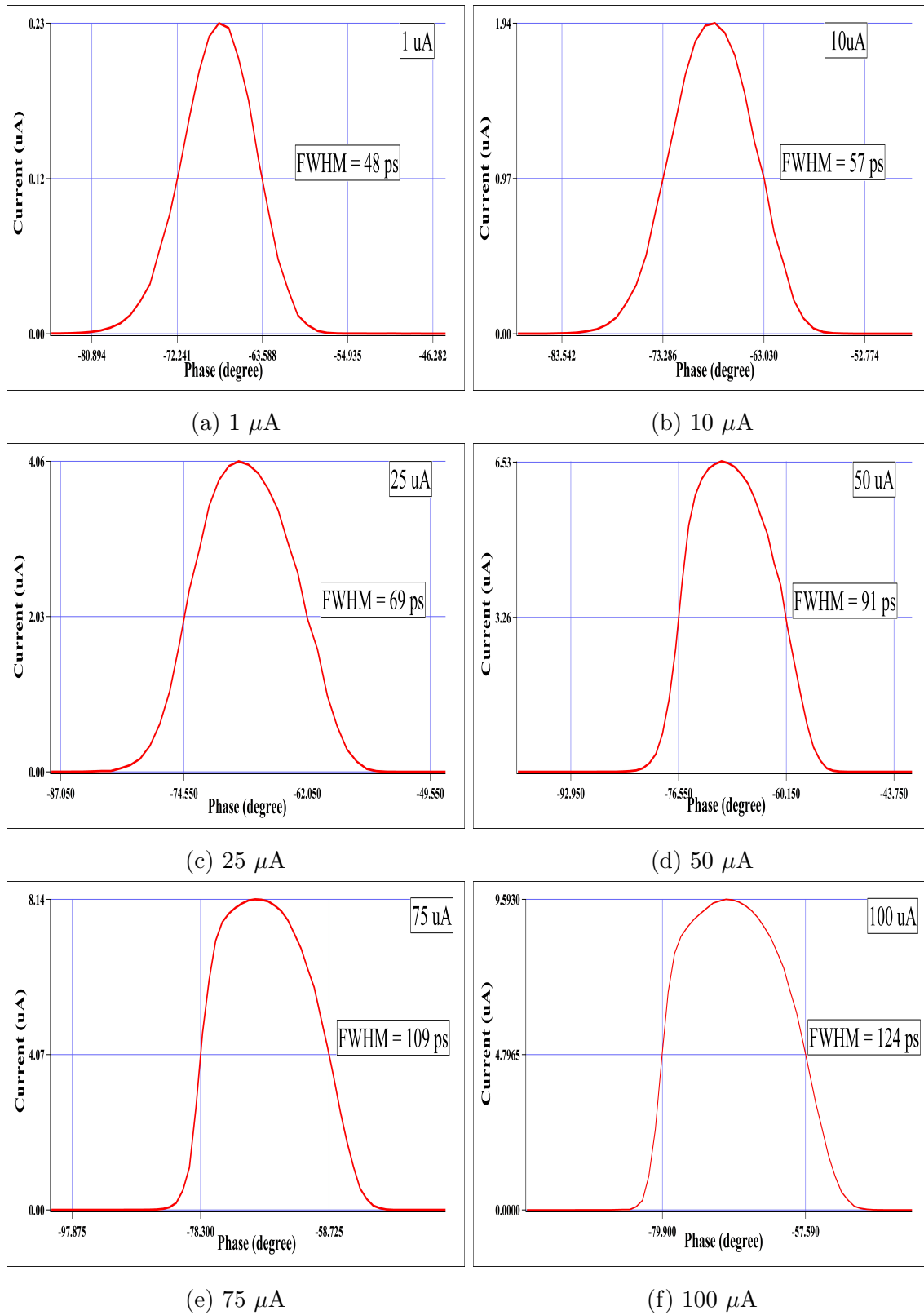


FIG. 26: The beam current transmitted through the chopper-slit as a function of the laser phase is shown for six different beam currents. These measurements were made using the A-laser with a 499 MHz repetition rate.

The bunch length results for different currents are shown in Table 1. The uncertainty of the corrected FWHM is calculated by quantifying the notch size uncertainty.

TABLE 1: Bunch length results for different currents using the chopper slit technique

Current (μA)	FWHM_{measured} (ps)	FWHM_{corrected}(ps)	Distribution
1	48	44.5 ± 0.4	Gaussian
10	57	54.1 ± 0.4	Gaussian
25	69	66.6 ± 0.3	non Gaussian
50	91	89.2 ± 0.2	non Gaussian
75	109	107.5 ± 0.1	non Gaussian
100	124	122.7 ± 0.1	non Gaussian

6.1.3 BROCK CAVITY

A harmonic resonant cavity (also known as the Brock cavity) is used in the injector 1D line to determine the bunch length. The Brock cavity is non-invasive as it uses RF signals in the cavity generated by the beam bunches in the cavity. When the electron beam goes through the bore of the cavity the cavity is excited and resonates with relative amplitude and phase at Fourier harmonics of the beam current. The superposition of those modes creates a voltage versus time signal. The current in the periodically bunched beam can be described as a Fourier series expansion in the form

$$I(t) = a_0 + a_1 \cos(\omega_0 t + \theta_1) + a_2 \cos(2\omega_0 t + \theta_2) + a_3 \cos(3\omega_0 t + \theta_3) + \dots, \quad (97)$$

where $I(t)$ is the electron beam current, a_0 is the DC current, and ω_0 is the bunch repetition frequency. Both a and θ terms have an effect on the shape and bunch length measured. The cavity resonates in TM modes. In order to exclude TE mode excitation, the cavity is designed so that the length of the cavity along the beam direction of motion (l) is very small. Because any TE mode oscillates at frequencies greater than or equal to $c/2l$, where c is the velocity of light, they are minimally excited below many tens of GHz.

The cavity is designed to resonate with the beam current in the TM_{0n0} modes which means that it will have only a radial wall current. To ensure only these modes are excited, the cavity walls are cut with a radial slits to remove the unwanted azimuthal modes. The TM_{0n0} modes in the cavity are designed so they are nearly harmonics of the bunch repetition frequency (ω_0). This is accomplished by properly adjusting the shape of the cavity by using a computer design simulation program called superfish [40].

The cavity consists of two halves. Each half is manufactured from 12.5 mm thick aluminum sheet. The sheet is cut into disks with outer diameter about 20 cm. In the center of these disks a beam line aperture is drilled with diameter 8 mm. Forty eight slots are cut from the back side of each half and the interior of the disk is removed. The cavity is formed by bolting the two halves with an intervening wire seal. Three aluminum supporting tabs are used to bolt the cavity inside a double sided knife edge flange with diameter 33.65 cm (13.25 inch). A copper taper is attached between the two halves at the edge of the beam aperture forming a magnetic field coupler, and attached to a knife edge flange by a feed-through. Finally, the cavity and the knife edge flange are inserted between a reducing flange [41] as shown in Fig. 27.

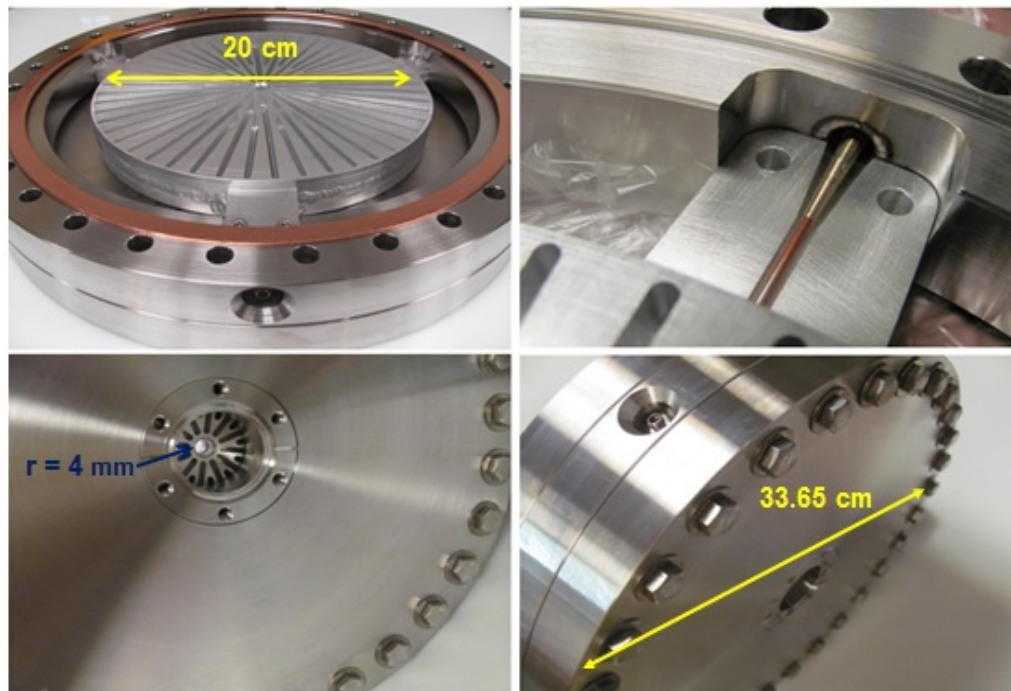


FIG. 27: Brock cavity

For calibration, the Brock cavity was installed near the Faraday cup beam dump in the 1D line of the injector line as shown in Fig. 28. The cavity signal is taken by a fast cable (40 GHz) to a fast sampling oscilloscope. The oscilloscope screen and inputs are remotely controlled via an epics screen. A camera is set observing the oscilloscope screen to record the signal and compare it with the epics screen as shown in Fig. 29. The measured signal has distortion due to imperfections in cavity manufacturing. If the cavity had no imperfections, the signal

output would reflect the beam current. Imperfection in the cavity which cause misalignment between the resonant mode (measured) and the beam Fourier terms (ideal) cause uneven excitation of the different modes. This phase and amplitude error is a systematic error which can be corrected by obtaining a transfer function.

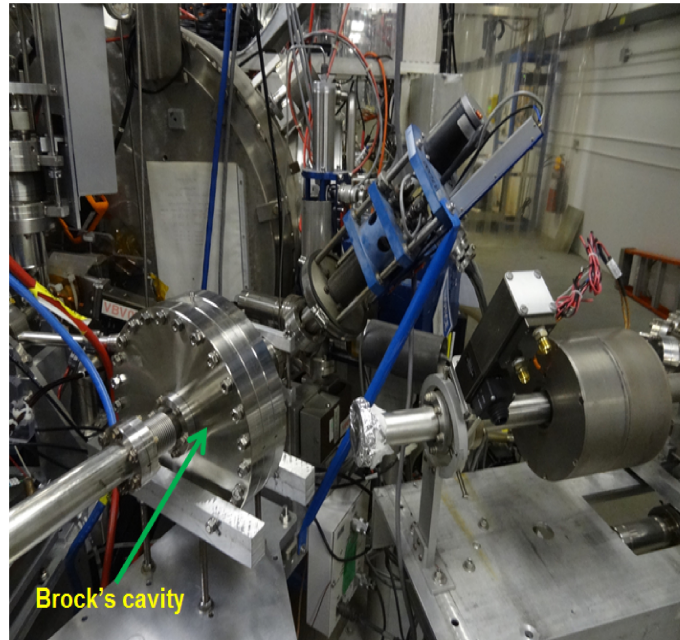


FIG. 28: Brock cavity in 1D line

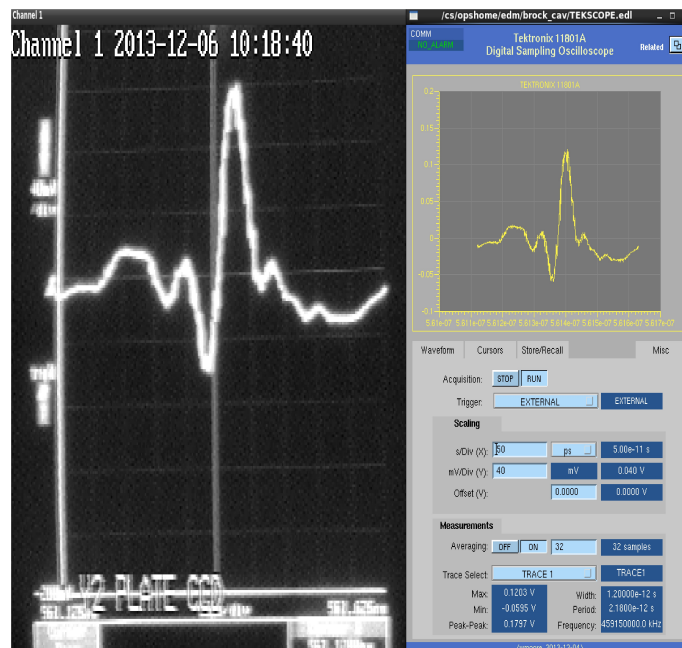


FIG. 29: Oscilloscope signal from camera and epics

Assume that the beam Fourier series is $B(f)$ and the detected signal is $D(f)$. The beam Fourier series can be obtained by multiplying the detected signal by the transfer function $T(f)$

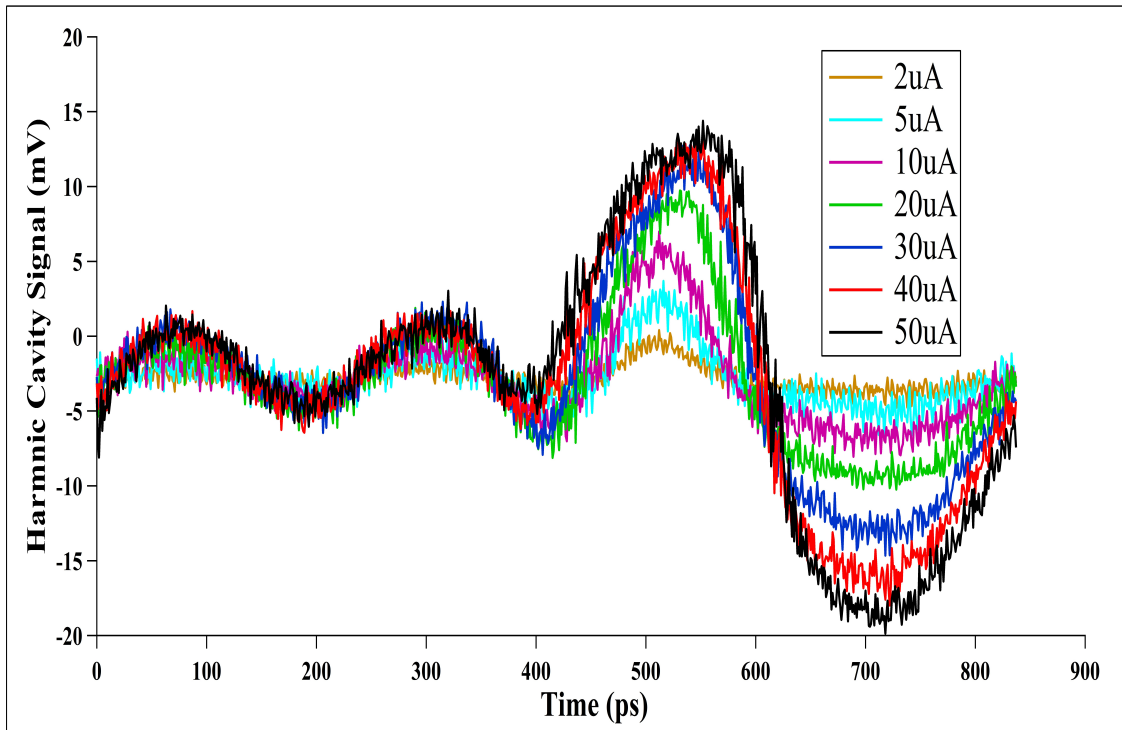
$$B(f) = D(f) \times T(f). \quad (98)$$

Since the transfer function is not known, an assumption is made to obtain it. In the calibration run the beam current is assumed to be Gaussian (verified a posterior) and the beam conditions were $25 \mu\text{A}$ and 500 keV . A Gaussian fitting is done to the detector output. Then the Fourier transform is done to the original voltage and the fitted Gaussian.

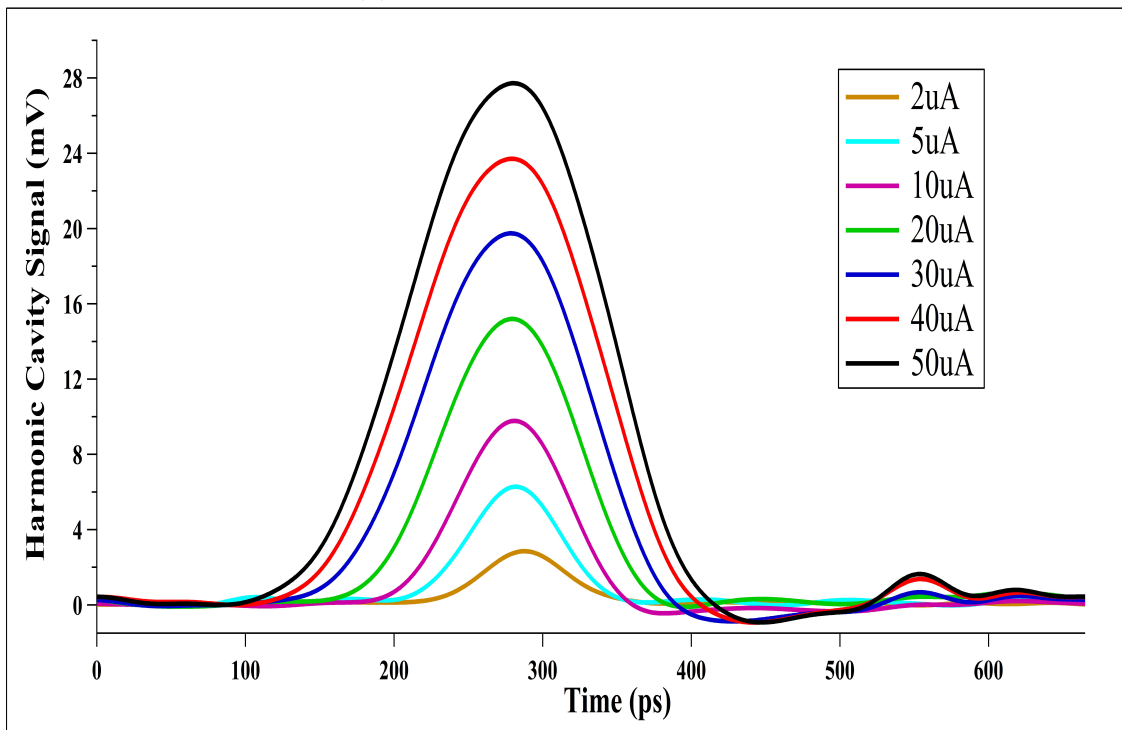
The transfer function is obtained by dividing the FFT of the fitted Gaussian by the FFT of the original voltage. Once it is obtained, the transfer function is used to correct and derive the voltage for all the measurements at 130 keV . The corrected voltage is obtained by multiplying the FFT of the measured voltage by the transfer function, then an inverse Fourier transform (IFFT) of the output of the multiplication is plotted. The corrected voltage for different beam currents are shown in Fig. 30 and the FWHM for the bunch length is calculated. The bunch length results are shown in Table 2. Comparing the results with the chopper slit method in Table 1, the bunch length as measured by Brock cavity is higher because of the effect of the space charge. The bunch moves a distance downstream of the chopping chamber before it reaches the Brock cavity.

TABLE 2: Bunch length results for different currents using the Brock cavity in the 1D line

Current (μA)	FWHM_{measured} (ps)
2	64.6 ± 0.2
5	69.2 ± 0.2
10	81.7 ± 0.3
20	99.1 ± 0.3
30	118.3 ± 0.5
40	130.9 ± 0.6
50	138.9 ± 0.6



(a) Before using transfer function



(b) After using transfer function

FIG. 30: Measured voltage before and after using transfer function correction for the Brock cavity at the 1D line.

Brock cavity after A2 aperture

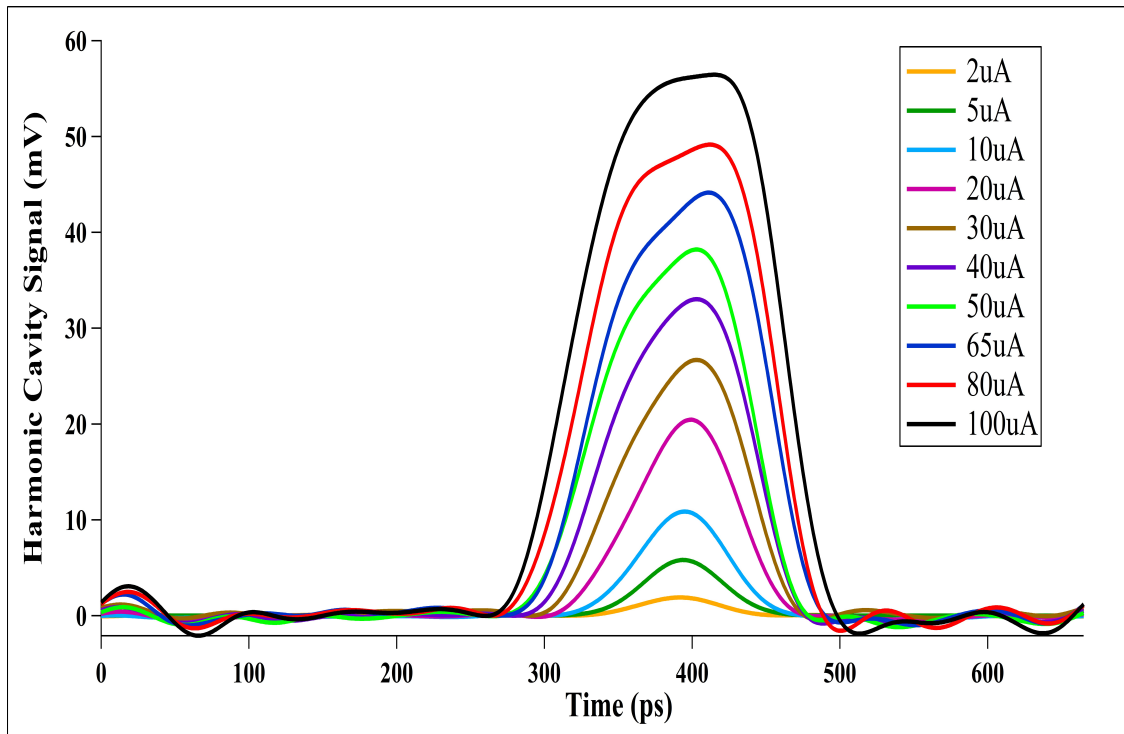
After the initial successful testing and measurements using the Brock cavity in the 1D line it was removed from the 1D line and installed on the main injector beam line after the A2 aperture. A new set of measurements were done using both the harmonic cavity and the slit scan technique using the B-laser at 499 MHz and the A-laser at 249.5 MHz. The FWHM bunch length results from the slit-scan technique are calculated as in the previous section. The transfer function correction method is used for the Brock cavity and the bunch length is calculated at FWHM. The corrected voltages are plotted for 499 MHz and 249.5 MHz as shown in Fig. 31 and Fig. 32. The bunch length at FWHM for both techniques are shown in Table 3 and Table 4.

TABLE 3: Bunch length results for Brock cavity at A2 and slit scan technique using the 249.5 MHz laser

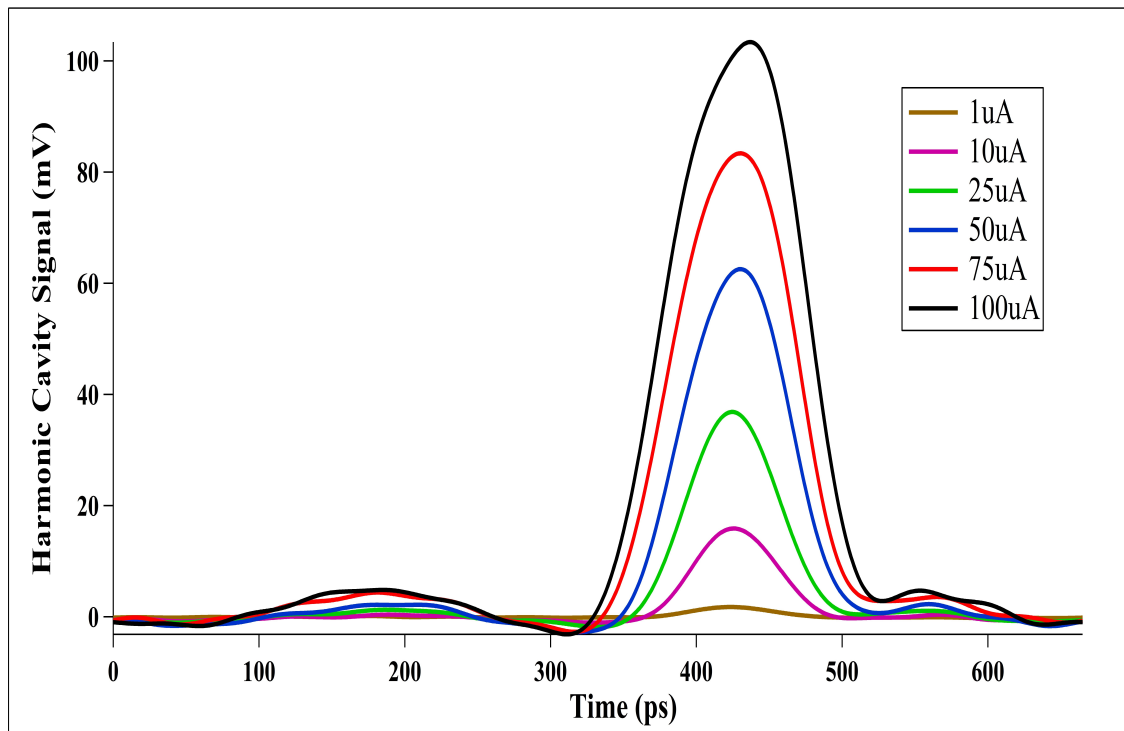
	Brock cavity	Slit-scan
Current (μA)	FWHM_{measured} (ps)	FWHM_{corrected} (ps)
1		59.4 ± 0.3
2	61.1 ± 0.1	63.7 ± 0.3
5	62 ± 0.1	69.5 ± 0.3
10	68.4 ± 0.1	80.4 ± 0.2
20	79.2 ± 0.1	100.3 ± 0.2
30	95.7 ± 0.1	116.6 ± 0.2
40	105.6 ± 0.1	130.7 ± 0.2
50	113 ± 0.1	143.6 ± 0.2
65	123.2 ± 0.1	154.8 ± 0.1
80	132 ± 0.1	167.1 ± 0.1
100	144.9 ± 0.1	182.2 ± 0.1

TABLE 4: Bunch length results for Brock cavity at A2 and slit scan technique using the 499 MHz laser

	Brock cavity	Slit-scan
Current (μA)	FWHM_{measured} (ps)	FWHM_{corrected} (ps)
1	63.2 ± 0.1	45.6 ± 0.4
10	65.2 ± 0.1	56.2 ± 0.3
25	70.2 ± 0.1	72.6 ± 0.2
50	83 ± 0.1	95.2 ± 0.2
75	95.4 ± 0.1	114.9 ± 0.2
100	104 ± 0.1	131.3 ± 0.1

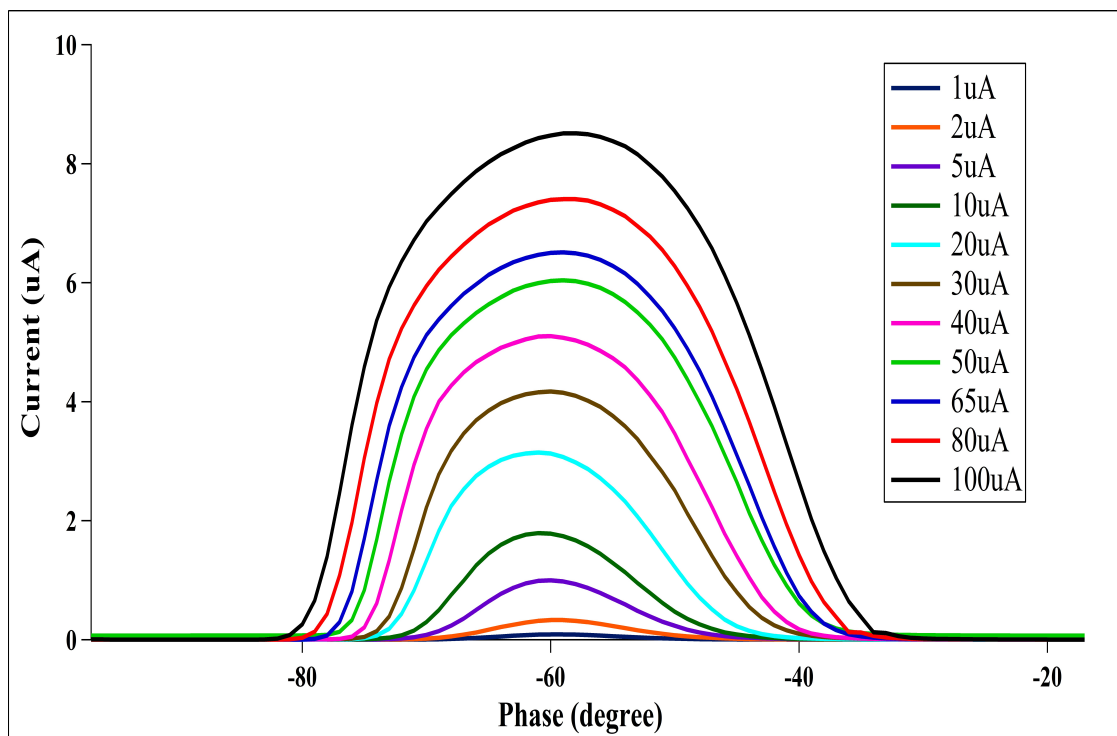


(a) Brock cavity for A-laser at 249.5 MHz

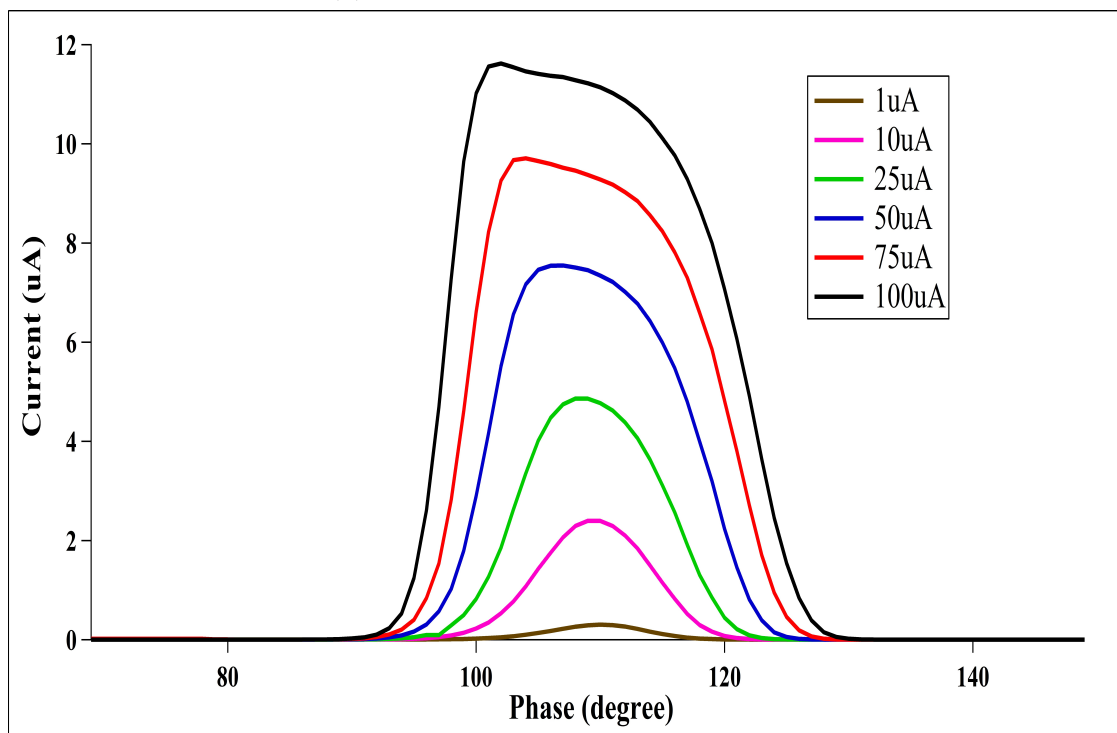


(b) Brock cavity for B-laser at 499 MHz

FIG. 31: Measured voltage for A-laser and B-laser for Brock cavity at the A2 location.



(a) Slit scan for A-laser at 249.5 MHz



(b) Slit scan for B-laser at 499 MHz

FIG. 32: Slit scan for A-laser and B-laser.

6.1.4 PARTICLE TRACKING SIMULATION

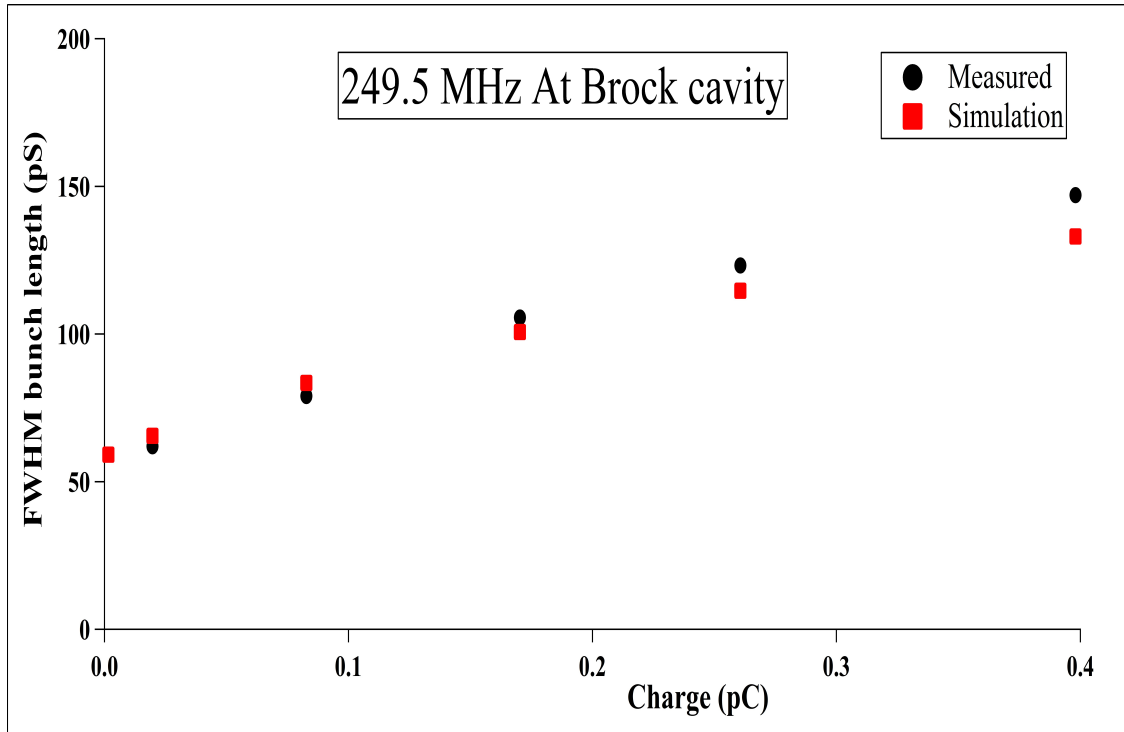
As mentioned in the previous sections, the bunch length is measured by two techniques separated longitudinally. The Brock cavity (first technique) is upstream of the chopper (second technique) by about 2.1 meters and due to the space charge effect, the bunch length is not the same (the bunch will grow as it travels). In order to compare the two techniques, a particle tracking simulation (ASTRA) is used to estimate the bunch length at the two locations¹. ASTRA tracks the particles including the effect of space charge forces. The particle distribution used in the simulation is a simple 10000 particles Gaussian distribution. The bunch length values for both techniques and the simulation results for repetition rates 249.5 MHz and 499 MHz are shown in Fig. 33 and Fig. 34

Comparing the results of the two techniques and the simulations shows good agreement. The measurements made by the Brock cavity with the 499 MHz laser overestimate the bunch length at low current (charge) due to the limited band width of Brock cavity while the measurements made with the 249.5 MHz laser overestimate the bunch length at higher currents by about 10%. This result indicates that the transfer function needs more refinement. Another point to mention: at higher current ASTRA simulations did not predict asymmetric bunch profile as was indicated by both techniques.

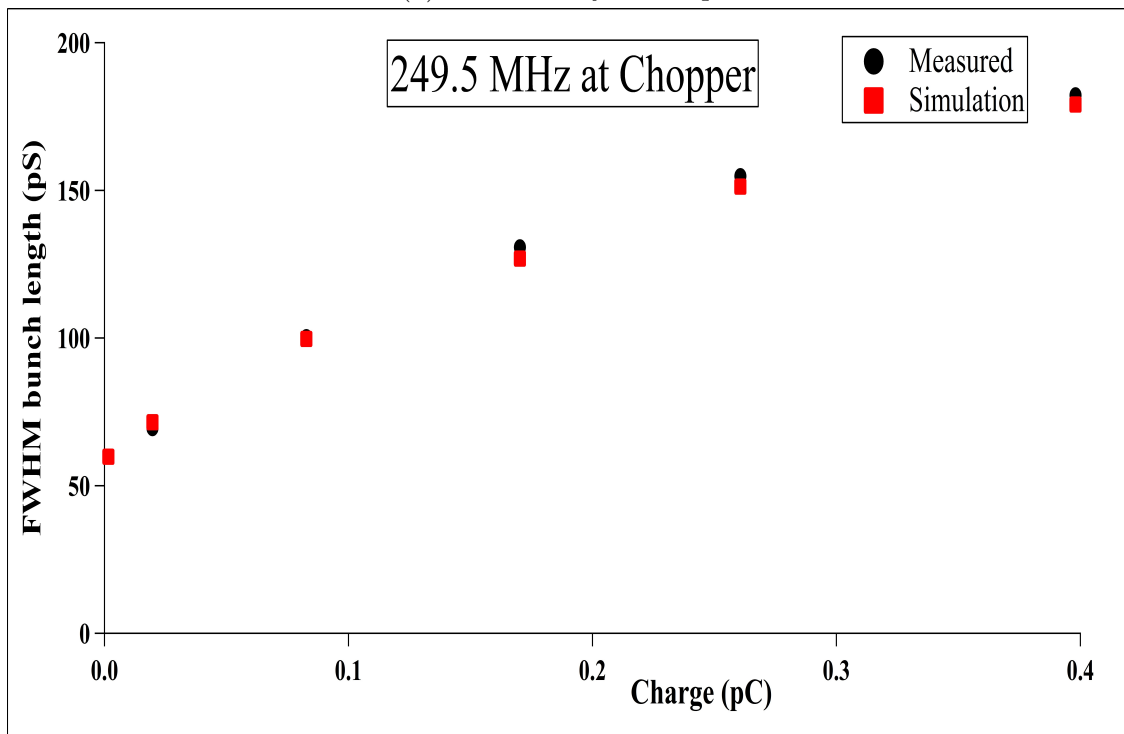
6.1.5 BROCK CAVITY AS A PHASE DETECTOR

CEBAF runs with interleaved beams with a fixed phase/time between bunches. It was investigated whether the Brock cavity can be used as a phase detector or not. In order to do the measurements, a splitter is attached to the cavity antenna that sends half of the signal to the oscilloscope and the other half to a zero-biased Schottky diode rectifier as shown in Fig. 35. The output of the Schottky diode is connected to a digital voltmeter. Two beams at 249.5 MHz were delivered to the Brock cavity, the arrival time of the first beam is constant while the arrival time of the second beam is varied to pass the bunches of the second beam through the first beam. The output of the voltmeter is shown in Fig. 36, the large peaks happen when the two bunches are separated by 668 ps because the fundamental resonance frequency of the cavity is 1497 MHz and at that frequency all the Fourier series coefficient are activated. The shortest signal of the large peaks (0 ns) corresponds to the situation when the two beams are coincident in time. In this situation the cavity is excited by coherent sum of the two bunches while at the other large peaks, the cavity feels the bunches as individual

¹Simulation is done by Fay Hanon and the results will be published

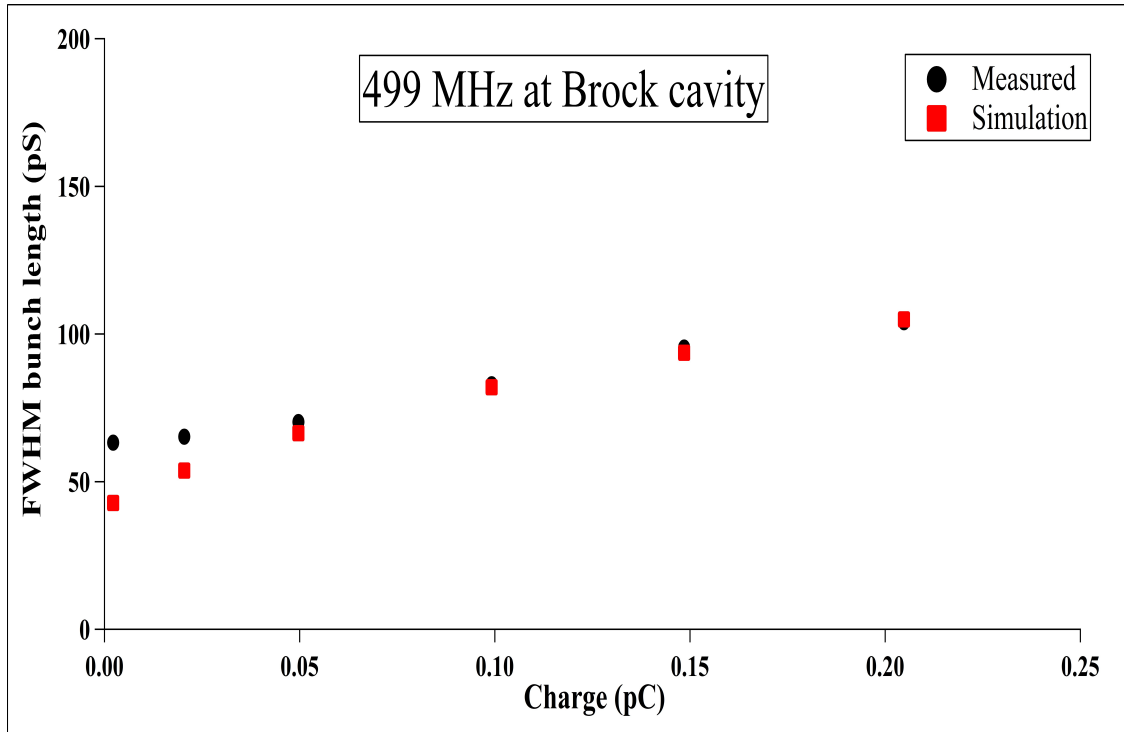


(a) Brock cavity technique

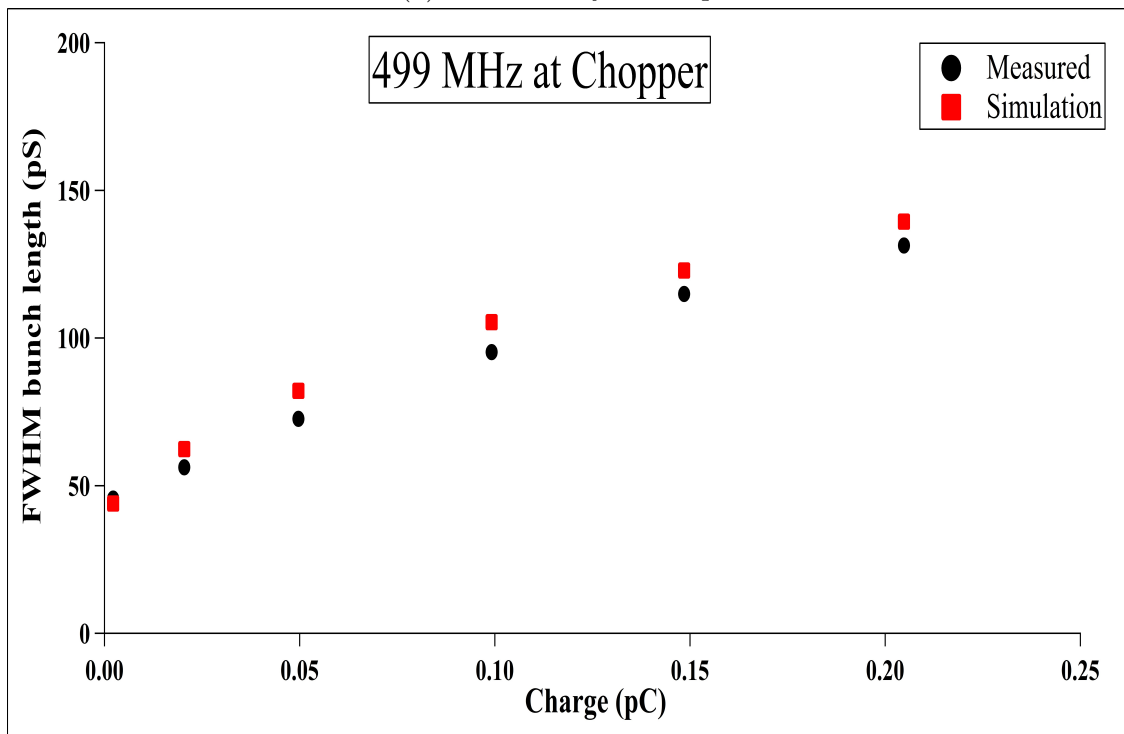


(b) Chopper-slit technique

FIG. 33: Simulated and measured electron bunch length as a function of bunch charge at 249.5 MHz for chopper-slit technique and Brock cavity technique. The uncertainty on the chopper-slit technique data is at most 0.4 ps while on the Brock technique data is at most 0.1 ps and therefore is not visible on the plot.



(a) Brock cavity technique



(b) Chopper-slit technique

FIG. 34: Simulated and measured electron bunch length as a function of bunch charge at 499 MHz for chopper-slit technique and Brock cavity technique. The uncertainty on the chopper-slit technique data is at most 0.3 ps while on the Brock technique data is at most 0.1 ps and therefore is not visible on the plot.

bunches. From these results, it is deduced that the cavity can be used as a phase detector which will provide a quick and accurate method to set the laser phase responsible for the interleaved beams.

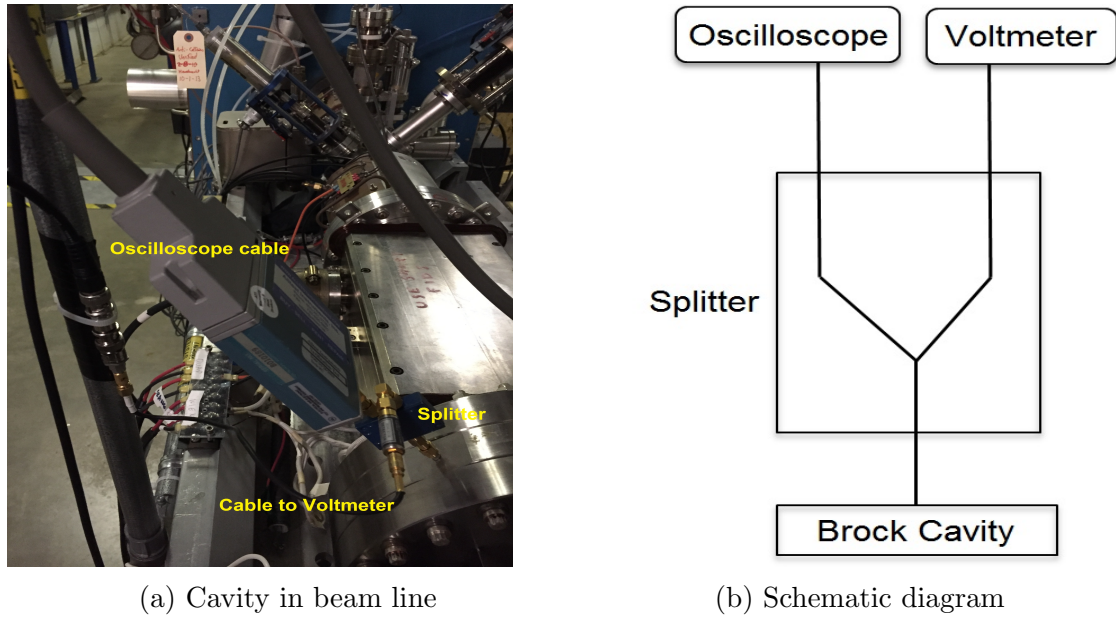


FIG. 35: Brock cavity as phase detector

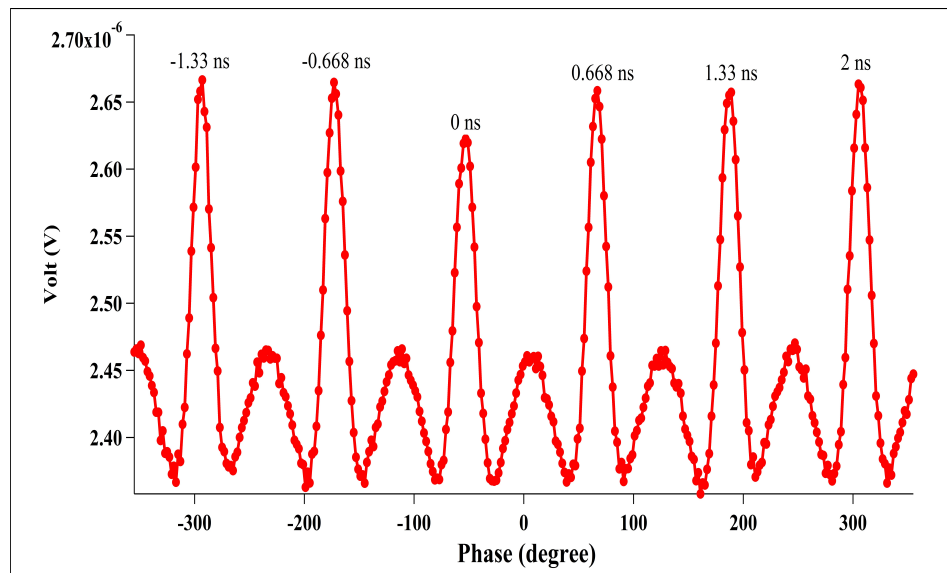


FIG. 36: Voltmeter output as a function of phase

6.2 BUNCH LENGTH IN THE 4D LINE

6.2.1 4D LINE OVERVIEW

The 4D line starts downstream of the two cryomodules. The beam energy is 123 MeV. The first element in the measurement is the injector spectrometer dipole. If the dipole is off, the beam will continue downstream to the injector chicane and when it is on, the beam is deflected to the 4D line. The diagnostic elements in the 4D line are a viewer, BPM, and wire scanner. The viewer is used to view the beam shape and the BPM is used to adjust the beam position. The wire scanner is used for transverse profile measurements.

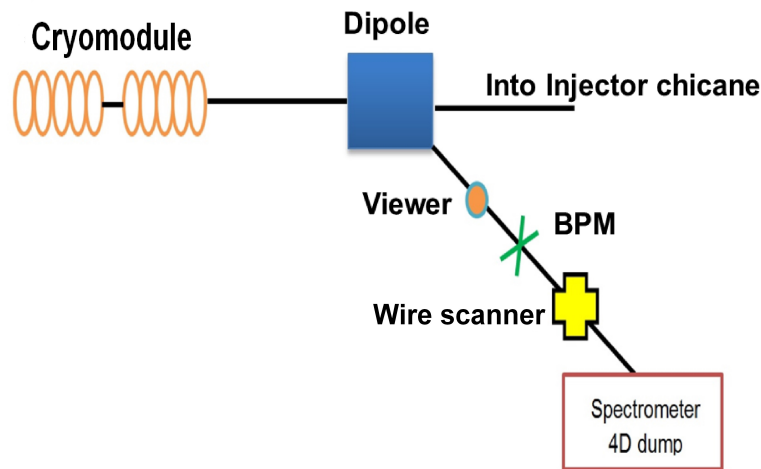


FIG. 37: Schematic drawing for 4D line

6.2.2 RF BACK-PHASING TECHNIQUE

RF back-phasing is a destructive technique used to determine the bunch length in CE-BAF [25]. The basic principle of the technique is to induce an energy spread in the beam bunch related to the bunch length followed by the detection of the spread using the dipole. The energy spread is minimized when the bunch is set on crest of the RF wave and maximized when the bunch is at zero crossing ($\pm 90^\circ$ phase difference). In these cases the head and tail of the bunch receive a different amount of energy. Due to the energy difference, the transverse profile is increased after the beam is deflected by the dipole because the bunch transverse profile is spread in the dispersed direction on the viewer.

The measurement procedure starts by minimizing the BPM before and after the spectrometer to ensure that the beam is on the desired track. The bunch was deflected to the 4D line by using the dipole. The energy spread was minimized by cresting the bunch on the RF wave in the eight cavities of the cryomodule. The viewer was used to monitor the bunch and the wire scanner used to measure the horizontal beam profile of the bunch as shown in Fig. 38. By changing the phase to $\pm 90^\circ$ in the last two cavities, the profile measurement is repeated and the horizontal beam profile is determined as shown in Fig. 38. By knowing the dispersion at the wire scanner position, the bunch length is calculated using Eq. (99) where BL is the bunch length in degrees, B_0 is the magnetic field of the dipole in Tesla when the bunch is on crest, B_+ is the magnetic field when the bunch is off crest, D is the dispersion in cm at the wire scanner position (260 cm), and X_0 and X_+ are the on crest and off crest horizontal distance in cm respectively. The horizontal distance, vertical distance, and magnetic field are shown in Table 5, and the average *rms* value for the bunch length is found to be $80.8 \pm 2.0 \mu\text{m}$.

$$BL = \frac{180}{\pi} \left[\frac{B_+(X_+ - X_0)}{D(B_0 - B_+)} \right]. \quad (99)$$

TABLE 5: Back-phasing results

	Sigma X (cm)	Sigma Y (cm)	Bdl (T cm)
On crest	0.026 ± 0.001	0.025 ± 0.001	148873.875
+90 ⁰ off crest	0.444 ± 0.014	0.025 ± 0.001	93523.875
-90 ⁰ off crest	0.389 ± 0.006	0.024 ± 0.001	93523.875

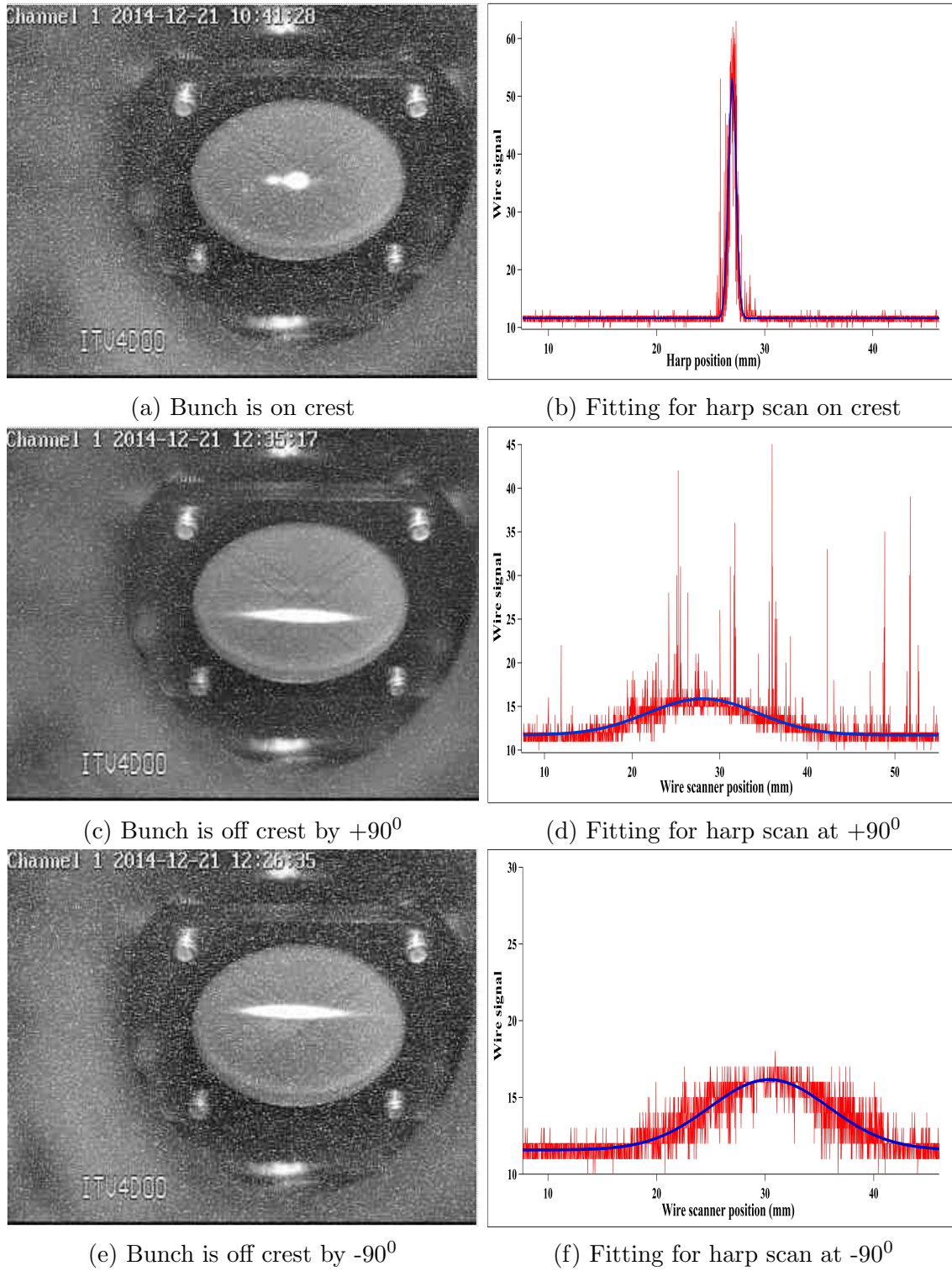


FIG. 38: Back-phasing results

6.3 BUNCH LENGTH IN THE INJECTOR CHICANE

6.3.1 EXPERIMENT SETUP

The injector chicane consists of four dipole magnets with nine quadrupole magnets interspersed between them. Each dipole magnet is 30 cm long with a bending angle of 5.5° . The beam path has a bending radius of 3.125 m and so the magnetic field strength is 1.3128 kG at 123 MeV as calculated from Eq. (100)

$$\rho = \frac{\beta E(\text{GeV})}{B(\text{T}) \times 0.2998}. \quad (100)$$

The experiment location is chosen to be after the fourth dipole because the bunch will be fully compressed there. After the third dipole, the bunch is compressed only half as much. Analytical calculations and ELEGANT simulations of the bunching were performed and showed the same result.

A mirror is used to deflect the SR from the fourth dipole into the interferometer optical path. The mirror is placed 30.5 cm away from the end of the dipole and 12 mm from the center of the beam line to prevent the damage of the mirror from beam halo and to allow sufficient clearance for robust beam transport as shown in Fig. 39.

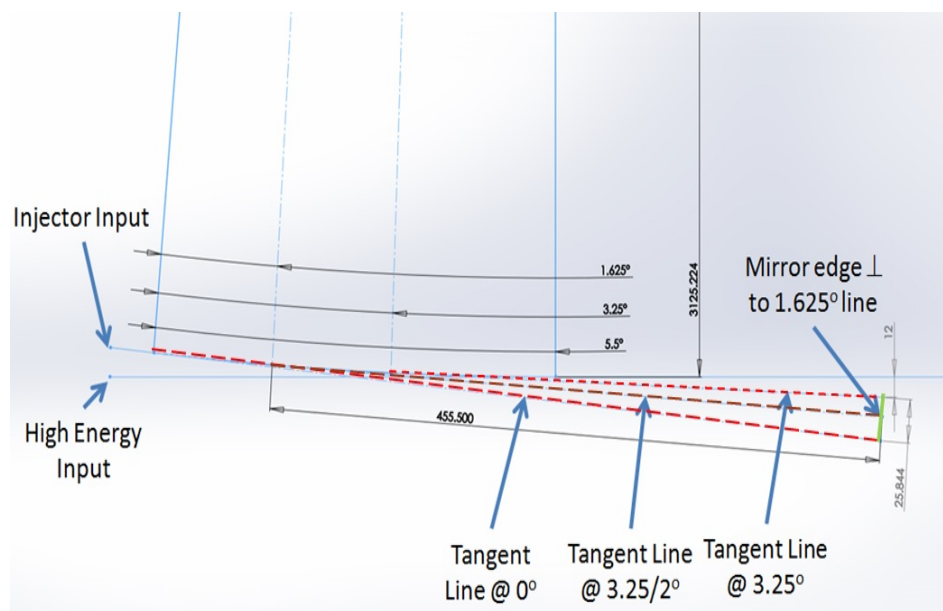


FIG. 39: Schematic diagram for the SR coming from the injector chicane fourth dipole. The solid blue lines represents the ends of the dipole. The mirror is 455.5 mm from the center of the arc from where SR hits the mirror.

Normally the vertical opening angle is $1/\gamma$ but since the radiation is in the low frequency range ($\omega \ll \omega_c$) then the opening angle must be calculated from Eq. (101) [34]

$$\theta_c = \frac{1}{\gamma} \left(\frac{2\omega_c}{\omega} \right)^{\frac{1}{3}}, \quad (101)$$

where ω_c is the critical frequency and ω is the frequency of interest. At 3 THz and 123 MeV beam energy, the vertical opening angle is 0.025 rad which means that the mirror will accept all the radiation because the vertical photon beam size is about 11.4 mm. In order to know how much power the mirror will accept, Eq. (55) is used to calculate the energy per bunch and the power is calculated by multiplying the energy by the bunch repetition rate of 499 MHz and the fractional mirror acceptance of $3.25^0/360^0$. The total power is calculated for different currents and shown in Table 6, and the power spectrum for different beam currents is shown in Fig. 40.

TABLE 6: Estimated power for different beam current

Current	Charge	No. of electrons	Power
50 (μA)	0.1 (pC)	6.25×10^5	41.26×10^{-3} (J/s)
20 (μA)	0.04(pC)	2.5×10^5	6.60×10^{-3} (J/s)
10 (μA)	0.02(pC)	1.25×10^5	1.65×10^{-3} (J/s)
5 (μA)	10 (fC)	6.25×10^4	0.41×10^{-3} (J/s)
50 (nA)	0.1 (fC)	625	0.41×10^{-7} (J/s)

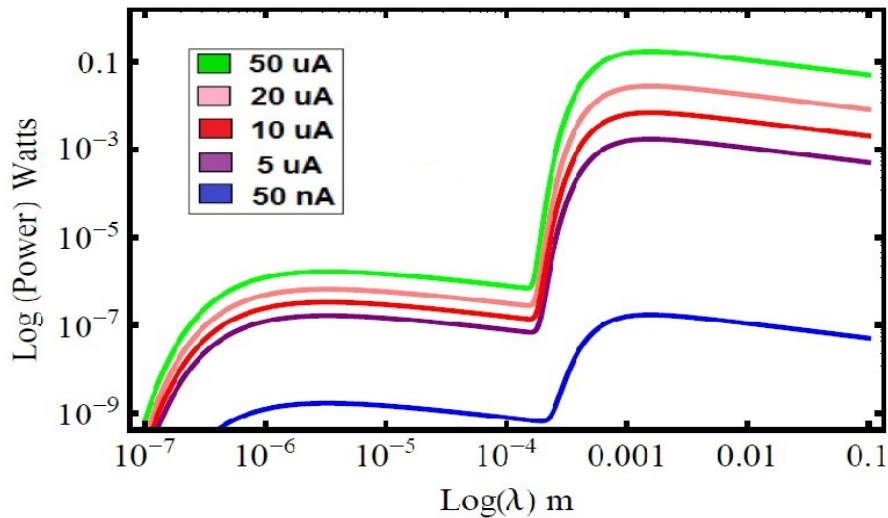


FIG. 40: Estimated power spectrum for different beam current

Since the electron beam goes through the dipole fringe field, edge radiation is expected to contribute to the radiation. The edge radiation calculations are done similarly to those in [42]. The edge radiation parameters for CEBAF are shown in Table 7, where λ is the wavelength of the interest, λ_c is the critical wavelength, R is the bending radius, L is the distance between the dipoles, and δ and ϕ are the edge radiation parameters.

TABLE 7: Edge radiation parameters

Parameter	Value
λ	100 μm
λ_c	0.935 μm
R	3.125 m
L	10.5 m
δ	0.00538
ϕ	11.2

According to [42], when $\delta \ll 1$ the synchrotron radiation has a small contribution to the radiation and the edge radiation will be dominant. When $\phi \gg 1$ the edge radiation becomes collimated. As indicated from the table, the value of δ shows that edge radiation will dominate at low frequency (0.3 THz) while at high frequency (3 THz) a contribution from synchrotron radiation will appear in the radiation profile. The value of ϕ shows that the radiation will be collimated. Since there are two dipoles in that study, a diffraction pattern is expected to appear due to radiation from the third chicane dipole. To study the effect of ER and SR at the mirror location in the vacuum chamber, the SRW code is used [43] by using IGOR-PRO [44]. The SRW code simulates the radiation intensity at the mirror location. Fig. 41(a) shows that there will be only edge radiation at 0.3 THz.

The two doughnuts represent the ER coming from the entrance and exit of the fourth dipole. More intensity comes from the exit of the fourth dipole. The mirror is 1 inch \times 1 inch (at 45° to the vertical) and located in the middle of the distance between the two doughnuts. As the frequency increases (shorter wavelength), the SR contributes more to the radiation intensity as shown in Fig. 41(b). The two doughnuts represents the edge radiation and between them the diffraction patterns and the SR. The diffraction patterns comes from the third dipole contribution and the patterns may be due to the ER or SR.

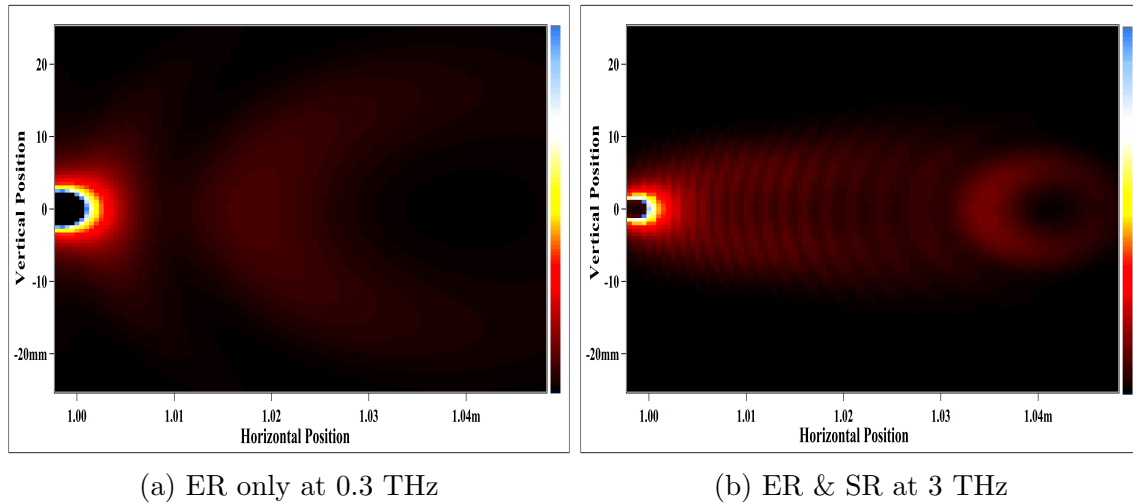


FIG. 41: Radiation intensity for different frequencies around the mirror location. The color key on the right of the figure represents the intensity where the dark red is the minimum value and equals 3.1×10^5 photons/mm². The dark blue represents the maximum intensity and equals 8.99×10^7 photons/mm².

6.3.2 CHAMBER CONSTRUCTION

To collect the Coherent Synchrotron Radiation (CSR), a new vacuum chamber was constructed. The chamber is built in a way similar to the previous chamber except that it has additional ports as shown in Fig. 42.



(a) Old beam line

(b) New beam line

FIG. 42: Old and new beam line

The new chamber is made from 316 stainless steel with the same thickness as the old one in order to have the same magnetic permeability. The elastic limit for the vacuum chamber is simulated and found to be 70 MPa which is much less than the elastic limit of the stainless steel. The chamber has two assemblies, one for the alignment diode laser and the other for the SR mirror which will reflect the SR upward to the interferometer. Both of them are mounted on a rotatable flange with jacking screws to provide small angular corrections as shown in Fig. 43.

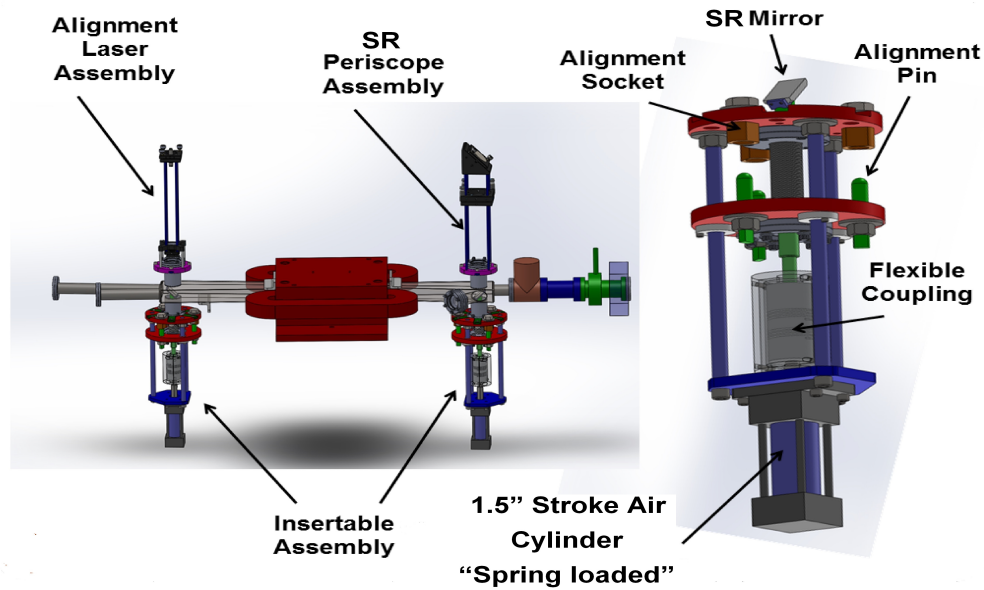


FIG. 43: Chamber assemblies

The two assemblies are attached to stroke air cylinders which are spring loaded to fall-out in case of pressure loss or electrical power signal loss. A laser alignment is done in the lab to ensure that the radiation will hit the middle of the mirror. Also, a vacuum check is done in the lab to ensure that there is no leakage in the chamber before it was installed in the tunnel. After the chamber was installed in the tunnel, another laser alignment was done by using a diode laser to ensure that the SR-mirror is not affected by the installation process.

6.3.3 OPTICAL LINE

To deliver the SR from the optical port to the real time interferometer (RTI), a table and an optical line consisting of plane mirrors, a concave mirror, an optical chopper (Thorlab), a polarizer (Microtech instruments G45-s), two irises, and two cameras (Mini Bullet ExView B/W) facing the two irises was built. All the optical line components are set on a 30.5 cm ×

45.7 cm breadboard and are installed as shown in Fig. 44. The table is 132.1 cm \times 77.5 cm and made from aluminum. It has an aperture aligned with another one in the breadboard with a diameter 5.7 cm over the optical port. The table is supported to ground by four foot anchors to prevent any movement. The SR coming from the optical port will hit plane Mirror (1) mounted at 45° to reflect the radiation to the concave mirror with a 1016 mm focal length. The concave mirror will reflect and focus the radiation to Mirror (2).

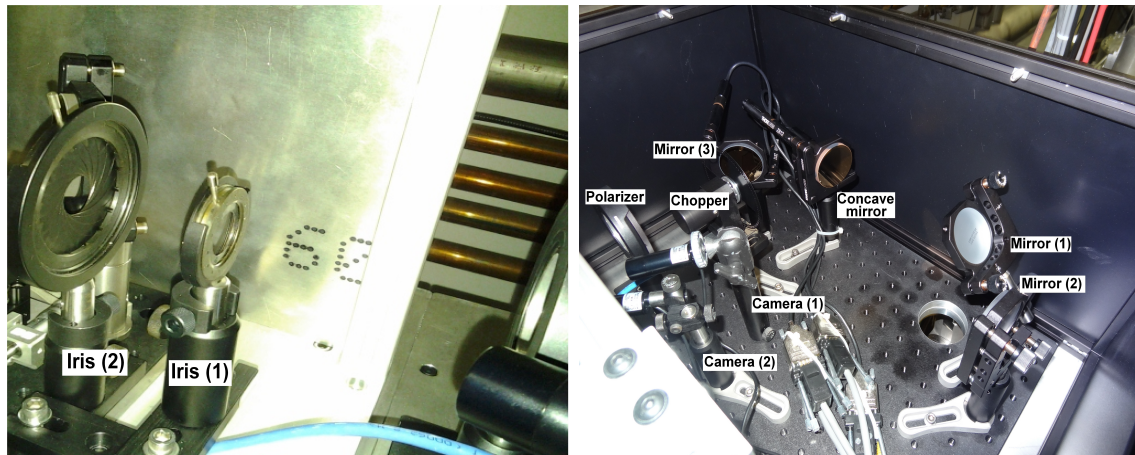
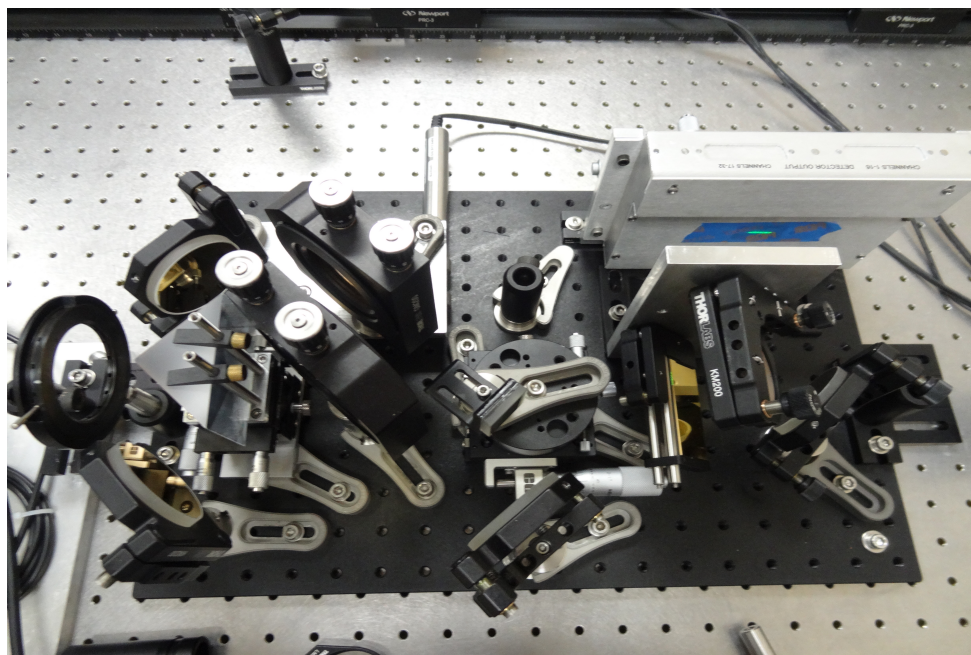


FIG. 44: Optical line

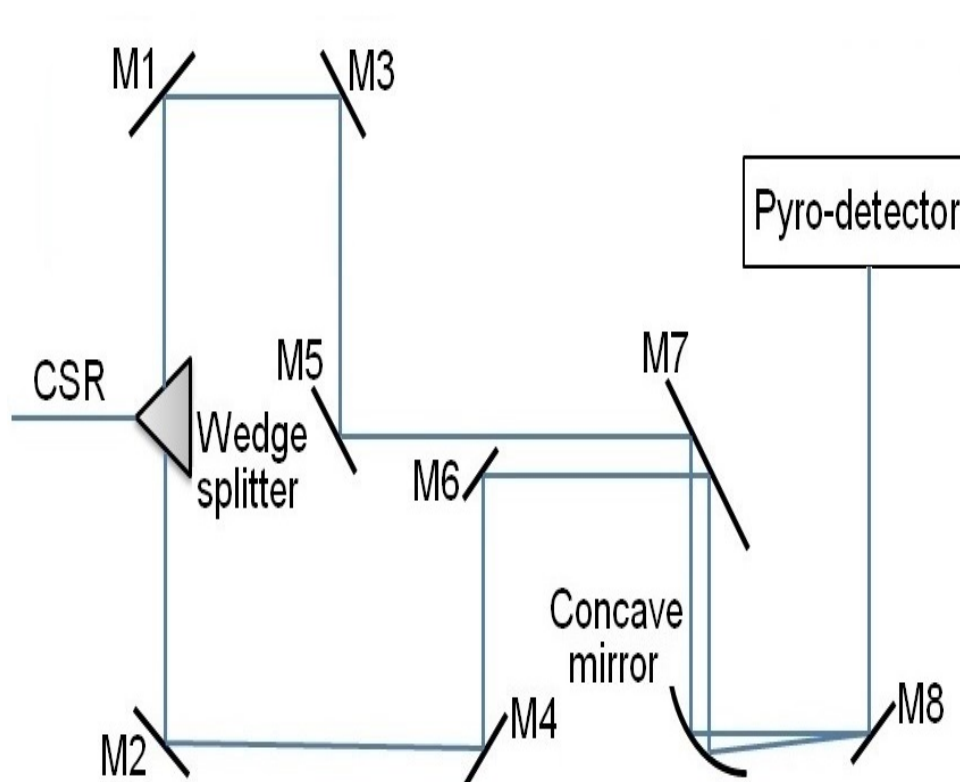
The SR has several reflections through the other mirrors until it goes through the chopper. The concave mirror and Mirror (3) have two remotely controlled steerers which move the radiation vertically or horizontally to do a fine alignment in case it is needed. The optical chopper is set at 25 Hz repetition rate. As the radiation passes the chopper, it will meet the polarizer. The polarizer is a wire grid that transmits 99% of the perpendicular field while it transmits 1% of the parallel field at 1 THz. Two irises are installed after the polarizer to define the radiation before it goes to the RTI.

6.3.4 RADIABEAM REAL TIME INTERFEROMETER

The RTI consists of a wedge splitter, plane mirrors, a concave mirror, and a pyro-detector array as shown in Fig. 45. The pyro-detector contains 32 elements. Each element is 0.5 mm by 1 mm and consists of a 25 μm thick LiTaO₃ crystal. The crystal is coated with chromium to increase its sensitivity in the range 0.2 THz to 20 THz (1.5 mm to 15 μm) [17].



(a) RTI components



(b) Schematic diagram for RTI

FIG. 45: Radiabeam Real Time Interferometer

The output of the detector is proportional to the signal coming into the 32 elements. After the installation of all the components is completed, a diode laser is used to align the optical line and the RTI. The motors, chopper, and the pyro-detector are remotely controlled. The RTI and the optical line are covered by a box to prevent it from misalignment or accidental damage. Lead bricks are used upstream of the box to shield the detector from any radiation coming from the CEBAF recombining.

6.3.5 EXPERIMENTAL DATA

The RTI is a non-invasive monitor as it does not interrupt beam delivery. The SR mirror was inserted and retracted numerous times to check if it has any effect on the beam stability. The test showed that the mirror has no effect on the beam stability. The background for the RTI is recorded before any experimental data is taken. The experiment was completed with up to 50 μA beam current. The two cameras did not detect any light, the oscilloscope did not give a beam related CSR signal, and the traces were close to the background. Camera (1) and Camera (2) did not detect any light because the visible light coming from the SR is less than the camera sensitivity limit. In order to explain why the detector did not give a noticeable beam related signal, several possibilities were investigated.

Window transmission

The window material is z-cut crystal quartz. The transmission curve is shown in Fig. 13. As shown from the green curve, the transmission will increase after 80 μm and will reach more than 75% at about 100 μm but there is abrupt decrease in the transmission to less than 50% between 70 μm and 80 μm . This will decrease the total power transmitted by a small factor. To overcome this effect, other materials could be used such as TPX and diamond. TPX is the lightest polymer and it is transparent in the THz range. It has a better transmission than the quartz crystal and the transmission increases to about 90% above 400 μm as shown in Fig. 13. But since the chamber is under vacuum, it cannot be used because it will not sustain the pressure and will crack. Diamond can sustain the pressure and has a constant transmission about 70% for the interesting range as shown in Fig. 13, but it is expensive.

Optical transport assembly

Another possibility for no beam related signal to check is that the SR is not propagating through the optical transport assembly of the chamber. A digital camera (Prosilica GC650)

is installed close to Mirror (1) in the optical line to check if there is synchrotron light present or not when the mirror is inserted as shown in Fig. 46. The mirror is inserted and retracted as the beam is on. The check shows that there is light coming when the mirror is inserted as shown in Fig. 47 which means that the mirror is installed in the right position. The coherent synchrotron emission is on the same path as the synchrotron light with wider angular spread as discussed previously.

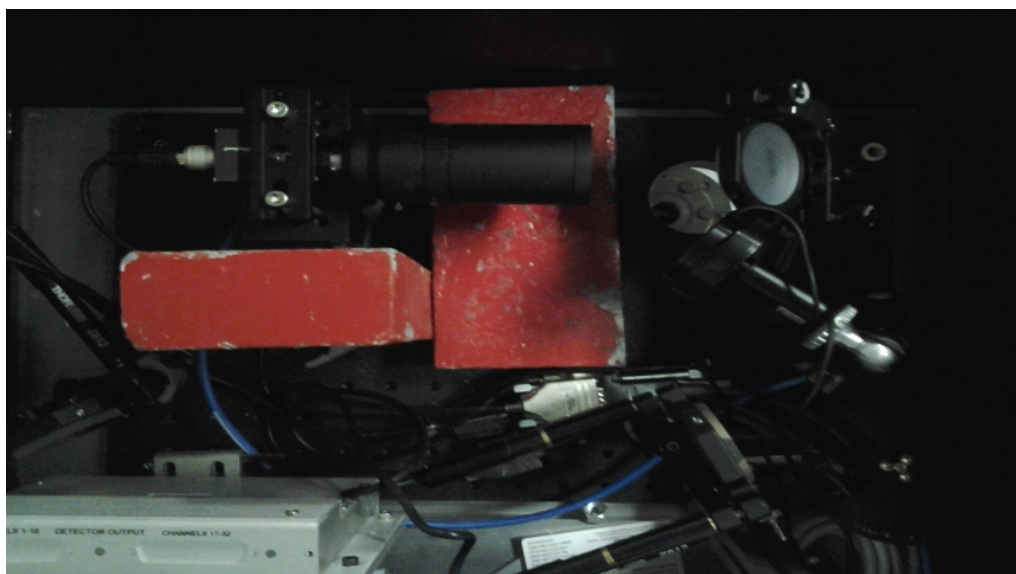
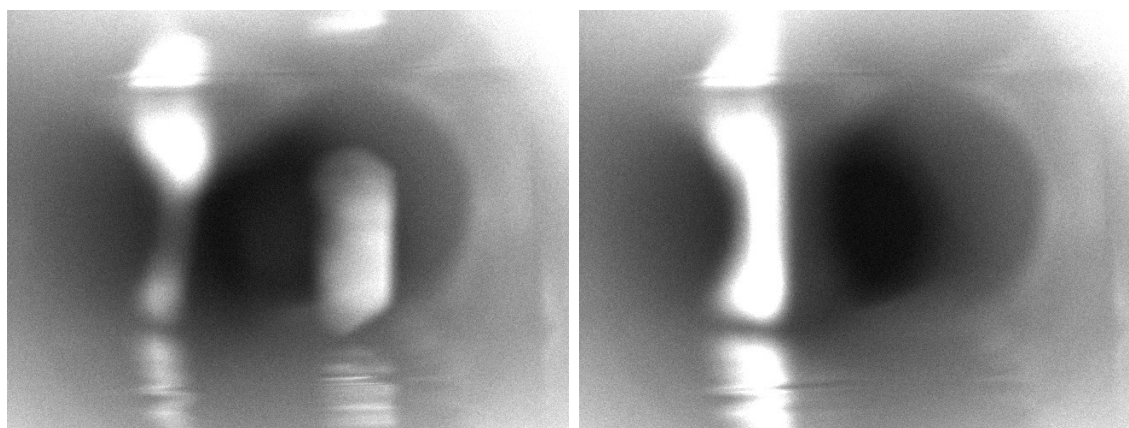


FIG. 46: Camera is installed to check the light coming from the optical port



(a) Mirror in

(b) Mirror out

FIG. 47: Camera output when SL mirror is inserted and retracted

Mirror reflectivity

Another possibility that may have an effect on the radiation is the reflectivity of the mirrors. The mirrors used in the experiment are coated with gold which has about 99.5% reflectivity and the SR power is expected to be less by about 7% because fourteen mirrors are used. According to [45], different metal coated mirrors were tested and compared. It was found that gold, silver, and aluminum coatings perform equally in the THz regime, so there is no reason to change the mirrors in order to decrease the loss from the mirrors.

Polarizer

Since CSR has seven times much energy radiated with the parallel polarization than the perpendicular polarization [34], then the parallel component is preferred. The polarizer has about 99% transmission to the perpendicular field and about 1% for the parallel field at 1000 GHz, so if the polarizer is installed in an inverted way the transmission will be 1%. In order to investigate this, the polarizer was taken out and the detector is set in the polarizer location. The experiment is done again at 10, 15, and 50 μA at 249.5 MHz repetition rate. The oscilloscope traces were found to be the same as before without a noticeable change as shown in Fig. 48, so it is clear that polarizer is not changing the signal detected.

Chopper

The integration time of the detector depends on the frequency of the chopper. In order to check the effect of the chopper frequency on the experiment, the chopper frequency changed from 1 Hz to 100 Hz in steps of 25 Hz. The oscilloscope output traces did not give a noticeable signal change as shown in Fig. 49. The only difference is that the detector takes proportionately more time to give the output signal and it takes more time at 1 Hz than 100 Hz.

Detector

The preceding analysis does not explain the lack of signal response from the RTI. The detector was relocated to be very close to the optical port to decrease the amount of radiation loss. The CSR will hit four mirrors instead of ten mirrors before it is received by the detector as shown in Fig. 50. The output signal did not change which indicates that the background noise is greater than the SR energy. To know how much signal power is needed to overcome

the background noise, the estimated power was calculated for the 32 channels of the detector and are shown in Table 8.

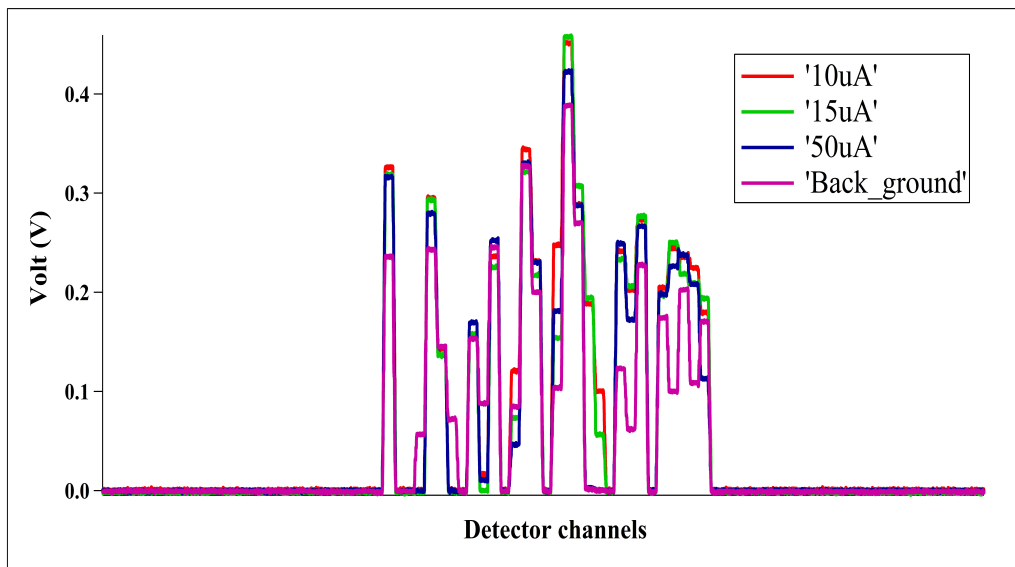


FIG. 48: Oscilloscope traces at different currents

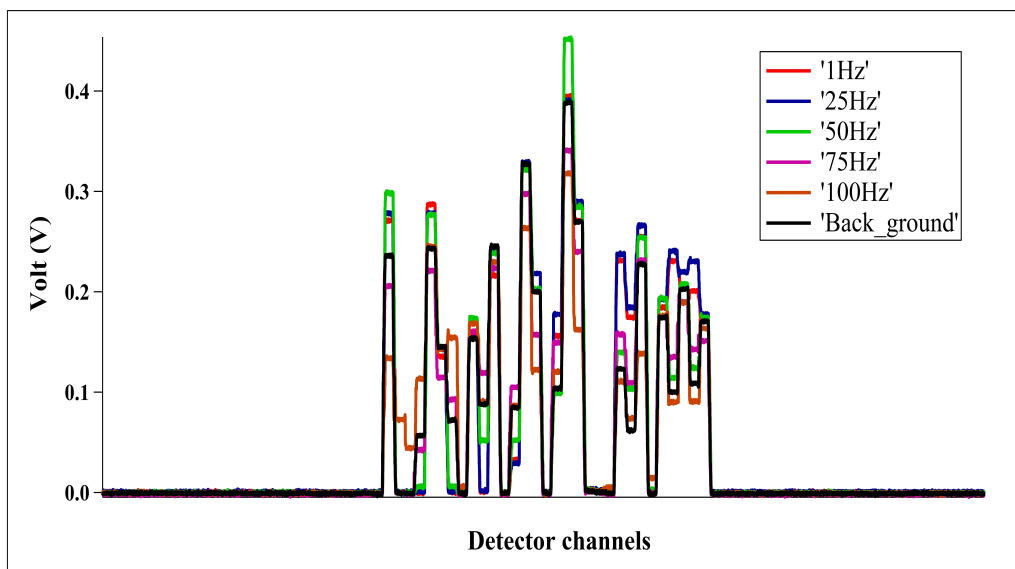


FIG. 49: Oscilloscope traces at different chopping frequencies

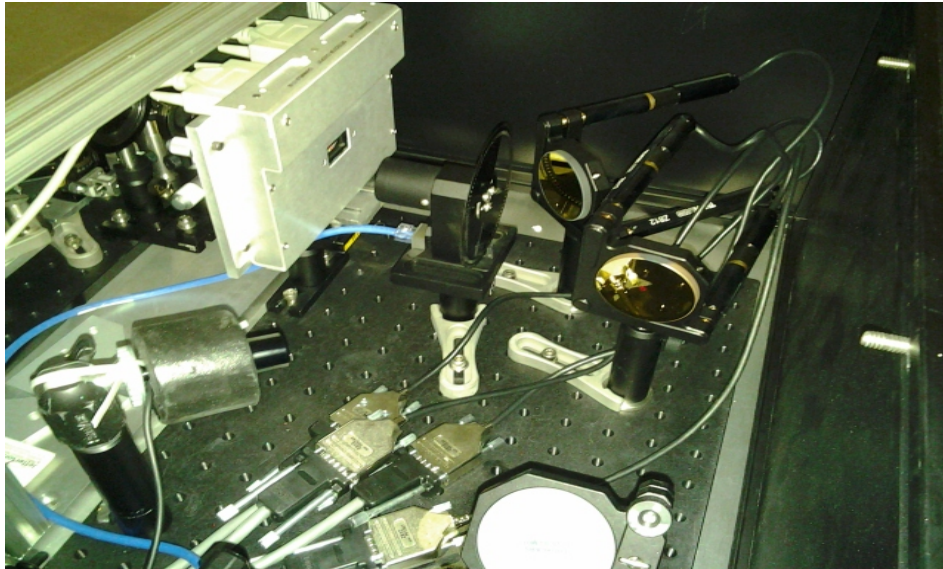


FIG. 50: Detector installed in a new position

TABLE 8: Estimated power for the detector's channels at $50 \mu\text{A}$

Channel	Power (W)	Channel	Power (W)
1	4.97×10^{-2}	17	2.44×10^{-7}
2	4.11×10^{-3}	18	2.48×10^{-7}
3	1.06×10^{-5}	19	2.51×10^{-7}
4	1.58×10^{-7}	20	2.55×10^{-7}
5	1.69×10^{-7}	21	2.58×10^{-7}
6	1.79×10^{-7}	22	2.61×10^{-7}
7	1.88×10^{-7}	23	2.64×10^{-7}
8	1.96×10^{-7}	24	2.67×10^{-7}
9	2.03×10^{-7}	25	2.70×10^{-7}
10	2.09×10^{-7}	26	2.73×10^{-7}
11	2.15×10^{-7}	27	2.75×10^{-7}
12	2.21×10^{-7}	28	2.78×10^{-7}
13	2.26×10^{-7}	29	2.80×10^{-7}
14	2.31×10^{-7}	30	2.82×10^{-7}
15	2.35×10^{-7}	31	2.85×10^{-7}
16	2.40×10^{-7}	32	2.87×10^{-7}

6.4 SYNCHROTRON LIGHT MONITOR

After the bunch is fully compressed in the injector chicane, it goes into the North linac (NL) and leaves the NL at an energy up to 1.2 GeV. Arc1 and Arc2 have high dispersion points ($\eta_x \sim 5$ m) at the central dipole. At these two points, a synchrotron light monitor (SLM) is used to determine the bunch length in the linac. The SLM has a receiving port where the SR goes through it and then hits a plane mirror to reflect the light onto another plane mirror. The second mirror will reflect the light to a digital camera through a second port. The image of the light is sent to the control room through the epics control system. The construction of the SLM is shown in Fig. 51.

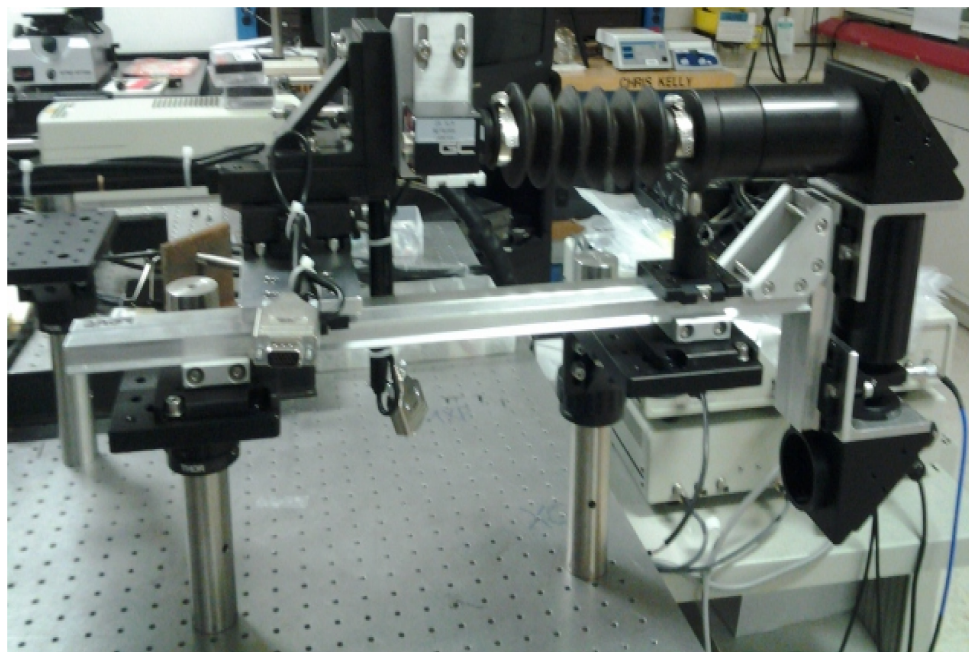
The measurement is done by first putting the bunch on crest to ensure minimum energy spread. As the NL gang phase changes, the energy spread will change and the spot size will increase. The NL gang phase is increased and decreased by one degree steps around the on crest phase. At each phase a picture of the spot is captured. By determining the spot size at each phase and plotting the relation between the spot size and the phase, a hyperbolic curve is obtained. From the slope of the asymptotes of the hyperbola, the bunch length is determined.

The Arc1 and Arc2 SLMs can detect changes in the energy spread for cases when the emittance and beta function are at the normal values. The bunch length measurement is in parallel to [37], the minimum energy spread happens when the bunch is on crest and changing the gang phases of the North Linac (NL) will increase the energy spread. The energy spread increase in the Arc1 is countered by a compensating change in the South Linac (SL) gang phase in case the measurement is done during the operation of the halls. This means, bunch length measurements can be completed without disturbing normal CEBAF operations.

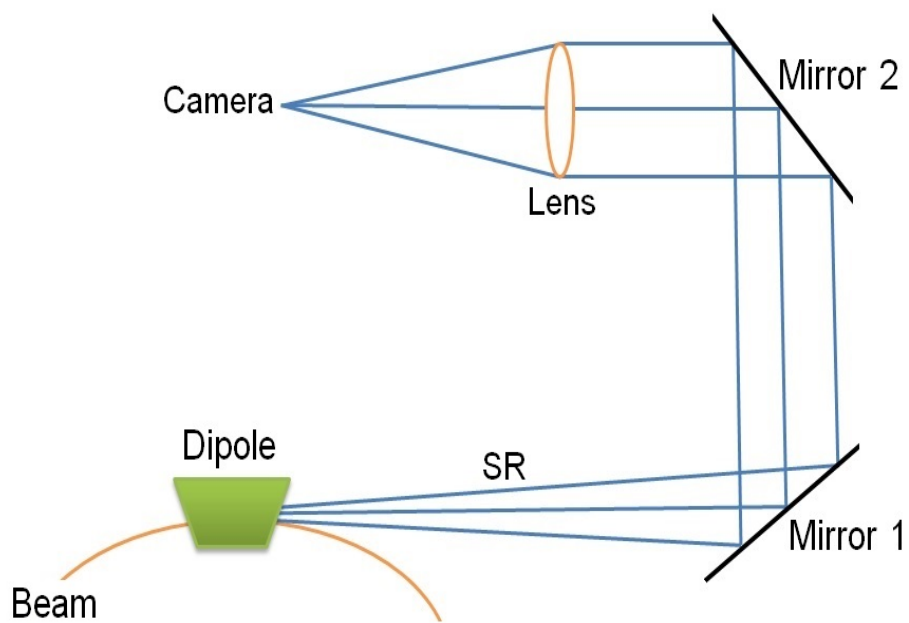
6.4.1 SLM ANALYSIS

Begin by characterizing a beam with a finite bunch length with coordinates (x, y, z, δ) where (x, y) are the transverse coordinates of the bunch, z is the longitudinal coordinate along the bunch, and δ is the relative energy deviation from the average bunch energy. When a beam with finite bunch length passes through off-crest cavities, a $z - p_z$ correlation (energy chirp) is introduced which in turn will affect the bunch size of the beam². The bunch longitudinal positions will be redirected into a transverse position spreading after passing through the dipole with the SLM port. The beam energy in Arc1 is the sum of the injector

²Derivation is provided by Michael Tiefenback



(a) SLM in lab before installation



(b) Schematic diagram for SLM

FIG. 51: Synchrotron light monitor

energy (E_{inj}) and the energy gain from the NL (E_{NL})

$$E = E_{inj} + E_{NL} \cos(kz + \phi), \quad (102)$$

where k is the wave number of the RF and ϕ is the linac phase shift. The energy locks are used to assure that the total beam energy in the Arc1 is constant.

$$E = E_{inj} + \frac{E_{NL}}{\cos(\phi)} \cos(kz + \phi). \quad (103)$$

Because kz is very small, to the first order Eq. 103 can be written as

$$E = E_{inj} + E_{NL} + E_{NL}kz \tan(\phi). \quad (104)$$

The relative energy error along the bunch due to the phase shift (ϕ) with respect to the intrinsic bunch length is

$$\delta = \frac{E - \bar{E}}{\bar{E}} = \frac{E_{NL}}{E_{inj} + E_{NL}} kz \tan \phi, \quad (105)$$

where \bar{E} is the average energy of the bunch ($E_{inj} + E_{NL}$). The beam distribution can be represented via a distribution function $F(x, y, z, \delta)$ that is separable with the longitudinal dimension (z) and energy spread (δ) independent of the transverse dimensions.

$$F(x, y, z, \delta) = f(x, y)Z(z)g(\delta). \quad (106)$$

The mean square of the energy spread (δ) and the bunch length (z) before the chirp are given by

$$\langle z_0^2 \rangle = \int \int \int \int z^2 f(x, y)Z(z)g(\delta) d\delta dz dx dy, \quad (107)$$

$$\langle \delta_0^2 \rangle = \int \int \int \int \delta^2 f(x, y)Z(z)g(\delta) d\delta dz dx dy. \quad (108)$$

By adding a chirp, a new distribution function for the energy deviation is

$$G(\hat{\delta}) = g(\delta - \lambda z), \quad (109)$$

where λ is the chirp factor. The new mean square values after applying the chirp are

$$\begin{aligned} \langle z^2 \rangle &= \int \int \int \int z^2 f(x, y)Z(z)g(\delta - \lambda z) d\delta dz dx dy \\ \langle z^2 \rangle &= \int \int \int \int z^2 f(x, y)Z(z)G(\hat{\delta}) d\hat{\delta} dz dx dy \\ \langle z^2 \rangle &= \langle z_0^2 \rangle, \end{aligned} \quad (110)$$

$$\begin{aligned}
\langle \delta^2 \rangle &= \int \int \int \int \delta^2 f(x, y) Z(z) g(\delta - \lambda z) d\delta dz dx dy \\
\langle \delta^2 \rangle &= \int \int \int \int (\hat{\delta} + \lambda z)^2 f(x, y) Z(z) G(\hat{\delta}) d\hat{\delta} dz dx dy \\
\langle \delta^2 \rangle &= \int \int \int \int (\hat{\delta}^2 + 2\lambda z \hat{\delta} + \lambda^2 z^2) f(x, y) Z(z) G(\hat{\delta}) d\hat{\delta} dz dx dy.
\end{aligned} \tag{111}$$

Because the distribution function is uncorrelated in these parameters, the cross term goes to zero and

$$\langle \delta^2 \rangle = \langle \delta_0^2 \rangle + \lambda^2 \langle z_0^2 \rangle. \tag{112}$$

The beam spot grows due to this energy spread when $\eta_x \neq 0$. To calculate the spot size, represent the beam by a new distribution $f(\hat{x}, y) = f(x - \eta_x \delta, y)$. The mean square for the transverse position is given by

$$\begin{aligned}
\langle x^2 \rangle &= \int \int \int \int x^2 f(x - \eta_x \delta, y) Z(z) g(\delta) ds dz dx dy \\
\langle x^2 \rangle &= \int \int \int \int (\hat{x} + \eta_x \delta)^2 f(\hat{x}, y) Z(z) g(\delta) ds dz d\hat{x} dy.
\end{aligned} \tag{113}$$

Again, the cross term is zero because the longitudinal distribution function is uncorrelated with transverse coordinates, thus

$$\langle x^2 \rangle = \langle x_0^2 \rangle + \eta_x^2 \langle \delta^2 \rangle. \tag{114}$$

The $z - p_z$ correlation is the sum of all correlations from the injector to the north linac and the sum may be set to zero by adjusting the NL gang phase because the correlations are linear. The result for beam size on the SLM, substituting Eq. (112) into Eq. (114), is

$$\langle x^2 \rangle = [\langle x_0^2 \rangle + \eta_x^2 \langle \delta_0^2 \rangle] + \eta_x^2 \lambda^2 \langle z_0^2 \rangle. \tag{115}$$

As a result of running the NL off crest, a quadratic term is added to the beam size from the induced energy spread. This term will dominate the measurement if the beam size is more than three times the minimum beam size and it is proportional to the root mean square of the bunch length. When there is no chirp, δ is equal to λz and from Eq. (105)

$$\lambda = \frac{E_{NL} k \tan(\phi)}{E_{inj} + E_{NL}} = \frac{E_{NL} k \phi}{E_{inj} + E_{NL}}. \tag{116}$$

Substituting from Eq. (116) into Eq. (115)

$$\langle x^2 \rangle = [\langle x_0^2 \rangle + \eta_x^2 \langle \delta_0^2 \rangle] + \left[\frac{\eta_x E_{NL} k}{E_{inj} + E_{NL}} \right]^2 \langle z_0^2 \rangle \phi^2. \tag{117}$$

Plotting x versus ϕ will give a hyperbolic plot and the asymptotes of the hyperbolas will have a slope proportional to the beam size. Fitting $[x^2 = a^2 + b^2\phi^2]$ to the results, the bunch length will be given by

$$z_0 = \frac{b(E_{inj} + E_{NL})}{\eta_x E_{NL} k}. \quad (118)$$

6.4.2 EXPERIMENTAL RESULTS

The measurement begins by putting the bunch on crest to ensure minimum energy spread. As the NL gang phase changes, the energy spread will change and the spot size will increase as shown in Fig. 52. When the NL gang phase changed in the positive direction, the beam spot shows a tail which increases with increasing phase. The dispersive contribution becomes dominant (the spot length is almost three times the on crest spot size) as shown in Fig. 52b - Fig. 52e. When the phase goes in the negative direction, the tail is still there but inverted as shown in Fig. 52f - Fig. 52i which means that it is a beam property.

It is convenient to calibrate dispersion and beam size together using the camera as shown in Fig. 53. The beam energy is changed by ± 1 MeV and the beam displacement on the SLM is measured. For example, if the total energy is 1000 MeV and the energy gain is changed by 1 MeV then the relative energy shift is 1×10^{-3} .

Two different measurements are used to estimate the bunch length. The first is an edge measurement done by measuring the transverse spot size from edge to edge. The measurement is done ignoring camera saturation and provides an upper bound for bunch length. The other measurement is *rms* based and suffers from camera saturation. The *rms* calculations begin by using a MATLAB [46] code to remove the image frame, subtract the background and convert the image into a 2D matrix. A horizontal projection is done to the output matrix for each figure. A Gaussian fit is made and the resulting sigma is taken as the beam width. Plotting the sigma versus the phase change will give a hyperbola and by knowing the slope of the asymptotes, the bunch length can be calculated. The *rms* calculations are expected to be overestimated because of the camera saturation. The two measurements and hyperbolic fits are shown in Fig. 54 and Fig. 55 for Arc1. The slope of Fig. 54 has the highest slope which means a higher indicated bunch length. This is expected since the full width is for a head to tail spread measurement.

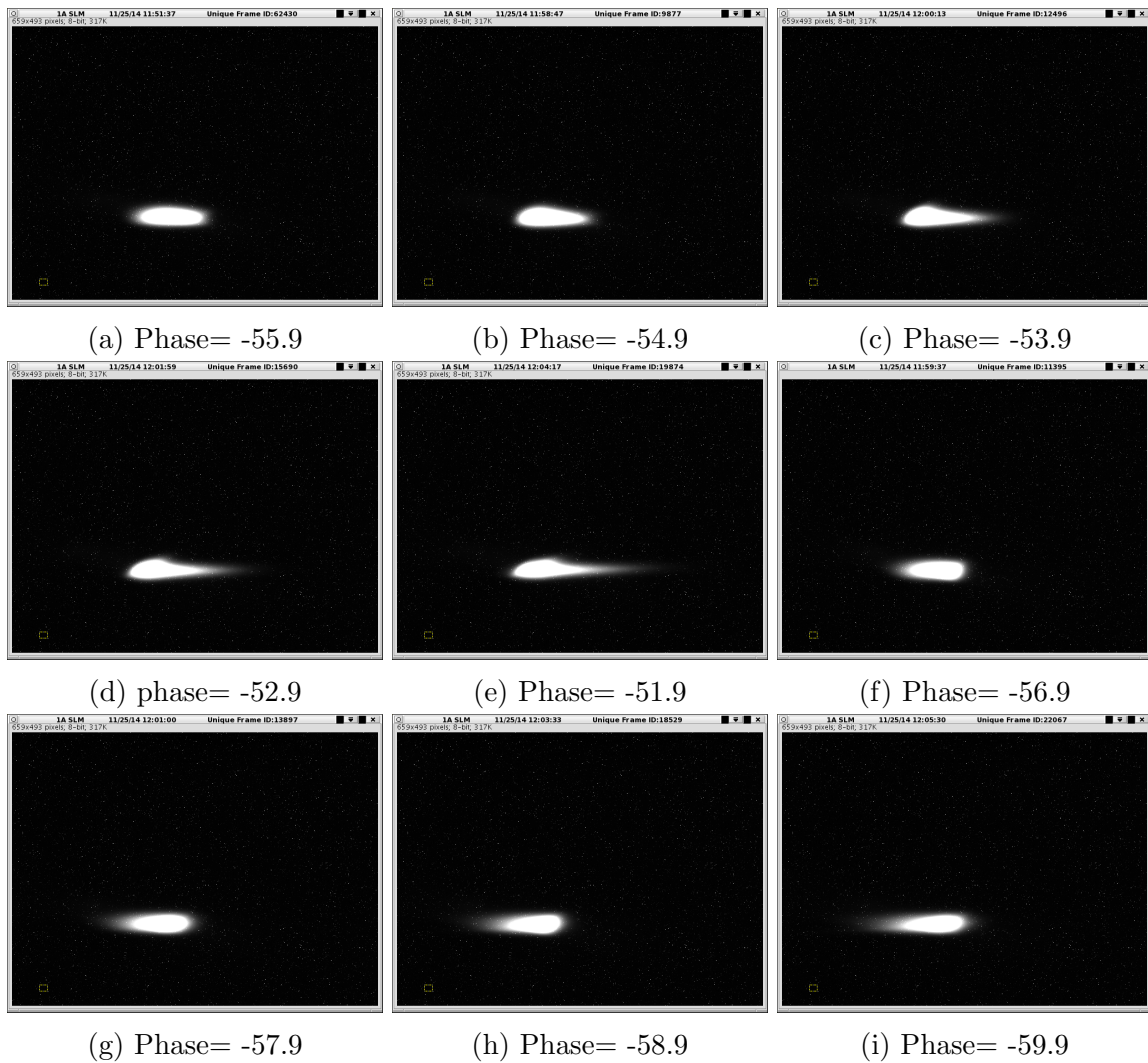


FIG. 52: The spot length on SLM changes as the NL gang phase changes.

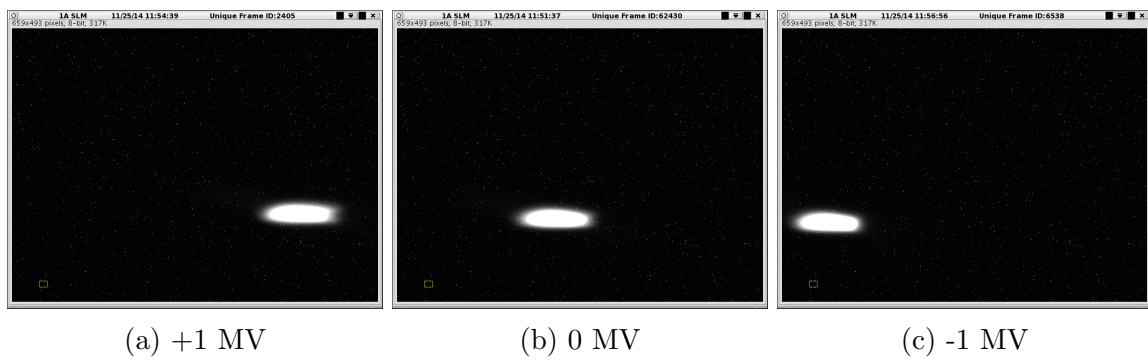


FIG. 53: Changing the gradient by ± 1 MV to calculate the dispersion.

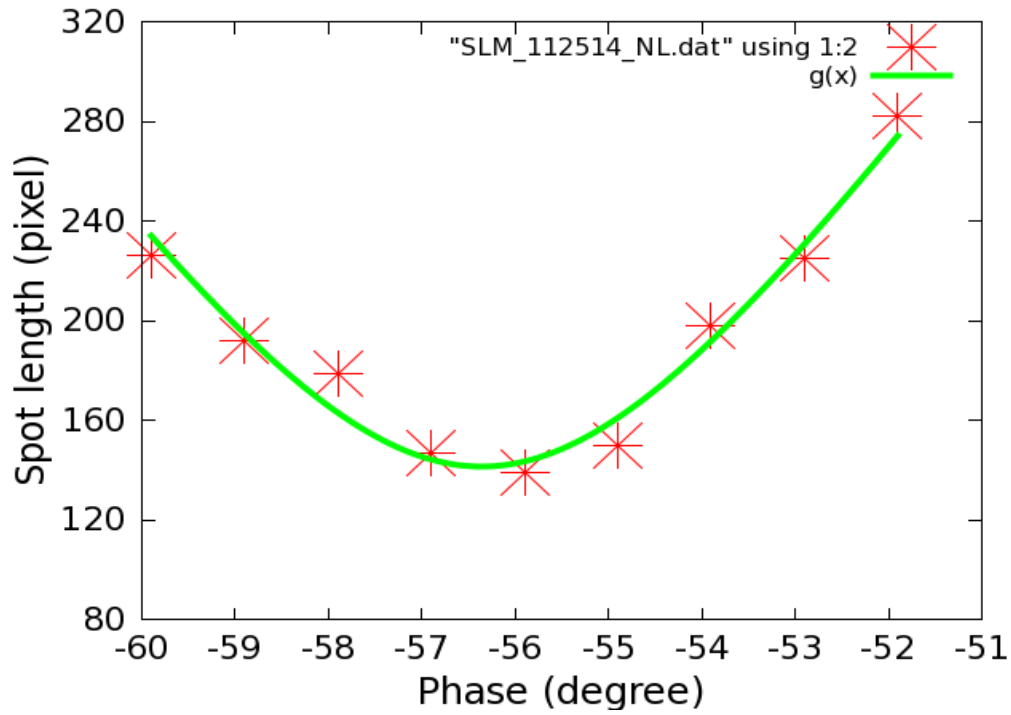


FIG. 54: Hyperbola fitting for Arc1 - head to tail calculation (tune mode).

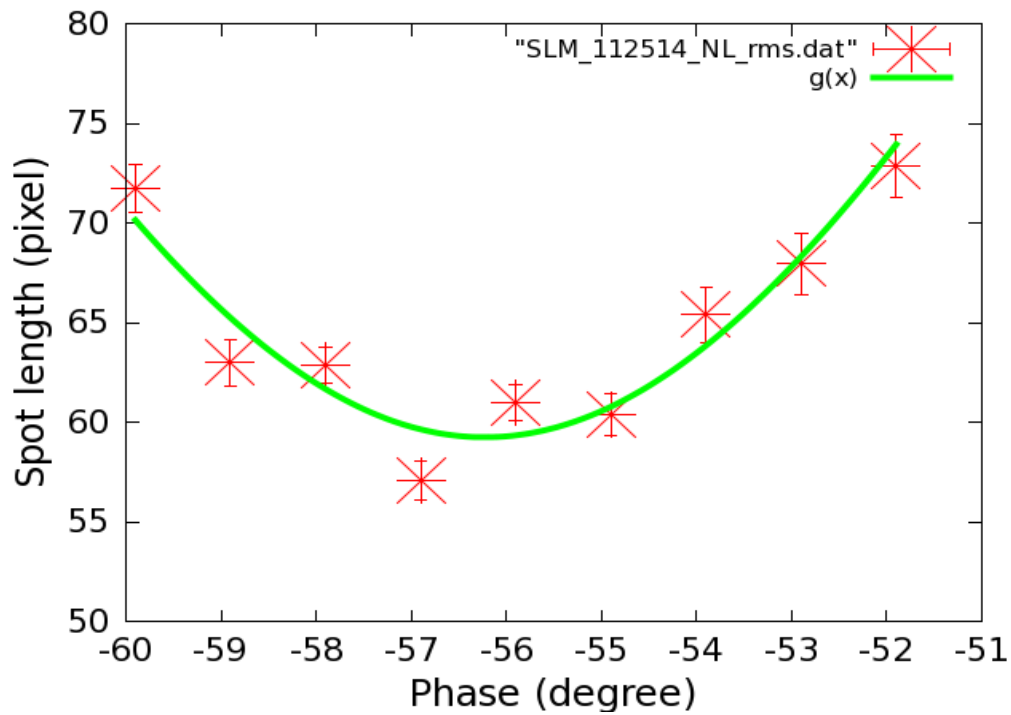


FIG. 55: Hyperbola fitting for Arc1 - rms calculation (tune mode).

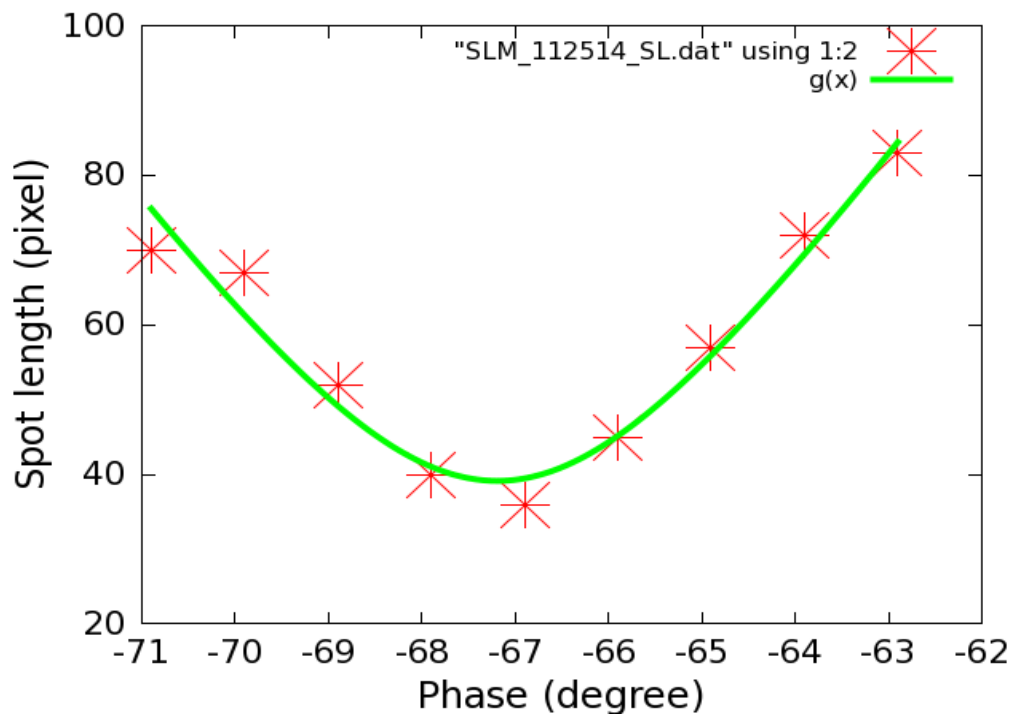


FIG. 56: Hyperbola fitting for Arc2 - head to tail calculation (tune mode).

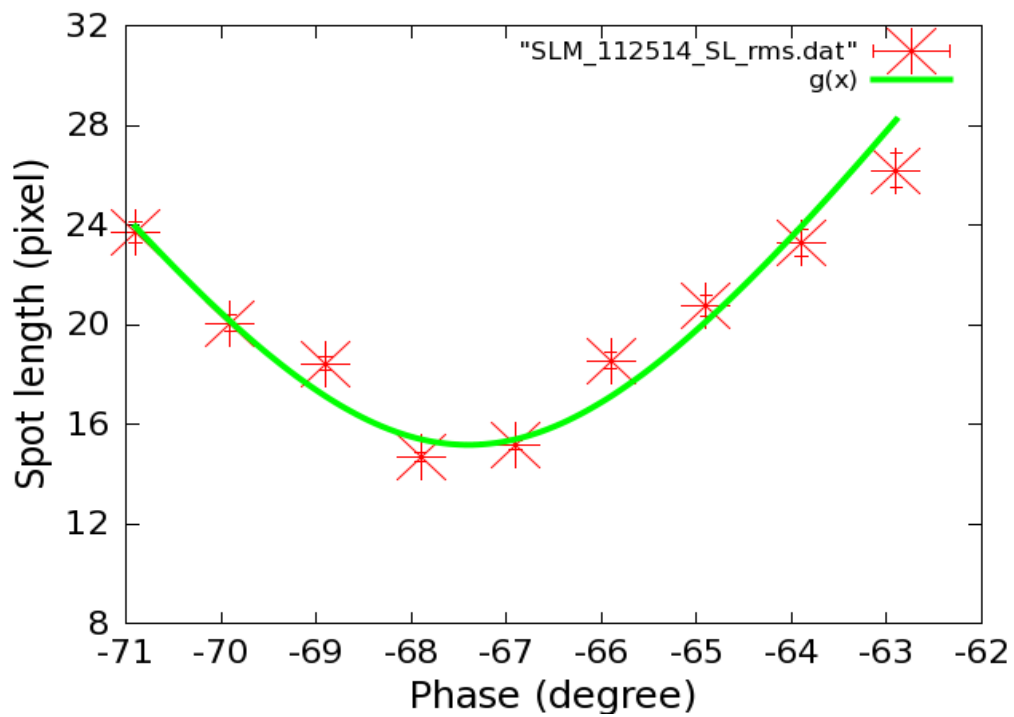


FIG. 57: Hyperbola fitting for Arc2 - rms calculation (tune mode).

The same measurements and calculations are done for Arc2 as shown in Fig. 56 and Fig. 57. Arc1 and Arc2 results were accomplished by using tune mode beam. Using tune mode beam leads to a beam jitter which in turn may overestimate the bunch length. The overestimate came from the fact that the image size may increase during image capture due to the beam jitter which in turn will increase the error bars on the fitting curve. In a later experiment, the bunch is compressed before entering the North linac and the measurements are done again for both arcs. The results for both arcs before and after compression are shown in Table 9.

TABLE 9: Bunch length results

Location	Head to tail(μm)	<i>rms</i>(μm)	<i>rms</i>(μm) - comprssion
Arc1	474.1 ± 20.4	91.4 ± 6.5	46.1 ± 3.5
Arc2	401.2 ± 18.8	112.8 ± 5.8	42.5 ± 5.1

The bunch length shows a good internal agreement, the Arc2 result before compression is greater than Arc1 because the Arc1 M_{56} may not be equal to zero³ which in turn will increase the bunch length.

One year later, the measurements were done again with CW beam and the results are shown in Fig. 58 and Fig. 59. The beam jitter was less than the tune beam mode as expected. The bunch length for Arc1 is $141.2 \pm 4.3 \mu\text{m}$ and for Arc2 is $144.4 \pm 4.7 \mu\text{m}$. The excellent agreement is achieved because CW mode was used and the integration time for the SLM was decreased to prevent the camera saturation. The CW bunch length result is different from the tune mode result because the beam configuration was changed.

³Internal discussion with Michael Tiefenback

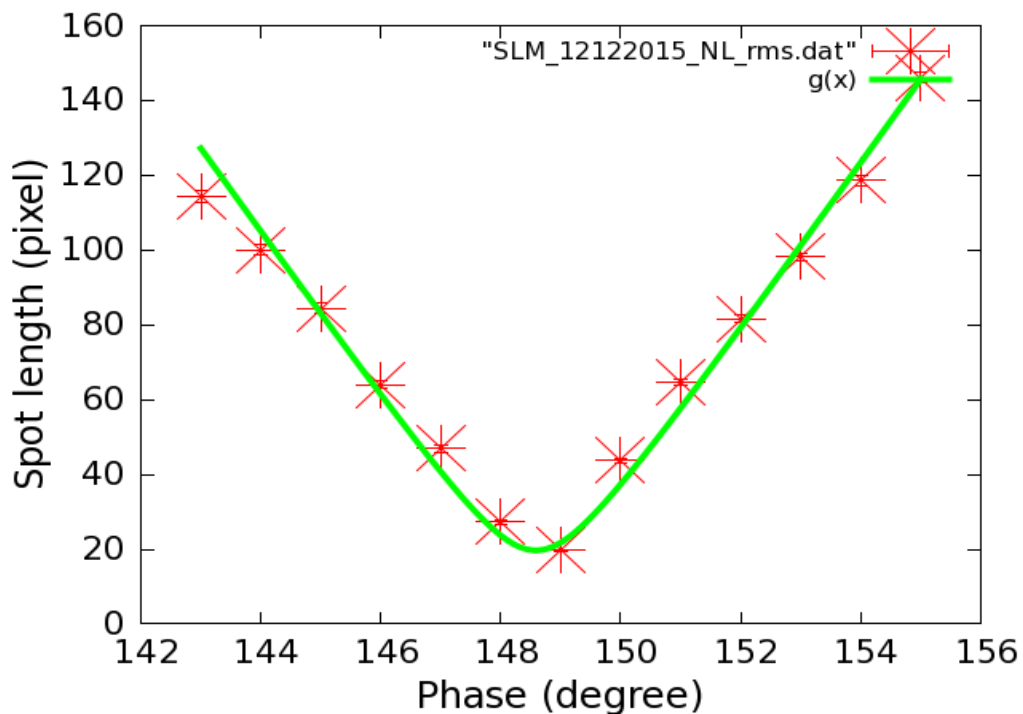


FIG. 58: Hyperbola fitting for Arc1 - *rms* calculation (CW mode).

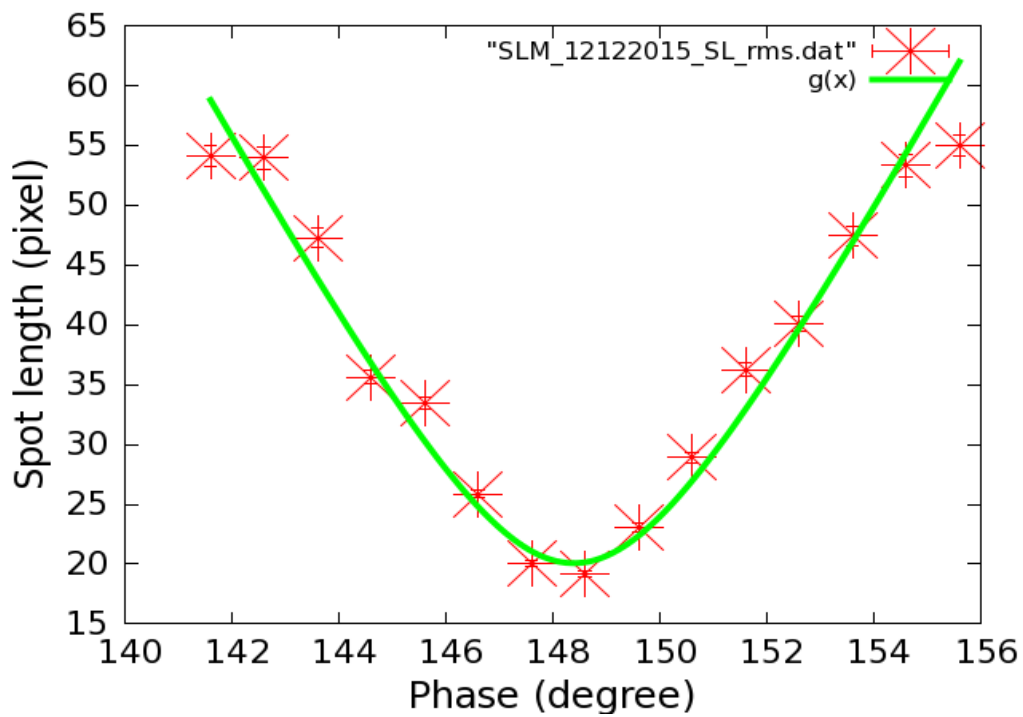


FIG. 59: Hyperbola fitting for Arc2 - *rms* calculation (CW mode).

CHAPTER 7

SUMMARY AND CONCLUSION

In this thesis, the longitudinal beam size (bunch length) at CEBAF is determined by many measurement techniques. The techniques are both invasive and non-invasive. The bunch length depends on the location of the measurements. The bunch length is long in the beginning of the injector line and is compressed to a short bunch length after the injector chicane.

At the beginning of the injector, the bunch length was determined by Brock's cavity and the slit-scan technique. The Brock cavity is a non-invasive technique depending on the resonance with modes of the cavity; the resonance can be expressed as a Fourier series sum. The output signal is the superposition of the Fourier modes. The output signals were used to determine the bunch length. The slit-scan technique is an invasive technique and it works by scanning the electron beam bunch through a small slit by changing the laser phase. The bunch length was determined from the output relation between the phase and the current. The bunch length was determined at different beam currents by both techniques and simulations were used to estimate the bunch length at the two locations. Simulation results showed good agreement with the slit-scan technique. The Brock cavity with a 499 MHz laser overestimated the bunch length at low current because of the cavity band width limitation and measurements made with 249.5 MHz overestimated the bunch length by 10 % at high currents because the transfer function needed more refinement. The Brock cavity is a fast method, provides a calibrated and continuous monitor of the bunch length, but it can not determine small bunches due to its bandwidth limits. The slit-scan method is an accurate method and can determine bunch length to about 40 ps but the disadvantage is that it takes a long time to perform the measurements.

The third measurement technique used in the injector was the back-phasing technique and the measurement was completed in the 4D line. At that location, the bunch was much smaller due to active compression in the injector. The beam energy can reach up to 123 MeV in the measurements. The back-phasing technique is an invasive technique that depends on the fact that the energy spread is at maximum as the bunch is at zero crossing of an RF wave which means that there will be an energy chirp leading to an energy difference between the head and the tail. By deflecting the beam using a dipole and using a wire scanner to

measure the horizontal beam profile for a bunch on crest and at zero crossing of the RF wave, the bunch length was determined. Back-phasing is an effective technique that can determine any change in the bunch length even if there is any deformation in the beam bunch but it takes a long time to complete the measurements and analyze the data to determine the bunch length.

The fourth measurement technique used was a non-invasive technique and works on the basis of interference of synchrotron radiation. In order to establish that technique, a new chamber with four ports was constructed and installed at the end of the CEBAF injector. The chamber was designed and constructed after doing some calculations determining the placement of the mirror that was used to reflect the CSR into the RTI. The experiment was completed after the fourth dipole of the injector chicane because the bunch was fully compressed there. A SR mirror was installed at 455.5 mm away from the middle of the dipole and the CSR was directed to the RTI through an optical line that was installed on a table above the chamber. The RTI consists of wedge splitter, plane mirrors, concave mirror, and a pyro-detector. The signal received by the RTI was chopped by a chopper working at 25 Hz repetition rate.

It was found that the RTI output signal did not yield beam related signals even when the beam current was maximum. A survey was completed about possible effects that can lower the power of the CSR. The survey included the effects of window transmission material, mirror reflectivity, chopper repetition rate, and the polarizer on the CSR power. The survey results showed that the crystal quartz window provided adequate transmission material for the chamber window. The mirror reflectivity decreased the CSR by a small factor that had no effect on the output signal coming from the detector. The chopper repetition rate had no effect on the shape of the output signal but as the frequency increased the detector took more time to give the signal. The polarizer check showed that it did not change the detected signal and the detector did not detect the CSR signal because the background noise was higher than the CSR signal to be detected. The signal level that should be received at the detector channels was calculated and shown in Table 8.

The fifth measurement technique used was to observe the synchrotron light from a dispersed beam. It is an invasive technique that depends on the fact that the energy spread increases when the bunch is not on crest. The measurement was done by changing the gang phase of the North linac (or South linac gang phase in cases using the SLM in Arc2) and determining the spot length at the monitor for each phase. Plotting the spot length versus the phase, doing a hyperbola fit to the plot, and knowing the slope of the fit, the bunch

length was determined. Two SLMs were used, one in Arc1 and the other in Arc2. Both SLM results were consistent with the back-phasing result and in good agreement with each other especially after applying the bunch compression. The SLM is a fast, cost effective technique and presently the only technique in CEBAF to determine the bunch length after compression by the injector chicane.

The calculated and estimated *rms* bunch lengths measured are given in Table 10, the results show a good agreement between the calculated and estimated bunch length. The measured results in the table were calculated for electron beam operating at 499 MHz with 10 μ A of beam current. The expected results were determined from simulations for slit-scan technique and Brock cavity technique. Back-phasing and SLM expected value was known from internal discussions while the SLM compression value was calculated from Eq. (54).

TABLE 10: Bunch length results (*rms* value) summary at all locations

Technique	Location	Beam Energy	Measured	Expected
Brock cavity	A2	130 keV	8.31 ± 0.01 mm	6.8 mm
Slit-scan	Chopper chamber	130 keV	7.16 ± 0.04 mm	7.9 mm
Brock cavity	1D dump	130 keV	10.41 ± 0.04 mm	8.1 mm
Back-phasing	4D dump	102 MeV	80.8 ± 2.0 μ m	100 μ m
SLM1	Arc1	1052 MeV	91.4 ± 6.5 μ m	100 μ m
SLM1(compression)	Arc1	1052 MeV	46.1 ± 3.5 μ m	56 μ m
SLM2	Arc2	2002 MeV	112.8 ± 5.8 μ m	100 μ m
SLM2(compression)	Arc2	2002 MeV	42.5 ± 5.1 μ m	56 μ m

7.0.3 FUTURE WORK

As discussed above, the Brock cavity and SLM worked fine but need a little adjustment while RTI was commissioned but did not observe the desired signal. In this section, ways to overcome these points are discussed.

Bunch length measurements were completed in the injector line using the Brock cavity and slit-scan techniques. The main issue with the Brock cavity was determining the transfer function to correct the received voltage signal. Since the transfer function is determined, it may become easier to make Brock cavity an operational tool. One way to do this is to feed the data directly into a code that can calculate the bunch length. The Brock cavity should be improved as an operation tool which means that any operator can use it without the help

of an expert. Using the Brock cavity as a live bunch length monitor will help in adjusting the beam to the right bunch length.

SLM measurements provide the only technique in CEBAF to determine the bunch length after compression. The SLM is an invasive technique but can be used during the regular operation of CEBAF. Two issues were noticed during the measurements. The first issue was the beam jittering. As the beam jitters the spot size is overestimated and leads to an overestimate in the bunch length. The beam jitter may be because one of the cavities is not phased well, and finding that cavity will minimize the beam jitter. The second issue was the camera saturation which leads to an overestimate to the bunch length. The camera saturation can be eliminated by decreasing the integration time of the camera. To become an operational tool, automating the image processing process needs to be completed. Automating the process should start by capturing the image of the spot at the SLM for different NL gang phases. The results should be fed into the written code (see APPENDIX C) to determine the *rms* beam width. Plotting the *rms* beam width versus the gang phase will give a hyperbolic curve. Automating these steps will make SLM a beneficial tool to determine the bunch length in an easy way.

The RTI experiment did not give the desired signal because the background noise was high. Minimizing the background and filtering the CSR signal will help in achieving a useful monitor. Minimizing the background can be accomplished in the tunnel by shielding the components of the experiment from the infrared radiation coming from the tunnel elements. Another improvement is to put the experiment in a nitrogen gas environment to decrease the infrared absorption by air. A final step that should be done is to calibrate the pyro-detector. This step was not made because of the lack of an infrared source and it is important to demonstrate the sensitivity of the detector to the THz radiation.

Adopting the above recommendations will make bunch length measurements more efficient, more effective, and easier to the operators.

BIBLIOGRAPHY

- [1] R. Kazimi, “Simultaneous four-hall operation for 12 GeV CEBAF,” in *Proceedings of IPAC 2013, Shanghai, China*, p. 3502, 2013.
- [2] T. Nakazato, M. Oyamada, N. Niimura, S. Urasawa, O. Konno, A. Kagaya, R. Kato, T. Kamiyama, Y. Torizuka, and T. Nanba, “Observation of coherent synchrotron radiation,” *Physical Review Letters*, vol. 63, no. 12, pp. 1245–1248, 1989.
- [3] E. B. Blum, U. Happek, and A. J. Sievers, “Observation of coherent synchrotron radiation at the Cornell linac,” *Nuclear Instruments and Methods in Physics Research Section A*, vol. 307, no. 23, pp. 568–576, 1991.
- [4] R. Kato, T. Nakazato, M. Oyamada, S. Urasawa, T. Yamakawa, M. Yoshioka, M. Ikezawa, K. Ishi, T. Kanai, Y. Shibata, and T. Takahashi, “Suppression of coherent synchrotron radiation in conducting boundaries,” in *Proceedings of International Conference on Particle Accelerators*, pp. 1617–1619, 1993.
- [5] J. S. Nodvick and D. S. Saxon, “Suppression of Coherent Radiation by Electrons in a Synchrotron,” *Physical Review*, vol. 96, no. 1, pp. 180–184, 1954.
- [6] V. Yakimenko, M. Fedurin, V. Litvinenko, A. Fedotov, D. Kayran, and P. Muggli, “CSR Shielding Experiment,” *Proceedings of 2011 Particle accelerator conference, New York, USA*, pp. 1677–1679, 2011.
- [7] Y. Shibata, T. Takahashi, T. Kanai, K. Ishi, M. Ikezawa, J. Ohkuma, S. Okuda, and T. Okada, “Diagnostics of an electron beam of a linear accelerator using coherent transition radiation,” *Physical Review E*, vol. 50, no. 2, pp. 1479–1484, 1994.
- [8] D. X. Wang, G. A. Krafft, E. Price, P. A. D. Wood, D. W. Porterfield, and T. W. Crowe, “A noninvasive bunch length monitor for femtosecond electron bunches,” *Applied Physics Letters*, vol. 70, no. 4, p. 529, 1997.
- [9] B. Leissner, C. Berger, R. Siedling, M. Tonutti, M. Geitz, G. Schmidt, and P. Schmuser, “Bunch length measurements using a Martin Puplett interferometer at the TESLA Test Facility linac,” in *Proceedings of the 1999 Particle Accelerator Conference*, vol. 3, pp. 2172–2174.

- [10] M. Geitz, K. Hanke, P. Schmüser, Y. Divin, U. Poppe, V. Pavlovskii, V. Shirotov, O. Volkov, J. Menzel, and M. Tonutti, “A Hilbert transform spectrometer using a high- T_c Josephson junction for bunch length measurements at the TESLA Test Facility linac,” in *Proceedings of the 1999 Particle Accelerator Conference, New York*, pp. 2178–2180, 1999.
- [11] M. Castellano, V. Verzilov, L. Catani, A. Cianchi, G. Orlandi, and M. Geitz, “Measurements of coherent diffraction radiation and its application for bunch length diagnostics in particle accelerators,” *Physical Review E*, vol. 63, no. 5, p. 056501, 2001.
- [12] F. Perez, I. Birkel, E. Huttel, A. Müller, and M. Pont, “Beam size and bunch length measurements at the ANKA storage ring,” *Proceedings of the 2003 Particle Accelerator Conference*, p. 3276, 2003.
- [13] Y. Yamamoto, T. Hori, I. Sakai, K. Yadomi, and H. Iwasaki, “Measurement of the beam bunch length in an electron storage ring using an avalanche photodiode,” *Nuclear Instruments and Methods in Physics Research Section A*, vol. 533, pp. 505–508, 2004.
- [14] P. Evtushenko, J. Coleman, K. Jordan, J. M. Klopff, G. Neil, and G. P. Williams, “Bunch Length Measurements at the JLab FEL Using Coherent Transition and Synchrotron Radiation,” in *AIP Conference Proceedings*, vol. 868, pp. 193–201, 2006.
- [15] C. Kondo, H. Maesaka, Y. Otake, S. Matsubara, T. Matsumoto and S. Inoue, “CSR BUNCH LENGTH MONITOR FOR XFEL/SPRING-8 SACLA,” *Proceedings of IPAC2011*, p. 1224, 2011.
- [16] S. Wesch, B. Schmidt, C. Behrens, H. Delsim-Hashemi, and P. Schmüser, “A multi-channel THz and infrared spectrometer for femtosecond electron bunch diagnostics by single-shot spectroscopy of coherent radiation,” *Nuclear Instruments and Methods in Physics Research Section A*, vol. 665, pp. 40–47, 2011.
- [17] J. Thangaraj, G. Andonian, R. Thurman-Keup, J. Ruan, A. S. Johnson, A. Lumpkin, J. Santucci, T. Maxwell, A. Murokh, M. Ruelas, and A. Ovodenko, “Demonstration of a real-time interferometer as a bunch-length monitor in a high-current electron beam accelerator,” *The Review of Scientific Instruments*, vol. 83, no. 4, p. 043302, 2012.
- [18] I. Nozawa, K. Kan, J. Yang, A. Ogata, T. Kondoh, M. Gohdo, K. Norizawa, H. Kobayashi, H. Shibata, S. Gonda, and Y. Yoshida, “Measurement of < 20 fs bunch

- length using coherent transition radiation,” *Physical Review Special Topics - Accelerators and Beams*, vol. 17, no. 7, p. 072803, 2014.
- [19] B. E. Carlsten, D. W. Feldman, J. M. Kinross-Wright, M. L. Milder, S. J. Russell, J. G. Plato, B. A. Sherwood, M. E. Weber, R. G. Cooper, and R. E. Sturges, “Subpicosecond Compression Experiments at Los Alamos National Laboratory,” in *AIP Conference Proceedings*, vol. 367, pp. 21–35, 1996.
- [20] R. Akre, L. Bentson, P. Emma, and P. Krejcik, “Bunch length measurements using a transverse RF deflecting structure in the SLAC linac,” *Proceedings of EPAC*, p. 1882, 2002.
- [21] K. Sakaue, Y. Nishimura, M. Nishiyama, T. Takahashi, M. Washio, T. Takatomi, and J. Urakawa, “Temporal profile measurement of an electron bunch with the two-cell rf deflecting cavity at Waseda University,” *Japanese Journal of Applied Physics*, vol. 54, no. 2, p. 026301, 2015.
- [22] M. Fitch, A. Melissinos, and P. Colestock, “Picosecond electron bunch length measurement by electro-optic detection of the wakefield,” in *Proceedings of the 1999 Particle Accelerator Conference*, vol. 3, pp. 2181–2183, 1999.
- [23] X. Yan, A. MacLeod, W. Gillespie, G. Knippels, D. Oepts, A. van der Meer, and W. Seidel, “Subpicosecond Electro-optic Measurement of Relativistic Electron Pulses,” *Physical Review Letters*, vol. 85, no. 16, pp. 3404–3407, 2000.
- [24] G. Berden, W. Gillespie, S. Jamison, E.-A. Knabbe, A. MacLeod, A. van der Meer, P. Phillips, H. Schlarb, B. Schmidt, P. Schmüser, and B. Steffen, “Benchmarking of Electro-Optic Monitors for Femtosecond Electron Bunches,” *Physical Review Letters*, vol. 99, no. 16, p. 164801, 2007.
- [25] D. Wang, G. Krafft, and C. Sinclair, “Measurement of femtosecond electron bunches using a rf zero-phasing method,” *Physical Review E*, vol. 57, no. 2, pp. 2283–2286, 1998.
- [26] M. Ayzatsky, E. Biller, A. Dovbnaya, I. Khodak, V. Kushnir, V. Mitrochenko, A. Opanasenko, S. Perezhogin, D. Stepin, and L. Zavada, “Bunch-length monitor for an electron linac,” in *Proceedings of the 2001 Particle Accelerator Conference*, vol. 3, pp. 2356–2358, 2001.

- [27] S. E. Korbly, A. S. Kesar, R. J. Temkin, and J. H. Brownell, "Measurement of subpicosecond bunch lengths using coherent Smith-Purcell radiation," *Physical Review Special Topics - Accelerators and Beams*, vol. 9, no. 2, p. 022802, 2006.
- [28] A. H. Lumpkin, "Time-domain diagnostics in the picosecond regime," in *AIP Conference Proceedings*, vol. 367, pp. 327–340, AIP, 1996.
- [29] A. Takahashi, M. Nishizawa, Y. Inagaki, M. Koishi, and K. Kinoshita, "A new femtosecond streak camera," in *SPIE's 1993 International Symposium on Optics, Imaging, and Instrumentation*, pp. 22–30, 1993.
- [30] M. Geitz, "Bunch length measurements," *Proceedings of DIPAC*, pp. 19–23, 1999.
- [31] K. Wille, *The Physics of Particle Accelerators - An Introduction*. Oxford University Press, 1st ed., 2000.
- [32] H. Wiedemann, *Particle Accelerator Physics*. Springer, 3rd ed., 2007.
- [33] A. Chao and M. Tigner, *Handbook of Accelerator Physics and Engineering*. World Scientific, 3rd printing ed., 2006.
- [34] D. Jackson, *Classical Electrodynamics*. John Wiley & Sons, Inc., 3rd ed., 1998.
- [35] M. F. Kimmit, *Far Infrared Techniques*. Pion Limited, 1970.
- [36] R. A. Smith, F. E. Jones, and R. P. Chasmar, *The Detection and Measurement of Infra-red Radiation*. Clarendon Press, 1968.
- [37] P. Emma, H. Loos, and C. Behrens, "Fast, absolute bunch length measurements in a linac using an improved RF-phasing method," in *Proceedings of FEL 2012, Nara, Japan*, p. 602, 2012.
- [38] J. Denard, "Beam current monitors," *CERN-2009-005*, p. 141, 2009.
- [39] J. Hansknecht and M. Poelker, "Synchronous photoinjection using a frequency-doubled gain-switched fiber-coupled seed laser and ErYb-doped fiber amplifier," *Physical Review Special Topics - Accelerators and Beams*, vol. 9, p. 063501, 2006.
- [40] K. Halbach and R. F. Holsinger, "Superfish - a computer program for evaluation of RF cavities with cylindrical symmetry," *Particle Accelerator*, no. 7, p. 213, 1976.

- [41] B. Roberts, R. R. Mammei, M. Poelker, and J. L. McCarter, “Compact noninvasive electron bunch-length monitor,” *Physical Review Special Topics - Accelerators and Beams*, vol. 15, p. 122802, 2012.
- [42] G. Geloni, V. Kocharyan, E. Saldin, E. Schneidmiller, and M. Yurkov, “Theory of edge radiation,” *DESY 08-118*, 2008.
- [43] O. Chubar, P. Elleaume, and A. Snigirev, “Phase analysis and focusing of synchrotron radiation,” *Nuclear Instruments and Methods in Physics Research Section A: Accelerators, Spectrometers, Detectors and Associated Equipment*, vol. 435, no. 3, pp. 495–508, 1999.
- [44] WaveMetrics, “Igor Pro - Technical graphing and data analysis.”
- [45] M. Naftaly and R. Dudley, “Terahertz reflectivities of metal-coated mirrors.,” *Applied optics*, vol. 50, no. 19, pp. 3201–4, 2011.
- [46] Mathworks.com, “MATLAB.”
- [47] M. Borland, “Elegant: A exible SDDS-compliant code for accelerator simulation. ANL Pub. LS-287,” 2000.

APPENDIX A

SIGNAL PROCESSING

A.1 WIENER-KHINCHIN THEOREM

The spectral power density is the Fourier transform of the autocorrelation

A.1.1 PROOF

Let $E(t)$ be a random function with autocorrelation function $C(\tau)$

$$C(\tau) = \int_{-\infty}^{\infty} \overline{E}(t)E(t + \tau)dt, \quad (119)$$

where t is the time and τ is the time lag. The Fourier inversion theorem gives

$$E(t + \tau) = \int_{-\infty}^{\infty} E_{\nu}e^{-2\pi i\nu(t+\tau)}d\nu, \quad (120)$$

$$\overline{E}(t) = \int_{-\infty}^{\infty} \overline{E}_{\nu'}e^{2\pi i\nu't}d\nu'. \quad (121)$$

Plugging $\overline{E}(t)$ and $E(t + \tau)$ into Eq. (119)

$$C(\tau) = \int_{-\infty}^{\infty} \left[\int_{-\infty}^{\infty} \overline{E}_{\nu'}e^{2\pi i\nu't}d\nu' \right] \left[\int_{-\infty}^{\infty} E_{\nu}e^{-2\pi i\nu(t+\tau)}d\nu \right] dt, \quad (122)$$

$$C(\tau) = \int_{-\infty}^{\infty} \int_{-\infty}^{\infty} \int_{-\infty}^{\infty} \overline{E}_{\nu'}E_{\nu}e^{2\pi i(\nu'-\nu)t}e^{-2\pi i\nu\tau}d\nu d\nu' dt. \quad (123)$$

Since Dirac delta function satisfies $\delta(\nu' - \nu) = \int_{-\infty}^{\infty} e^{2\pi i(\nu'-\nu)t}dt$ then

$$C(\tau) = \int_{-\infty}^{\infty} \int_{-\infty}^{\infty} \overline{E}_{\nu'}E_{\nu}\delta(\nu' - \nu)e^{-2\pi i\nu\tau}d\nu d\nu' = \int_{-\infty}^{\infty} \overline{E}_{\nu'}E_{\nu}e^{-2\pi i\nu\tau}d\nu, \quad (124)$$

$$C(\tau) = \int_{-\infty}^{\infty} |E_{\nu}|^2 e^{-2\pi i\nu\tau}d\nu. \quad (125)$$

The autocorrelation is the Fourier transform of the absolute square of E_{ν} .

A.2 CONVOLUTION THEOREM

In digital signal processing, the Fourier transform properties of a signal are used to modify a signal by adding, subtracting, multiplying, or dividing by a filtering function. The convolution of two functions $f(\nu)$ and $g(\nu)$ is a new function $h(\nu)$ and is defined as

$$(f * g)(\nu) = \int_{-\infty}^{\infty} g(\nu - t)f(t)dt = h(\nu).$$

The convolution theorem states that the Fourier transform of a convolution of two functions is the product of their individual Fourier transform.

$$F[(g * f)](\nu) = F[g(\nu)]F[f(\nu)] = F[h(\nu)].$$

A.2.1 PROOF

Assuming two functions $f(t)$ and $g(t)$ have Fourier transforms $g(\nu)$ and $f(\nu)$, then the Fourier product is

$$F[g(\nu)]F[f(\nu)] = \int_{-\infty}^{\infty} e^{-2\pi i\nu t}g(t)dt \int_{-\infty}^{\infty} e^{-2\pi i\nu t'}f(t')dt', \quad (126)$$

$$F[g(\nu)]F[f(\nu)] = \int_{-\infty}^{\infty} \int_{-\infty}^{\infty} e^{-2\pi i\nu(t+t')}g(t)f(t')dtdt'. \quad (127)$$

Let $u = t + t'$, by changing the variables and using Fubini's theorem

$$F[g(\nu)]F[f(\nu)] = \int_{-\infty}^{\infty} \int_{-\infty}^{\infty} e^{-2\pi i\nu u}g(u - t')f(t')dudt', \quad (128)$$

$$F[g(\nu)]F[f(\nu)] = \int_{-\infty}^{\infty} e^{-2\pi i\nu u} \left[\int_{-\infty}^{\infty} g(u - t')f(t')dt' \right] du. \quad (129)$$

Let $h(u) = \int_{-\infty}^{\infty} g(u - t')f(t')dt'$

$$F[g(\nu)]F[f(\nu)] = \int_{-\infty}^{\infty} e^{-2\pi i\nu u}h(u)du = F[h(\nu)]. \quad (130)$$

APPENDIX B

BEAM DYNAMICS

B.1 TILTED ELLIPSE

The parameters for the description of the tilted ellipse in Fig. 60 may be obtained as follows. By substituting Eq. (30) into Eq. (29) and rearrange the parameters, one obtains

$$x^2 + \left(\alpha^2 x^2 + 2\alpha\beta x x' + \beta^2 x'^2 \right) = \epsilon\beta, \quad (131)$$

$$x^2 + \left(\alpha x + \beta x' \right)^2 = \epsilon\beta. \quad (132)$$

Substituting $x' = sx = -\alpha x/\beta$ in Eq. (132), then

$$x_{max} = \pm \sqrt{\beta\epsilon}. \quad (133)$$

Substituting x_{max} in Eq. (132) to determine the corresponding x' , then

$$x' = -\alpha \frac{x_{max}}{\beta}. \quad (134)$$

Therefore

$$(x_{max}, x') = \left(\sqrt{\beta\epsilon}, -\alpha \sqrt{\frac{\epsilon}{\beta}} \right). \quad (135)$$

Differentiating Eq. (132) with respect to x , one obtains

$$2x + 2\alpha(\beta x' + \alpha x) = 0. \quad (136)$$

To find x'_{max} , x' must equal zero in Eq. (136), then

$$(\beta x' + \alpha x) = \frac{-x}{\alpha}. \quad (137)$$

Substituting from Eq. (137) into Eq. (132)

$$\frac{x^2}{\alpha^2}(\alpha^2 + 1) = \beta\epsilon. \quad (138)$$

From Eq. (30)

$$x = \pm \alpha \sqrt{\frac{\epsilon}{\gamma}}. \quad (139)$$

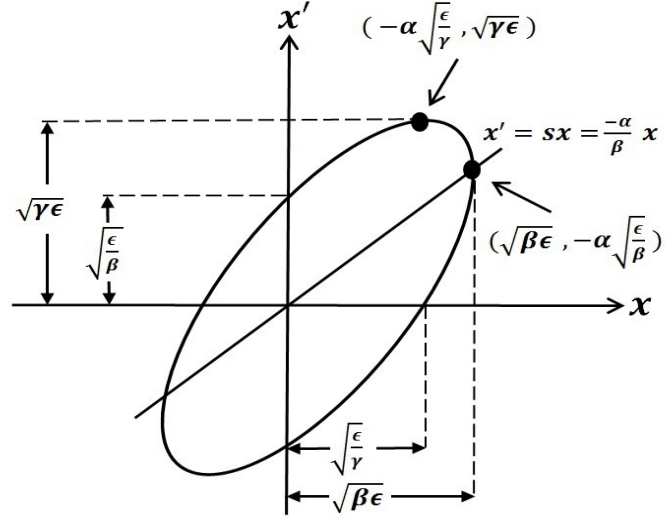


FIG. 60: Phase space

The corresponding x' is found by substituting Eq. (139) into Eq. (132)

$$\alpha^2 \frac{\epsilon}{\gamma} + (\beta x' - \alpha^2 \sqrt{\frac{\epsilon}{\gamma}})^2 = \beta \epsilon, \quad (140)$$

$$(\beta x' - \alpha^2 \sqrt{\frac{\epsilon}{\gamma}})^2 = \beta \epsilon - \frac{\alpha^2 \epsilon}{\gamma} = \frac{\epsilon}{\gamma} (\beta \gamma - \alpha^2) = \frac{\epsilon}{\gamma}, \quad (141)$$

$$\beta x' - \alpha^2 \sqrt{\frac{\epsilon}{\gamma}} = \sqrt{\frac{\epsilon}{\gamma}}, \quad (142)$$

$$\beta x' = \sqrt{\frac{\epsilon}{\gamma}} (1 + \alpha^2) = \sqrt{\frac{\epsilon}{\gamma}} \beta \gamma, \quad (143)$$

$$x'_{max} = \sqrt{\epsilon \gamma}. \quad (144)$$

Therefore

$$(x, x'_{max}) = (-\alpha \sqrt{\frac{\epsilon}{\gamma}}, \sqrt{\epsilon \gamma}). \quad (145)$$

Next, the intercepts with the phase space axes are found by putting $x = 0$ into Eq. (132) which yields

$$(\beta x'_{max})^2 = \beta \epsilon, \quad (146)$$

$$x' = \pm \sqrt{\frac{\epsilon}{\beta}}. \quad (147)$$

Therefore

$$(x, x') = (0, \pm \sqrt{\frac{\epsilon}{\beta}}). \quad (148)$$

Putting $x' = 0$ into Eq. (132) yields

$$x^2 + \alpha^2 x^2 = \beta\epsilon, \quad (149)$$

$$x^2(1 + \alpha^2) = \beta\epsilon, \quad (150)$$

$$x = \pm \sqrt{\frac{\epsilon}{\gamma}}. \quad (151)$$

Therefore

$$(x, x') = (\pm \sqrt{\frac{\epsilon}{\gamma}}, 0). \quad (152)$$

B.2 M_{56} FOR KINEMATIC COMPRESSION

Assume an electron with a velocity $v = \beta c$ and relativistic momentum $P = \beta\gamma mc$ goes through a length L , where m is the electron mass and c is the speed of light. After a period of time (T), the distance between the particle and the reference particle changes by ΔL given by

$$\Delta L = \Delta v T. \quad (153)$$

Since the momentum can be written as $P = mc\beta(1 - \beta^2)^{-\frac{1}{2}}$ then

$$\Delta P = mc[(1 - \beta^2)^{-\frac{1}{2}} + \beta^2(1 - \beta^2)^{-\frac{3}{2}}] \Delta\beta, \quad (154)$$

$$\Delta P = mc(1 - \beta^2)^{-\frac{3}{2}} \Delta\beta = mc\gamma^3 \Delta\beta, \quad (155)$$

$$\frac{\Delta P}{P} = \frac{mc\gamma^3 \Delta\beta}{mc\gamma\beta} = \gamma^2 \frac{\Delta v}{v}, \quad (156)$$

$$\Delta v = \frac{v}{\gamma^2} \frac{\Delta P}{P}. \quad (157)$$

Substituting from Eq. (157) into Eq. (153)

$$\Delta L = \frac{vT}{\gamma^2} \frac{\Delta P}{P} = \frac{L}{\gamma^2} \frac{\Delta P}{P}. \quad (158)$$

Since the distance change can be written as $\Delta L = M_{56} \Delta P/P$, then

$$M_{56} = \frac{L}{\gamma^2}. \quad (159)$$

This means that when the particle is not moving with a relativistic velocity and there is a difference in the particle energy within the beam bunch, longitudinal motion is possible. The M_{56} is a function of the distance (L) and γ^2 .

APPENDIX C

COMPUTER CODES USED

C.1 MATLAB CODE

This matlab code is used for image processing the SLM data. It starts by reading the image and then changes the image into a portable gray map 'pgm' file ('pgm' is a data matrix whose values represent shades of gray). The 'pgm' image is written as a matrix then the frame and the background are removed. After removing the background, a horizontal projection is applied to the matrix, then a Gaussian fitting is done to the output file and the *rms* value for the fitting is determined. These previous steps are done for all the images in a for loop.

```
clear
for i=1:13
    % Write formatted data to an output string
    Name = sprintf('15022606_%d.png', i);
    %Read the image in MATLAB enviroment
    N{i}=imread(Name);
    %Image are written into pgm files
    imwrite(N{i}, sprintf('15022606_%d.pgm', i));
    Name = sprintf('15022606_%d.pgm', i);
    M{i}=imread(Name);
    % Eliminate the image frame
    MM{i}=M{i}(40:485,10:660);
    %Change the image into double precision
    MMM{i}=double(MM{i});
    %Do the horizontal projection to the image matrix
    proj{i}=sum(MM{i});
    n=size(proj{i},2);
end
%Read and write the image back ground into pgm file
```

```
b1=imread('15022606_0.png');
imwrite(b1,'b2.pgm');
back=imread('b2.pgm');
back2=back(40:485,10:660);
back3=double(back2);
for i=1:13
    %Subtract the back ground from the image
    new{i}=MM{ i}-back3;
    New{i}=sum(new{i});
    %Do A Gaussian fitting to the horizontal projection
    and determine the rms value
    i
    F=fit((1:n)',New{i}(1:n)', 'gauss1')
    figure;
    %Plot the projection with the Gaussian fitting
    plot(New{i});
    hold on
    plot(F)
    xlabel('Pixel number');
    ylabel('Pixel intensity');
    title(sprintf('15022606_%d.pgm',i));
end
```

C.2 ELEGANT

ELEGANT (Electron Generation ANd Tracking) [47] is a 6D accelerator simulation code that generates particle distributions and tracks them. ELEGANT is an open source code and it has many capabilities such as tracking transport lines, computing Twiss parameters, computing matrix elements, optimization of result, etc.

C.2.1 ELEGANT: INJ.LTE

The following lines describes the lattice of the injector beam line and it includes all the components of the injector beam line from viewer (ITV0L01) to the last dipole of the injector chicane (MBL0R04).

```

D0: DRIF,L=0.305322
ITV0L01: MONI
D1: DRIF,L=0.224795
MBH0L01H: HKICK,L=0
MBH0L01V: VKICK,L=0
D2: DRIF,L=0.294893
IPM0L01: MONI
D3: DRIF
MQS0L01: KQUAD,L=0.08,TILT=-0.7853981633974479,&
SYNCHRAD=1,ISR=1
D4: DRIF,L=0.1068
MQJ0L01: KQUAD,L=0.15,SYNCHRAD=1,ISR=1
D5: DRIF,L=1.205
MHE0L01V: VKICK,L=0
D6: DRIF,L=0.6788
MQS0L01A: KQUAD,L=0.08,TILT=-0.7853981633974479,&
SYNCHRAD=1,ISR=1
D7: DRIF,L=0.0743
MHB0L01AH: HKICK,L=0
MHB0L01AV: VKICK,L=0
D8: DRIF,L=0.8521
ITV0L02: MONI
MQJ0L02: KQUAD,L=0.15,K1=-5.21518055805346,&

```

SYNCHRAD=1,ISR=1
D9: DRIF,L=0.191895
IPM0L02: MONI
MQS0L02: KQUAD,L=0.08,TILT=-0.7853981633974479,&
SYNCHRAD=1,ISR=1
D10: DRIF,L=0.132852
MBH0L02H: HKICK,L=0
MBH0L02V: VKICK,L=0
D11: DRIF,L=0.055058600000000001
MQJ0L02A: KQUAD,L=0.15,K1=5.187823235328593,&
SYNCHRAD=1,ISR=1
D12: DRIF,L=0.68500000000000001
MHE0L02H: HKICK,L=0
D13: DRIF,L=1.31101
MHB0L02AH: HKICK,L=0
MHB0L02AV: VKICK,L=0
D14: DRIF,L=1.04199
MQS0L02B: KQUAD,L=0.08,TILT=-0.7853981633974479,&
SYNCHRAD=1,ISR=1
D15: DRIF,L=0.08699999999999999
MHB0L02BH: HKICK,L=0
MHB0L02BV: VKICK,L=0
D16: DRIF,L=1.02
MHE0L03V: VKICK,L=0
D17: DRIF,L=0.103515
ITV0L03: MONI
D18: DRIF,L=0.036485
MHE0L03H: HKICK,L=0
D19: DRIF,L=0.18831
MBH0L03H: HKICK,L=0
MBH0L03V: VKICK,L=0
D20: DRIF,L=0.48169
MQJ0L03A: KQUAD,L=0.15,SYNCHRAD=1,ISR=1
D21: DRIF,L=0.15

```

IPM0L03: MONI
MQS0L03: KQUAD,L=0.08,TILT=-0.7853981633974479,&
SYNCHRAD=1,ISR=1
D22: DRIF,L=0.255
MQJ0L03: KQUAD,L=0.15,K1=-2.30105587616528,&
SYNCHRAD=1,ISR=1
D23: DRIF,L=0.2
IHA0L03: MONI
D24: DRIF,L=2.09452
ITV0L04: MONI
MHB0L04H: HKICK,L=0
MHB0L04V: VKICK,L=0
IPM0L04: MONI
MQS0L04: KQUAD,L=0.08,TILT=-0.7853981633974479,&
SYNCHRAD=1,ISR=1
D25: DRIF,L=0.106797
MQJ0L04: KQUAD,L=0.15,K1=0.1469440194475174,&
SYNCHRAD=1,ISR=1
D26: DRIF,L=1.3091
R031: RFCA,L=0.5,VOLT=3500000,PHASE=90,&
FREQ=1496999790,CHANGE_P0=1,&
  END1_FOCUS=1,END2_FOCUS=1,BODY_FOCUS_MODEL="SRS"
D27: DRIF,L=0.249995
R032: RFCA,L=0.5,VOLT=3500000,PHASE=90,&
FREQ=1496999790,CHANGE_P0=1,&
  END1_FOCUS=1,END2_FOCUS=1,BODY_FOCUS_MODEL="SRS"
D28: DRIF,L=0.6605960000000001
R033: RFCA,L=0.5,VOLT=3500000,PHASE=90,&
FREQ=1496999790,CHANGE_P0=1,&
  END1_FOCUS=1,END2_FOCUS=1,BODY_FOCUS_MODEL="SRS"
R034: RFCA,L=0.5,VOLT=3500000,PHASE=90,&
FREQ=1496999790,CHANGE_P0=1,&
  END1_FOCUS=1,END2_FOCUS=1,BODY_FOCUS_MODEL="SRS"
R035: RFCA,L=0.5,VOLT=2121490,PHASE=90,&

```

```

FREQ=1496999790,CHANGE_P0=1,&
  END1.FOCUS=1,END2.FOCUS=1,BODY.FOCUS_MODEL="SRS"
R036: RFCA,L=0.5,VOLT=2121490,PHASE=90,&
FREQ=1496999790,CHANGE_P0=1,&
  END1.FOCUS=1,END2.FOCUS=1,BODY.FOCUS_MODEL="SRS"
R037: RFCA,L=0.5,VOLT=2121490,PHASE=90,&
FREQ=1496999790,CHANGE_P0=1,&
  END1.FOCUS=1,END2.FOCUS=1,BODY.FOCUS_MODEL="SRS"
R038: RFCA,L=0.5,VOLT=2121490,PHASE=90,&
FREQ=1496999790,CHANGE_P0=1,&
  END1.FOCUS=1,END2.FOCUS=1,BODY.FOCUS_MODEL="SRS"
D29: DRIF,L=0.653563
ITV0L05: MONI
D30: DRIF,L=0.119375
MAT0L05H: HKICK,L=0
D31: DRIF,L=0.219712
MAT0L05V: VKICK,L=0
D32: DRIF,L=0.193804
IPM0L05: MONI
MQS0L05: KQUAD,L=0.08,TILT=-0.7853981633974479,&
SYNCHRAD=1,ISR=1
D33: DRIF,L=0.092645999999999999
MQJ0L05: KQUAD,L=0.15,K1=-0.8779322912802214,&
SYNCHRAD=1,ISR=1
D34: DRIF,L=0.7534850000000001
R041: RFCA,L=0.7000000000000001,VOLT=11776752.5,PHASE=90,&
FREQ=1496999790,&
  CHANGE_P0=1,END1.FOCUS=1,END2.FOCUS=1,BODY.FOCUS_MODEL="SRS"
D35: DRIF,L=0.299
R042: RFCA,L=0.7000000000000001,VOLT=11776752.5,PHASE=90,&
FREQ=1496999790,&
  CHANGE_P0=1,END1.FOCUS=1,END2.FOCUS=1,BODY.FOCUS_MODEL="SRS"
R043: RFCA,L=0.7000000000000001,VOLT=11776752.5,PHASE=90,&
FREQ=1496999790,&

```

```
CHANGE_P0=1,END1_FOCUS=1,END2_FOCUS=1,BODY_FOCUS_MODEL="SRS"  
R044: RFCA,L=0.7000000000000001,VOLT=11776752.5,PHASE=90, &  
FREQ=1496999790,&  
  CHANGE_P0=1,END1_FOCUS=1,END2_FOCUS=1,BODY_FOCUS_MODEL="SRS"  
R045: RFCA,L=0.7000000000000001,VOLT=11776752.5,PHASE=90, &  
FREQ=1496999790,&  
  CHANGE_P0=1,END1_FOCUS=1,END2_FOCUS=1,BODY_FOCUS_MODEL="SRS"  
R046: RFCA,L=0.7000000000000001,VOLT=11776752.5,PHASE=90, &  
FREQ=1496999790,&  
  CHANGE_P0=1,END1_FOCUS=1,END2_FOCUS=1,BODY_FOCUS_MODEL="SRS"  
R047: RFCA,L=0.7000000000000001,VOLT=11776752.5,PHASE=90, &  
FREQ=1496999790,&  
  CHANGE_P0=1,END1_FOCUS=1,END2_FOCUS=1,BODY_FOCUS_MODEL="SRS"  
R048: RFCA,L=0.7000000000000001,VOLT=11776752.5,PHASE=90, &  
FREQ=1496999790,&  
  CHANGE_P0=1,END1_FOCUS=1,END2_FOCUS=1,BODY_FOCUS_MODEL="SRS"  
D36: DRIF,L=0.784357  
IPM0L06: MONI  
D37: DRIF,L=0.042672  
MDB0L06H: HKICK,L=0  
MDJ0L06V: VKICK,L=0  
D38: DRIF,L=0.176456  
MQD0L06: KQUAD,L=0.15,K1=-3.420718081442382,SYNCH_RAD=1,ISR=1  
D39: DRIF,L=0.8497609  
MBF0L06: DRIF,L=0.13596722678  
IPM0L07: MONI  
D40: DRIF,L=0.056896  
MDB0L07H: HKICK,L=0  
MDJ0L07V: VKICK,L=0  
D41: DRIF,L=0.162236  
MQB0L07: KQUAD,L=0.15,K1=8.743110805303758,SYNCH_RAD=1,ISR=1  
D42: DRIF,L=0.122612  
IHA0L07: MONI  
D43: DRIF,L=0.438472
```

ITV0L08: MONI
D44: DRIF, L=0.138684
IPM0L08: MONI
MDB0L08H: HKICK, L=0
MDJ0L08V: VKICK, L=0
MQB0L08: KQUAD, L=0.15, K1=-6.130387625341791, SYNCH_RAD=1, ISR=1
IHA0L08: MONI
D45: DRIF, L=0.577056
IPM0L09: MONI
MDB0L09H: HKICK, L=0
MDJ0L09V: VKICK, L=0
MQB0L09: KQUAD, L=0.15, K1=7.404139807530224, SYNCH_RAD=1, ISR=1
IHA0L09: MONI
ITV0L10: MONI
IPM0L10: MONI
MDB0L10H: HKICK, L=0
MDJ0L10V: VKICK, L=0
MQB0L10: KQUAD, L=0.15, K1=-1.214785296151175, SYNCH_RAD=1, ISR=1
IHA0L10: MONI
D46: DRIF, L=0.331948
MBL0R01: CSBEND, L=0.3, ANGLE=-0.09599312921857681, &
E2=-0.09599310885968811, N_KICKS=20, USE_RAD_DIST=1
D47: DRIF, L=2.9015377
MAT0R01H: HKICK, L=0
D48: DRIF, L=0.21971
MAT0R01V: VKICK, L=0
D49: DRIF, L=0.206248
IPM0R01: MONI
D50: DRIF, L=0.17265
MQD0R01: KQUAD, L=0.15, K1=-2.856389158742014, SYNCH_RAD=1, ISR=1
D51: DRIF, L=2.086392
MAT0R02H: HKICK, L=0
MAT0R02V: VKICK, L=0
IPM0R02: MONI

MQD0R02: KQUAD,L=0.15,K1=1.829890513253045,SYNCH_RAD=1,ISR=1
D52: DRIF,L=3.685
MBL0R02: CSBEND,L=0.3,ANGLE=0.09599312921857681,&
E1=0.09599310885968811,N_KICKS=20,USE_RAD_DIST=1
ISR0R02: MONI
D53: DRIF,L=4.936499
MAT0R03H: HKICK,L=0
MAT0R03V: VKICK,L=0
IPM0R03: MONI
MQD0R03: KQUAD,L=0.15,K1=-1.471968075392503,SYNCH_RAD=1,ISR=1
MAT0R04H: HKICK,L=0
MAT0R04V: VKICK,L=0
IPM0R04: MONI
MQD0R04: KQUAD,L=0.15,K1=1.957458200454235,SYNCH_RAD=1,ISR=1
D54: DRIF,L=4.730569
IHA0R05: MONI
D55: DRIF,L=0.20593
MAT0R05H: HKICK,L=0
MAT0R05V: VKICK,L=0
IPM0R05: MONI
MQD0R05: KQUAD,L=0.15,K1=-1.396770447598435,SYNCH_RAD=1,ISR=1
D56: DRIF,L=0.13566
ITV0R05: MONI
D57: DRIF,L=1.3181
BSM0R05V: VKICK,L=0
D58: DRIF,L=0.0127
BSM0R05H: HKICK,L=0
D59: DRIF,L=3.470039
MAT0R06H: HKICK,L=0
MAT0R06V: VKICK,L=0
IPM0R06: MONI
MQD0R06: KQUAD,L=0.15,K1=1.957458200454235,SYNCH_RAD=1,ISR=1
MAT0R07H: HKICK,L=0
MAT0R07V: VKICK,L=0

```

IPM0R07: MONI
MQD0R07: KQUAD,L=0.15,K1=-1.471968075392503,SYNCH_RAD=1,ISR=1
D60: DRIF,L=5.535107000000001
MBL0R03: CSBEND,L=0.3,ANGLE=0.09599312921857681,&
E2=0.09599310885968811,N_KICKS=20,USE_RAD_DIST=1
D61: DRIF,L=3.086392
MAT0R08H: HKICK,L=0
MAT0R08V: VKICK,L=0
IPM0R08: MONI
MQD0R08: KQUAD,L=0.15,K1=1.829890513253045,SYNCH_RAD=1,ISR=1
D62: DRIF,L=0.53144
IDA0R08: MONI
D63: DRIF,L=0.42872
SBC0R08: MONI
D64: DRIF,L=0.40193
IBC0R08: MONI
D65: DRIF,L=0.724302
MAT0R09H: HKICK,L=0
MAT0R09V: VKICK,L=0
IPM0R09: MONI
MQD0R09: KQUAD,L=0.15,K1=-2.856389158742014,SYNCH_RAD=1,ISR=1
D66: DRIF,L=1.5696
BSM0R09V: VKICK,L=0
D67: DRIF,L=0.006350000000000001
BSM0R09H: HKICK,L=0
D68: DRIF,L=1.9241957
MBL0R04: CSBEND,L=0.3,ANGLE=-0.09599312921857681,&
E1=-0.09599310885968811,N_KICKS=20,USE_RAD_DIST=1
MKMATCHM56: MARK &
           , FITPOINT=1
MKMATCHDSP: MARK &
           , FITPOINT=1
INJ: LINE=(D0,ITV0L01,D1,MBH0L01H,MBH0L01V,D2,IPM0L01,
D3,MQS0L01,D4,MQJ0L01,D5,MHE0L01V,D6,MQS0L01A,D7,

```

MHB0L01AH, MHB0L01AV, D8, ITV0L02, MQJ0L02, D9, IPM0L02, D3,
 MQS0L02, D10, MBH0L02H, MBH0L02V, D11, MQJ0L02A, D12, MHE0L02H,
 D13, MHB0L02AH, MHB0L02AV, D14, MQS0L02B, D15, MHB0L02BH, MHB0L02BV,
 D16, MHE0L03V, D17, ITV0L03, D18, MHE0L03H, D19, MBH0L03H, MBH0L03V,
 D20, MQJ0L03A, D21, IPM0L03, MQS0L03, D22, MQJ0L03, D23, IHA0L03,
 D24, ITV0L04, D1, MHB0L04H, MHB0L04V, D2, IPM0L04, D3, MQS0L04,
 D25, MQJ0L04, D26, R031, D27, R032, D28, R033, D27, R034, D28, R035,
 D27, R036, D28, R037, D27, R038, D29, ITV0L05, D30, MAT0L05H, D31,
 MAT0L05V, D32, IPM0L05, D3, MQS0L05, D33, MQJ0L05, D34, R041, D35,
 R042, D35, R043, D35, R044, D35, R045, D35, R046, D35, R047, D35, R048,
 D36, IPM0L06, D37, MDB0L06H, MDJ0L06V, D38, MQD0L06, D39, MBF0L06,
 D39, IPM0L07, D40, MDB0L07H, MDJ0L07V, D41, MQB0L07, D42, IHA0L07,
 D43, ITV0L08, D44, IPM0L08, D40, MDB0L08H, MDJ0L08V, D41, MQB0L08,
 D42, IHA0L08, D45, IPM0L09, D40, MDB0L09H, MDJ0L09V, D41, MQB0L09,
 D42, IHA0L09, D43, ITV0L10, D44, IPM0L10, D40, MDB0L10H, MDJ0L10V,
 D41, MQB0L10, D42, IHA0L10, D46, MBL0R01, D47, MAT0R01H, D48,
 MAT0R01V, D49, IPM0R01, D50, MQD0R01, D51, MAT0R02H, D48, MAT0R02V,
 D49, IPM0R02, D50, MQD0R02, D52, MBL0R02, ISR0R02, D53, MAT0R03H,
 D48, MAT0R03V, D49, IPM0R03, D50, MQD0R03, D53, MAT0R04H, D48,
 MAT0R04V, D49, IPM0R04, D50, MQD0R04, D54, IHA0R05, D55, MAT0R05H,
 D48, MAT0R05V, D49, IPM0R05, D50, MQD0R05, D56, ITV0R05, D57,
 BSM0R05V, D58, BSM0R05H, D59, MAT0R06H, D48, MAT0R06V, D49,
 IPM0R06, D50, MQD0R06, D53, MAT0R07H, D48, MAT0R07V, D49, IPM0R07,
 D50, MQD0R07, D60, MBL0R03, D61, MAT0R08H, D48, MAT0R08V, D49,
 IPM0R08, D50, MQD0R08, D62, IDA0R08, D63, SBC0R08, D64, IBC0R08,
 D65, MAT0R09H, D48, MAT0R09V, D49, IPM0R09, D50, MQD0R09, D66,
 BSM0R09V, D67, BSM0R09H, D68, MBL0R04, MKMATCHM56, MKMATCHD56

C.3 ELEGANT: INJ.ELE

The following lines show the code to perform the simulation of the injector line using the lattice file from the previous section.

```
&change_particle mass_ratio=0.5110034 &end
&run_setup
    lattice="INJ.lte",
    use_beamline="INJ",
    p_central_mev=6.27924163615229,
    final="%s.fin"
    parameters="%s.parms"
    sigma=%s.sig
&end
&twiss_output
    filename="%s.twi",
    matched=0,radiation_integrals=1,
    beta_x=3.07598, alpha_x=-0.56635,
    beta_y=2.79829, alpha_y=-0.397378
&end
&matrix_output
    SDDS_output=%s.mat
    start_from=MBL0R01
&end
&run_control n_steps=1
&end
&floor_coordinates
    magnet_centers=1,
    filename="%s.flr",
    X0=80.6
    Y0=100
    Z0=-249.14326,
    theta0=0,phi0=0
&end
&bunched_beam
```

```
n_particles_per_bunch=1024,  
emit_x=1.914000413443e-07, emit_y=1.914000413443e-07,  
beta_x=3.07598, alpha_x=-0.56635,  
beta_y=2.79829, alpha_y=-0.397378  
sigma_dp=0.0001,sigma_s=0.0001,  
distribution_type [0] = 3*" gaussian",  
distribution_cutoff [0] = 3*3,  
enforce_rms_values [0]=1,1,1  
&end  
&track  
&end
```

VITA

Mahmoud Mohamad Ali Ahmad
Department of Physics
Old Dominion University
Norfolk, VA 23529

EDUCATION

- Ph.D. 2016, Physics Department, Old Dominion University, Norfolk, Virginia.
- M.Sc. 2011, Physics Department, Old Dominion University, Norfolk, Virginia.
- M.Sc. 2004, Physics Department, Tanta University, Tanta, Egypt.
- B.Sc. 1999, Physics Department, Tanta University, Tanta, Egypt.

CONFERENCES AND WORKSHOP

- IPAC 2015, Richmond, Virginia, USA.
- NAPAC 2013, Pasadena, California, USA.
- BIW 2012, Newport News, Virginia, USA.

PUBLICATIONS

- Bunch length measurements using Synchrotron Light Monitor, M. M. Ali and M. G. Tiefenback, Proceedings of IPAC 2015.
- A bunch length monitor for JLAB 12 GeV upgrade, M. M. Ali, A. Freyberger, G. Krafft and J. Gubeli, Proceedings of NAPAC 2013.
- Precision absolute current measurement of low power electron beam, M. M. Ali, A. Freyberger, G. Krafft, M. Bevins and P. Degtiarenko, Proceedings of BIW 2012.
- A. M. Abo El Ata, F. M. Reich and M. M. Ali, Physics of low dimensional structure, 1 (2006) 31-35.
- A. M. Abo El Ata, F. M. Reich and M. M. Ali, Journal of Magnetism and Magnetic Materials, 292 (2005) 1724.